

Book of Abstracts

**THE 43RD ANNUAL SYMPOSIUM
ON POLYMER
SCIENCE/ENGINEERING**

**University of Waterloo
Waterloo, Ontario**

May 5th, 2021

**Institute for Polymer Research
University of Waterloo**

The Institute for Polymer Research would like to thank the sponsors for their support of the symposium.



2021

PROGRAM

**INSTITUTE FOR POLYMER RESEARCH
CELEBRATING 37 YEARS OF OFFICIAL INSTITUTE STATUS
FORTY-THIRD ANNUAL SYMPOSIUM
ON POLYMER SCIENCE/ENGINEERING 2019
Conrad Grebel College
Great Hall
University of Waterloo, Waterloo, Ontario
Wednesday, May 5, 2021**

- 8:50 **Welcome and Opening Remarks**
- 9:00 - 9:20 **Xiaotong Cao, Chemical Engineering, Waterloo (Prof. X. Feng, UW)**
Removal of phenolic compounds using poly(ether-block-amide) membranes
**(Winner of 2020 IPR Award for Academic Excellence in Polymer
Science/Engineering)**
- 9:20 - 10:00 **Academic Speaker: Professor Eduardo-Vivaldo Lima, National Autonomous
University of Mexico (UNAM) On the development of biorefining processes
from lignocellulosic biomasses**
- 10:00 – 10:25 **5-Min. Mini Presentations**
- 1) **Jada Steer (Prof. R. Dhib, Ryerson)**
Surface Modification of Fiber-Reinforced Polymer Composites
- 2) **Dylan Jubinville (Prof. T. Mekonnen, UW)**
Thermo-mechanical Reprocessing of Polypropylene for Utilization within
Postconsumer Applications
- 3) **Boris Nazareth (Prof. D. Schipper, UW)**
Functionalization of Hydrocarbon Polymers for Metal Oxide binding
applications
- 4) **Curtis Seto (Prof. T. Mekonnen, UW)**
Utilization of lignin for biocarbon production
- 5) **Rohan Shorey (Prof. T. Mekonnen, UW)**
Hydrophobic modification of lignin for rubber composites
- 10:25 – 10:40 **Coffee Break**
- 10:40 – 11:00 **Bhoomi Mavani (Prof. A. Penlidis, UW)**
Design of sensitive/selective polymeric materials for detection of VOCs
- 11:00 – 11:35 **5-Min. Mini Presentations**
- 6) **Daniel Afzal (Prof. Y. Li, UW)** Synthesis and Characterization of
Isopyridazine Derived from Isoindigo

	<p>7) Javan Buratynski (Prof. D. Schipper, UW) Tuning the Bandgap of Bithiazole Based Polymers</p> <p>8) Yunsheng Jiang (Prof. Y. Li, UW) A conjugated polymer donor Based on Alkyloxime Substituted Thiophene for BHJ organic solar cells</p> <p>9) Xiguang Gao (Prof. Y. Li, UW) An In-situ Formed Conductive Polymer for Enhancing the Performance of Li-S Batteries</p> <p>10) Yi Yuan (Prof. Y. Li, UW) Designing low-cost polymer donor for high performance non-fullerene acceptor based organic solar cells</p> <p>11) Lukas Bauman (Prof. B. Zhao, UW) The development and characterization of 3D Printable Double-network Hydrogels</p> <p>12) Jun-Zhi (Oliver) Wang (Prof. M. Gauthier, UW) pH-Responsive Polypeptides for Drug Delivery</p>
11:35 – 11:55	<p>Abdullah Basalem (Prof. J. Duhamel, UW) Characterization of Gemini Surfactants and their interactions with DNA by PEF</p>
11:55 - 1:00	Lunch
1:00 - 1:40	<p>Industry Speaker Valerie Farrugia, Xerox 2D and 3D Printing of Engineered Particles.</p>
1:40 – 2:00	<p>Audren Marquez (Prof. X. Wang, UW) The Role of Water in Self-Assembly</p>
2:00 – 2:20	<p>Kristijan Lulic (Prof. J. Duhamel, UW) Self-Association of Oligoquinoline Foldamers Probed by Fluorescence Anisotropy</p>
2:20 - 2:40	<p>Damin Kim (Prof. J. Duhamel, UW) Chemistry, Waterloo Compressibility of Amylopectin Characterized by Pyrene Excimer Formation</p> <p>(Winner of the 2020 IPR Award for Academic Excellence in Polymer Science/Engineering)</p>
2:40 – 3:00	Break

3:00 - 3:20

5-Min. Mini Presentations

13) Joanne Fernandez (Prof. M. Gauthier, UW)

Grafting of Starch Using a Cerium-Persulfate Initiation System

14) Natun Dasgupta (Prof. M. Gauthier, UW)

Synthesis of Thermoresponsive Chitosan Films grafted with Poly(di(ethylene glycol) methyl ether methacrylate)

15) Azin Adibi (Prof. T. Mekonnen, UW)

Engineered polysaccharide α -1,3 glucan as reinforcement fillers of rubber nanocomposite thin films for dipped goods application

16) Mingrui Liang (Prof. B. Zhao)

Tribological studies of cellulose nanocrystal polyurethane composite

3:20 – 3:40

Hunter Little (Prof. J. Duhamel, UW)

Probing the Internal Dynamics of Polymers in Polar Solvents

3:40 – 4:00

Remi Casier (Prof. J. Duhamel, UW)

Predicting the Folding Time of Proteins Based on Pyrene Excimer Formation Measurements on Polypeptides

4:00- 4:20

5-Min. Mini Presentations

17) Rebecca Lo (Prof. X. Wang, UW)

Synthesis of Macrocycles via Migration Insertion Polymerization

18) Helen Dawit (Prof. R. Dhib, Ryerson)

Modeling Average Molecular Weight Properties of PBMA via ARGET/AGET ATRP

19) Junjie Yin (Prof. J. Forrest, UW)

Stable polystyrene glasses through PVD and UV radiation

20) Sanjay Patel (Prof. J. Duhamel, UW)

Probing the Conformation of Structured Macromolecules by Pyrene Excimer Fluorescence

4:20-4:40

Break

4:40-5:00

Franklin Frasca (Prof. J. Duhamel, UW)

Gel Permeation Chromatography Analysis to Predict the Composition of PIBSI Dispersants

5:00-5:20

Janine Thoma (Prof. J. Duhamel, UW)
Using Pyrene Excimer Formation to Predict the flexibility of Polymeric
Bottle Brushes in Solution

5:20

Closing remarks

Extended Abstracts

Xiaotong Cao
Chemical Engineering
Waterloo

Removal of Phenolic Compounds using
Poly(ether-block-amide) Membranes

Winner of the 2021 IPR Award for Academic
Excellence in Polymer Science/Engineering

Removal of Phenolic Compounds using Poly(ether-block-amide) Membranes

Xiaotong Cao, Xianshe Feng*

Institute for Polymer Research & Department of Chemical Engineering, University of Waterloo, Waterloo, ON, Canada, N2L3G1

Phenolic compounds are common organic pollutants in a wide range of effluents from such industries as textile, pharmaceutical, rubber, plastic, wood processing, petrochemical, cosmetics and coal-tar production, with typical concentrations from a few ppm to several grams per liter. Due to their high toxicities and carcinogenicities, they are listed in the US as pollutants of priority concerns. As such, effective methods must be developed to remove phenolic compounds from water streams before discharge. This work attempted to use an energy efficient technology to remove phenolic contaminants from wastewater.

Among the current technologies, pervaporation is regarded as a promising technology for efficient removal of organic compounds from water, especially when the concentration of the organic compounds is low, due to such advantages as low operating cost, easy operation, no chemical addition and no regeneration required [1]. In pervaporation, the feed liquid contacts with one side of the membrane, and the permeated molecules are removed as a low-pressure vapor from the downstream side of the membrane (Figure 1). For such applications, polymers are the most commonly used material to prepare pervaporation membranes because of the ease of fabrication and low cost. The separation of organic compounds from water streams requires preferential permeation of organic compounds through the membrane, and the permselectivity of the membrane materials towards the target compounds is of significant importance for the separation performance.

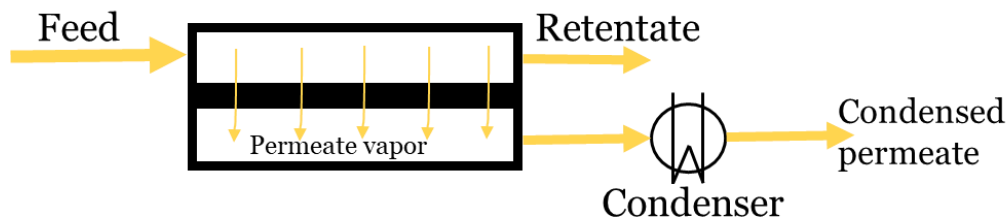


Figure 1. Schematic diagram of the pervaporation process.

Poly(ether-block-amide) (PEBA) is a block copolymer composed of rigid polyamide and soft polyether segments (Figure 2). Manipulating the relative content of the two blocks can give a series of elastomers with different properties. The first report on PEBA membrane for the pervaporative separation of phenol from aqueous solutions is attributed to Bøddeker of GKSS, who disclosed in 1989 that PEBA outperformed other elastomers [2]. After that, a series of investigations on the removal of phenolic compounds using different grades of PEBA membrane by pervaporation have been conducted. Among them, PEBA 2533, which has the highest content of the soft poly(tetramethylene oxide) segment in the thermoplastic elastomer series (80 wt%), showed excellent permselectivity to phenol due to its good affinity. Our previous work showed that PEBA 2533 can be used successfully for the sorptive removal of phenolic compounds as well. Therefore, PEBA 2533 was selected as the membrane material to separate phenolic compounds from aqueous solutions in current work.

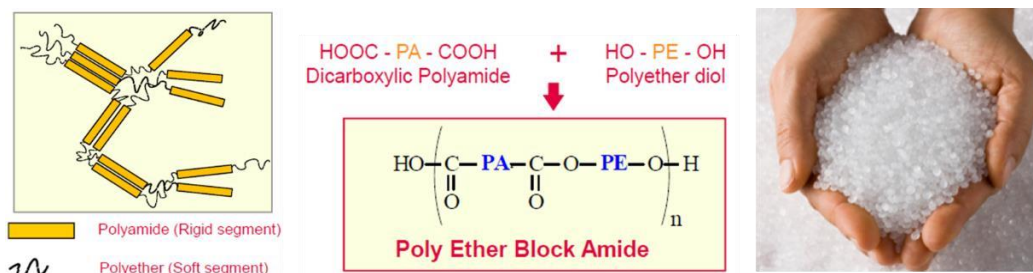


Figure 2. PEBA copolymer [3].

In this work, we studied the pervaporative removal of four representative phenolic compounds (phenol, p-cresol, p-nitrophenol, and p-chlorophenol) that are among the category of the most common phenolic compounds in natural environment and human surroundings using PEBA 2533 membrane. PEBA pellets were fabricated into membranes by a solution-casting technique. The membrane showed high permselectivity to phenol, p-cresol, and p-chlorophenol, while p-nitrophenol could hardly permeate through the membrane due to its negligible transmembrane driving force. Figure 3A shows the overall solute concentration in the permeate, where phenol, p-cresol and p-chlorophenol were highly concentrated by pervaporation. The high membrane permselectivity towards phenolic compounds predominantly comes from the high sorption selectivity, where PEBA shows a high solubility to phenolic compounds (Figure 3B). The effects of feed concentration and operating temperature on membrane performance were investigated. The permeation flux increased with an increase in feed concentration, while the enrichment factor decreased. Both the permeation flux and the enrichment factor increased with an increase in temperature. This can be explained from three aspects: (1) the thermal motion of the polymer chains is enhanced at high temperatures, (2) the permeating molecules are more energetic at high temperatures, and (3) an increase in temperature increases the vapor pressure of the permeating molecules in the liquid feed, thereby increasing transmembrane driving force for permeation. Depending on the specific phenolic solute, high-purity phenolic crystals could be produced from the phenolic-enriched permeate via de-sublimation in the cold trap, which is of particular interest for practical applications. Furthermore, in view of the coexistence of multiple phenolic compounds in practical wastewater, the pervaporation performance for feed solutions containing multiple phenolic compounds was studied. The coupling effects of co-existing phenolic compounds due to permeant-permeant interactions were found to be significant in permeation of multiple phenolic compounds. The permeation of phenol, p-cresol, and p-chlorophenol was affected adversely by the presence of other phenolic compounds in the feed solution, while the opposite was true for the permeation of slow-permeating p-nitrophenol.

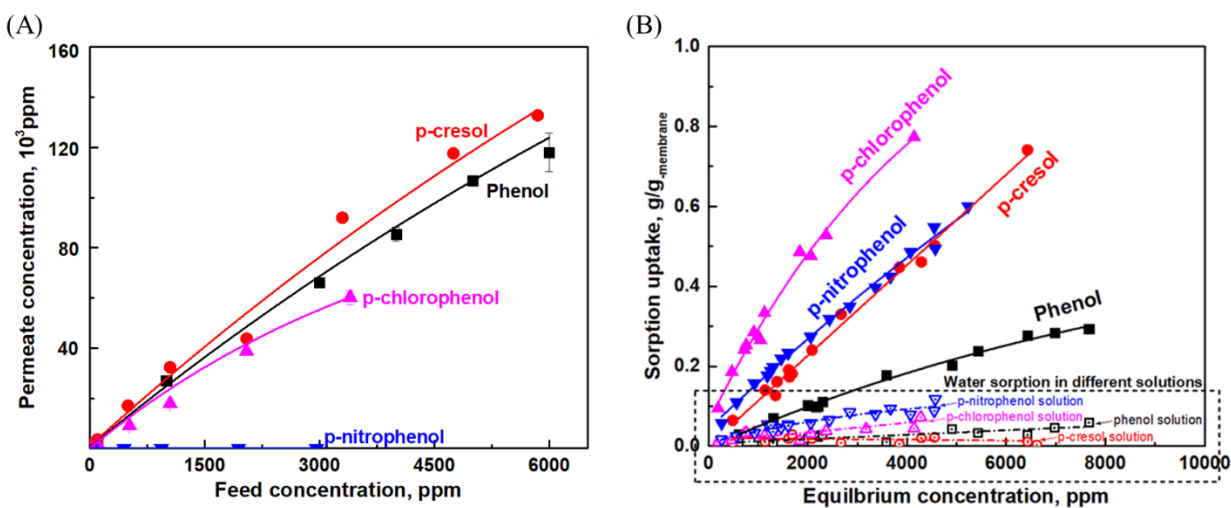


Figure 3. The overall solute concentration in the permeate at 30°C (A), and the solubility of phenolic compounds and water in PEBA membrane at 30°C (B).

In view of the excellent permselectivity of PEBA 2533 membrane to phenolic compounds, the membrane was also used in a perstraction system to separate phenolic compounds. Perstraction, a process combining selective permeation of a component through nonporous polymeric membranes and extraction into an extracting solution, is another membrane-based process that appears to be particularly suitable for removing phenolic compounds from water. The mass transport is driven by the difference in the chemical potential of the feed liquid and the stripping liquid. In such a perstraction process, the stripping phase should have a stronger affinity to phenolic compounds than the membrane so that phenolic molecules can be removed from the membrane upon reaching the downstream side. In this work, an alkaline solution was used as the stripping liquid because phenolic compounds are mildly acidic and will dissociate under alkaline conditions. It was found PEBA membrane can selectively extract phenolic compounds from water streams by perstraction. With an increase in the concentration of sodium hydroxide in the stripping solution, the overall mass transfer coefficient of perstraction increased at first and then became constant when the alkaline concentration was high enough (Figure 4). The use of an alkaline stripping agent can effectively enhance the removal of phenolic compounds from water by reducing the mass transfer resistances of the liquid boundary layers and desorption at the downstream side of the membrane [4].

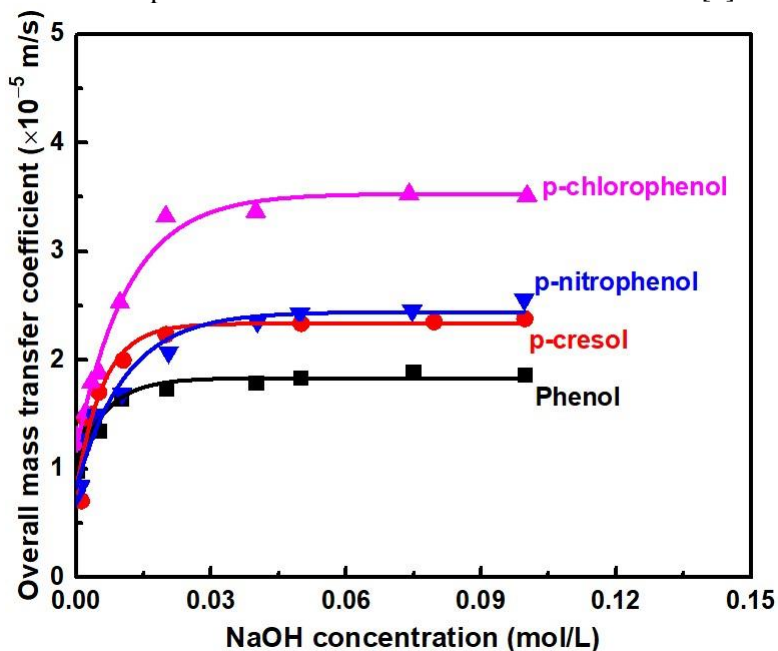


Figure 4. Effects of NaOH concentration in stripping solution on the overall mass transfer coefficient in perstraction at 30°C.

In conclusion, due to the good affinity between PEBA polymer and phenolic compounds, PEBA 2533 was shown to be material suitable for the removal of phenolic compounds from water streams by sorption, pervaporation and perstraction.

References:

- [1] X. Cao, K. Wang, X. Feng, Removal of phenolic contaminates from water by pervaporation, *J. Membr. Sci.* (623) 2021, 119043.
- [2] K.W. Böddeker, Pervaporation of phenols, US Patent 4,806,245 (1989).
- [3] N. Deluca, PEBA: TPE materials for high performance applications, in: *SPE-ANTEC 2017*, Anaheim, California, USA, May 2017, vol 1., pp 1423.
- [4] X. Cao, K. Wang, X. Feng, Perstraction of phenolic compounds via nonporous PEBA membrane, *Sep. Purif. Technol.*, (257) 2021, 117928.

Dr. Eduardo-Vivaldo Lima, PhD
Professor
National Autonomous University of Mexico
(UNAM)

On the Development of Biorefining Processes
from Lignocellulosic Biomass

On the development of biorefining processes from lignocellulosic biomasses

Prof. Eduardo Vivaldo-Lima, Prof. Martín G. Hernández-Luna, and Prof. Eduardo Bárzana, Facultad de Química, Universidad Nacional Autónoma de México (UNAM), Ciudad de México, 04510, México

Summary

A brief overview of the research on developing of biorefining processes from lignocellulosic waste biomasses carried out at UNAM's Facultad de Química is presented. The key aspect on the successful design/operation of a biorefinery is the pretreatment stage. Two pretreatment processes have been developed at FQ-UNAM. One of them, co-invented in collaboration with European, Central- and South-American partners, is the so-called "Combined Extrusion-Saccharification" (CES) process. Some highlights on the process, examples of production of added value chemicals and modeling of the pretreatment stage are offered. A few key aspects on the present research efforts (second pretreatment process) are also offered.

Introduction

The use of lignocellulosic waste as raw material for biorefining processes that allow the production of added-value products, such as bioethanol, cellulose, xylose, or hybrid materials, among others, has gained importance in the last two decades. The concept of biorefinery from lignocellulosic waste involves multistep processes that start with pretreatment of the biomass, so that the individual biopolymers (cellulose, hemicellulose and lignin) are chemically available for subsequent reactive processes [1-5]. The most efficient pretreatment process available to date is steam explosion (SE). It is the basis of the Abengoa, BioGasol and Beta Renewables industrial processes. In this method, chipped biomasses are treated with high-pressure saturated steam and then pressure is swiftly reduced, which makes the materials undergo an explosive decompression. Steam explosion is typically initiated at a temperature of 160–260 °C (corresponding pressure 0.69–4.83 MPa) for several seconds to a few minutes before the material is exposed to atmospheric pressure. The process causes hemicellulose degradation and lignin transformation due to the high temperatures, thus increasing the potential of cellulose hydrolysis [6-11]. Other pretreatment processes of technological or scientific relevance include (diluted) acid hydrolysis, (diluted) alkaline hydrolysis, Organosolv fractionation, twin-screw extrusion and fractionation using ionic liquids [9,12-15].

The yield of total sugars obtained after diluted pretreatment and subsequent enzymatic hydrolysis was in the range of 5.2 [13] to 73.6% (w/w) [12]. The yield reached after hydrolysis for alkaline pretreatment was 58% [13], while for ionic liquid and ethanosolv pretreatments the yield of saccharification was about 85% [14,15]. However, one of the drawbacks of these processes is the post-treatment, either washing or neutralization before enzymatic hydrolysis, or the generation of by-products.

Experimental systems studied

Two pretreatment processes were developed at FQ-UNAM. The first one is CES, which is the one whose results are described here. The second one is non-enzymatic in nature and will be discussed in the presentation.

The pretreatment stage for the CES process was carried out in a twin-screw extruder (Clextal Processing Platform Evolum EV25, Clextal France) composed of 10 modules, each 100 mm in length, one with electrical heating (Figure 1). Module one was used for the introduction of raw BAB at a flow rate of 0.23 kg h^{-1} . Two pumps were used to supply aqueous NaOH, 5% w/v, to module 3. The ratio the flow rate of aqueous NaOH to the flow rate of BAB (L/S) maintained in the extruder was 3.7. BAB deconstruction took place in modules 4-6. Temperature in this zone was programmed at 50°C . Module 5 consisted of a compression zone, which was followed by a mixing zone in module 6. Module 7 was used as an *in situ* neutralization zone; at this stage, aqueous phosphoric acid (5% w/v), at $L/S = 3.7$, was fed into the module. Module 8 was a zone of intensive mixing. Module 9 was used for filtration. Module 10 consisted of 2 reverse screws, thus acting as a compression zone. Operation conditions were set to achieve a NaOH/DM ratio of 10% (w/w), a liquid/solid ratio of 7.5 and a rotation speed of 100 rpm. This complex process will be referred to as “extrusion” hereafter. After extrusion, the solid extruded biomass was recovered, dried and analyzed for carbohydrates and lignin content [16]. A schematic representation of the process is show in Figure 1. Other details about the experimental system are provided in our published reports [16,17]. Some representative results of hydrolysis yield using several enzymes, theoretical yield of C6 sugars, as well as glucose and ethanol yields are shown in Figure 2.

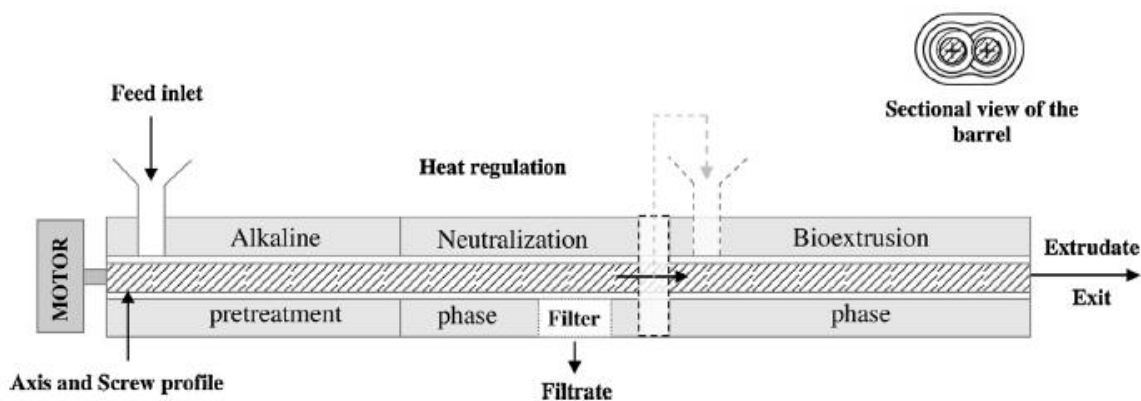


Figure 1. Schematic representation of the CES process (pretreatment and initial enzymatic hydrolysis) as two successive twin-screw extruders or, a single one divided in two zones, one for alkaline pretreatment and the other for bioextrusion [16].

An example of modeling work

The acid pretreatment of cellulose in batch and twin-screw extruder reactors has been modeled in our group [18]. Representative results are shown in Figure 3. It is generally observed that the reactions are faster in the twin-screw extruder.

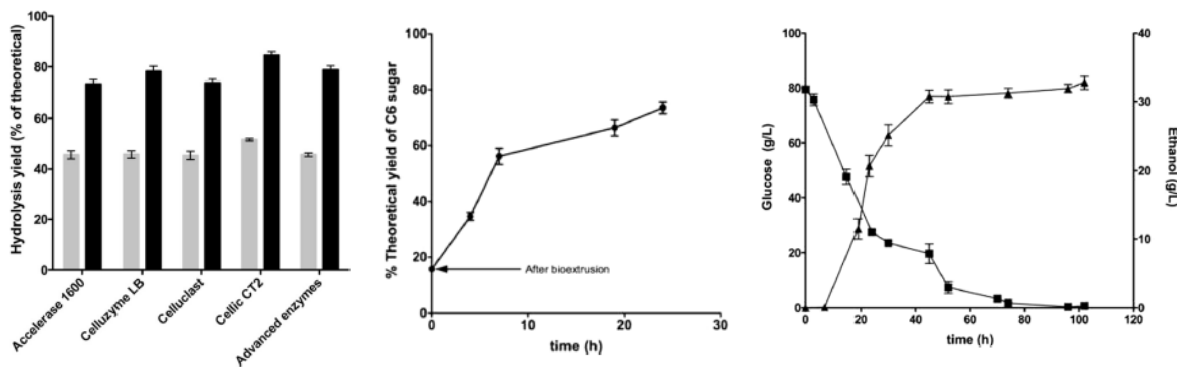


Figure 2. Representative results of the CES process: (a) enzyme selection; (b) C6 sugars yield during bio-extrusion and continued hydrolysis in an autoclave; (c) glucose and ethanol yield [17].

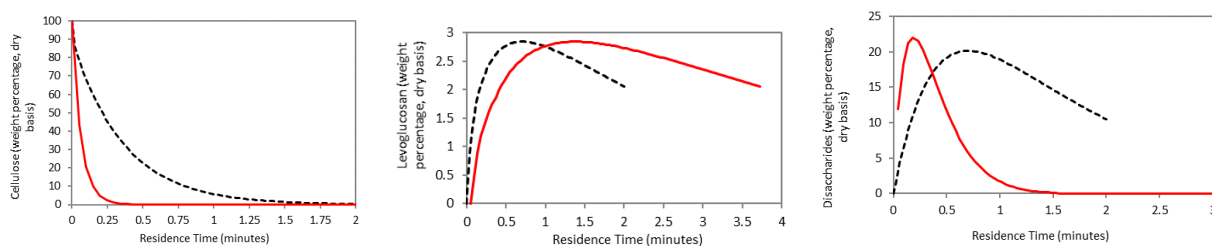


Figure 3. Modeling of cellulose acid degradation at 230 °C in batch (dark profiles, dotted line) and twin-screw extruder (red profile, solid line) reactors: (a) cellulose degradation; (b) levoglucosan production; (c) disaccharides production [18].

Conclusion

Pretreatment is the core of a refinery based on lignocellulosic waste biomasses. CES is a process which is competitive with the leading commercial processes, such as steam explosion and Organosolv. It may be attractive from the fact that small modular plants can be built in places close to the biomass waste generation.

Our modeling description of acid or alkaline pretreatments can describe the experimental trends.

Acknowledgements

Financial support from the following sources is gratefully acknowledged: (a) DGAPA-UNAM, Project PAPIIT IV100719, as well as PASPA sabbatical support to E.V.-L. while at the University of Waterloo, in Ontario, Canada; (b) European Community, Seventh Framework Program, grant agreement no. 227498 (BABETHANOL PROJECT); (c) Consejo Nacional de Ciencia y Tecnología (CONACYT, Mexico), Bioenergy Thematic Network (“Red Temática de Bioenergía”), grant 260457; (d) Facultad de Química-UNAM, research funds granted to E. V.-L. (PAIP 5000-9078); and (e) Department of Chemical Engineering, University of Waterloo, Canada, partial sabbatical support to E.V.-L. with research funds from Prof. Alexander Penlidis.

We acknowledge the participation of Dr. Oscar Hernández-Meléndez and Prof. Carmina Montiel-Pacheco, who carried out the experimental worked described here; as well as Dr. Jorge Alcaraz-Cienfuegos and Prof. María de los Ángeles Valdivia-López, who have carried out the experimental work related to the second (non-enzymatic) pretreatment process developed at FQ-UNAM.

References

- [1] M. FitzPatrick, P. Champagne, M. F. Cunningham, R. A. Whitney, *Bioresour. Technol.* **2010**, *101*, 8915-8922.
- [2] M. Brodin, M. Vallejos, M. T. Opedal, M. C. Area, G. Chinga-Carrasco, *J. Cleaner Prod.* **2017**, *162*, 646-664.
- [3] S. Niphadkar, P. Bagade, S. Ahmed, *Biofuels* **2018**, *9(2)*, 229-238.
- [4] J. Banerjee, R. Singh, R. Vijayaraghavan, D. MacFarlane, A. F. Patti, A. Arora, *Food Chem.* **2017**, *225*, 10-22.
- [5] U. Neuling, M. Kaltschmitt, *J. Oil Palm Res.* **2017**, *29*, 137-166.
- [6] E. Tomás-Pejó, P. Alvira, M. Ballesteros, M. J. Negro, In *Biofuels: Alternative Feedstocks and Conversion Processes*, (Eds: A. Pandey, C. Larroche, S. C Ricke, C.-G. Dussap, E. Gnansounou), Elsevier-Academic Press, Oxford, UK **2011**, Ch. 7.
- [7] M. Rastogi, S. Shrivastava, *Renew. Sustain. Ener. Rev.* **2017**, *80*, 330-340.
- [8] M. Vochozka, A. Maroušková, J. Váchal, J. Straková, *Waste Biomass Val.* **2016**, *7(6)*, 1549-1554.
- [9] L.-X. Jiang, S. Fang, J.-W. Mao, J.-H. Xie, *Mater. Sci. Forum* **2016**, *852*, 1175.
- [10] A. Duque, P. Manzanares, I. Ballesteros, M. Ballesteros, in *Biomass Fractionation Technologies for a Lignocellulosic Feedstock Based Biorefinery* (Ed: S.I. Mussatto), Elsevier, Oxford, UK **2016**, Ch. 15.
- [11] Y. Sun, J. Cheng, *Bioresour. Technol.* **2002**, *83*, 1-11.
- [12] J. Saucedo-Luna, A. J. Castro-Montoya, M. M. Martínez-Pacheco, C. R. Sosa-Aguirre, J. Campos-García, *J. Ind. Microbiol. Biotechnol.* **2011**, *38*, 725-732.
- [13] J. M. Hernández-Salas, M. S. Villa-Ramírez, J. S. Veloz-Rendón, K. N. Rivera-Hernández, R. A. González, M. A. Plascencia-Espinosa, S. R. Trejo-Estrada, *Bioresour. Technol.* **2009**, *100*, 1238-1245.
- [14] J. A. Pérez-Pimienta, M. G. López-Ortega, J. A. Chávez-Carvayar, P. Varanasi, V. Stavila, G. Chen, S. Singh, B. A. Simmons, *Biomass. Bioenerg.* **2015**, *75*, 180-188.
- [15] L. Caspeta, M. A. Caro-Bermúdez, T. Ponce-Noyola, A. Martínez, *Appl. Energy* **2014**, *113*, 277-286.
- [16] V. Vandenbossche, J. Brault, G. Vilarem, O. Hernández-Meléndez, E. Vivaldo-Lima, M. Hernández-Luna, E. Barzana, A. Duque, P. Manzanares, M. Ballesteros, J. Mata, E. Castellón, L. Rigal, *Ind. Crop. Prod.* **2014**, *55*, 258-266.
- [17] C. Montiel, O. Hernández-Meléndez, E. Vivaldo-Lima, M. Hernández-Luna, E. Barzana, *Bioenerg. Res.* **2016**, *9(4)*, 1005-1014.
- [18] J. C. Morales-Huerta, G. Jaramillo-Soto, O. Manero, E. Barzana, and E. Vivaldo-Lima, "Modeling of pretreatment and acid/alkaline hydrolyses of lignocellulosic biomasses in twin-screw extruders", *Ind. Eng. Chem. Res.*, *59(25)*, 11389-11401, 2020; DOI: 10.1021/acs.iecr.0c01737.

Jada Steer
Chemical Engineering
Ryerson

Surface Modification of Fiber-Reinforced Polymer Composites

Surface Modification of Fibre-Reinforced Polymer Composites

Jada Steer



Introduction

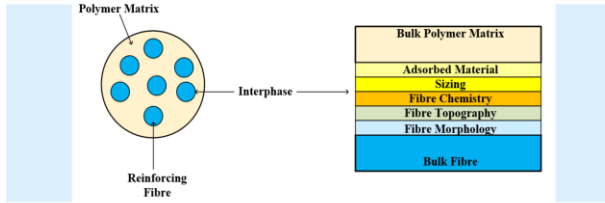
- Fibre-Reinforced Polymer Composites (FRPs)
- Used for many high-performance applications
 - Aerospace
 - Automotive
 - Biomedical
 - Structural
- Exceptional properties include:
 - High strength-to-weight ratio
 - Corrosion resistance
 - Thermal resistance



(1) Luo W., Zhang B., Zou H., Liang M., Chen Y., *J. Ind. Eng. Chem.*, 2017, 51, 129-139; (2) Ash R., Jans F., *Bolton J. Nanotech.*, 2016, 7, 1174-1196

May 5, 2021 | 2

Rationale & Objectives



- Performance of FRPs is dependent on:
- Fibre Volume Fraction
 - Fibre Aspect Ratio
 - Fibre Orientation
 - Fibre/Matrix Interphase

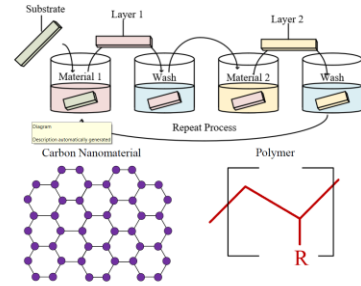


(3) Luo W., Zhang B., Zou H., Liang M., Chen Y., *J. Ind. Eng. Chem.*, 2017, 51, 129-139

May 5, 2021 | 3

Methodology

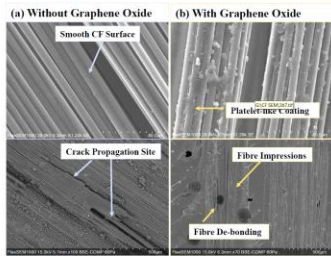
- Conduct a layer-by-layer assembly process via dip-coating
- Fabricate graphitic and polymeric layers on the fiber surface
- Determine impact on the mechanical properties of fibre-reinforced polymer composites



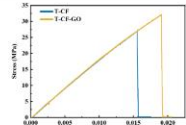
(4) Richardson J., Bjornholm M., Curcio F., *Science*, 2015, 348, 411-421

May 5, 2021 | 4

Progress & Next Steps



- Deposition of Graphene Oxide on Carbon Fibre
- Quantified interfacial strength using transverse tensile tests with an Epoxy matrix



(5) Luo W., Zhang B., Zou H., Liang M., Chen Y., *J. Ind. Eng. Chem.*, 2017, 51, 129-139

May 5, 2021 | 5

Conclusions

- Fibre-reinforced polymer composites have many diverse applications
- Improve the interfacial strength of fibre-reinforced polymer composites using surface modification
- Deposition of carbon nanomaterials and polymeric coating onto reinforcing fibres
- Enhance the dynamic properties of fibre-reinforced polymer composites



May 5, 2021 | 6

Dylan Jubinville
Chemical Engineering
Waterloo

Thermo-Mechanical Reprocessing of
Polypropylene for Utilization within Post-
consumer Applications

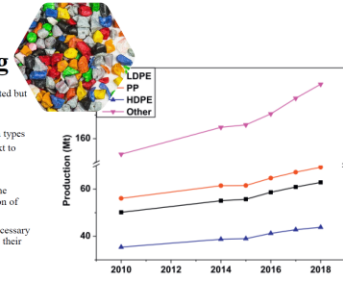
Thermo-mechanical Reprocessing of Polypropylene for Utilization within Post-consumer Applications

Presented by Dylan Jubinville MASc, EIT.



Polymer Recycling

- In 2019, 360 MT of polymeric material was converted but with only ~9% of it being recycled.
 - Equivalent weight of 10 empire state building.
- Polypropylene (PP) one of the most converted resin types
 - Largest share in municipal waste fractions next to polyethylene.
 - 0 to 1% of it being recycled
- The shift towards circular economies is driven by the increase environmental governance and consumption of resources (e.g. fossil fuels).
- A proper understand on the effect of recycling is necessary to observe how process induced degradation affects their potential re-usage.



Types of recycling*

- thermo-mechanical (heat and high shear)
 - Open loop
 - Post-consumer
 - Down-cycling
- Chemical
 - Closed loop
- re-use
 - Post-industrial
 - Up-cycling
- Incineration for energy recovery

*The type of recycling employed will depend on the **manufacture, desired outcome, and available resources.**



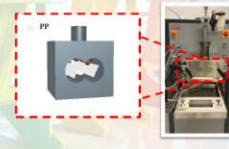
Materials

- Polypropylene [PP]
 - Lyondellbasell
 - Homo-polymer
 - $\rho = 0.90 \frac{g}{cm^3}$
 - MFI = $12 \frac{g}{10 min}$



Processing Methods

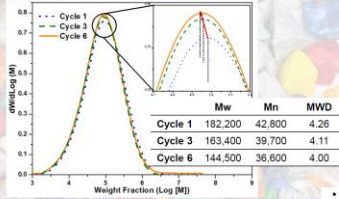
- Batch (Kinetic) mixer
 - Barrel Temperature: 180 °C
 - Melt Temperature: 195 °C
 - Screw Speed: 100 rpm



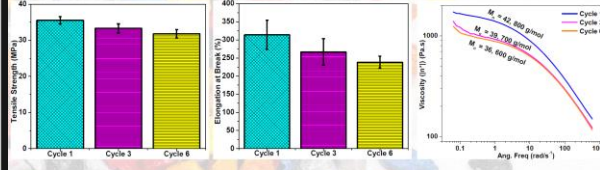
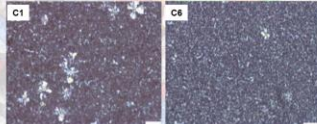
Recycling method



Results



- As PP is repeatedly reprocessed, the molecular weight decreases from 211,000 to 144,500 (32%).
 - Likely a result of molecular fragmentation (e.g. chain scission).
- Most significant changes were between C3 and C6 at bands 1765 cm⁻¹ (C=O) (asymmetric stretching).
 - Indicating onset of oxidative degradation and discoloration



- The effect of recycling on PP is not significant.
 - Except for elongation at break (%) which decreases by 10% (likely due to molecular fragmentation resulting in an increase number of small chain compounds (e.g. oligomers)).
- Parallel plate rheology showed that with increased extrusion cycles there is a decrease in melt viscosity.
 - Since constant temperature (180 °C), the decrease in viscosity is a strong indicator of chain scission.

Conclusion

- Overall, polypropylene can seemly be recycled up to at least 6 times while maintain its mechanical properties
- Process induced degradation greatly affects the materials flow behaviour and crystallinity.
 - As a result of chain scission being the primary mechanism for degradation until later cycles.



Boris Nazareth
Chemistry
Waterloo

Functionalization of Hydrocarbon Polymers for Metal Oxide Binding Applications

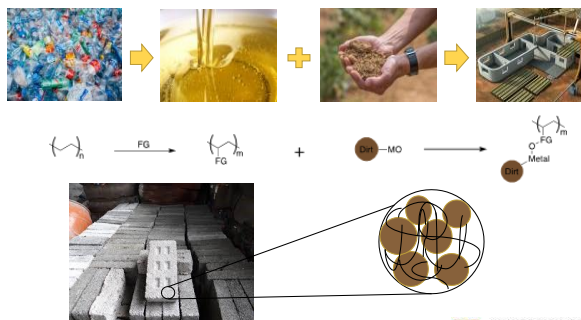
Functionalization of Hydrocarbon Polymers for Metal Oxide Binding Applications



Supervisor: Dr. Derek Schipper
IPR Symposium
May 5th, 2021

Boris Nazareth

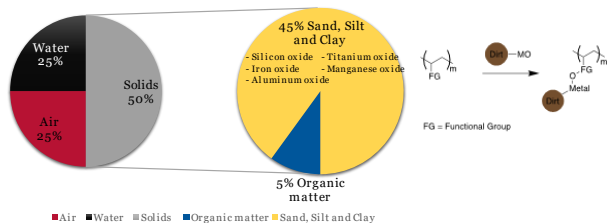
Objective



PAGE 2

Functional group – Metal oxide bond

APPROXIMATE COMPOSITION OF SOIL



Soils: genesis and geomorphology - Cambridge University Press: New York, NY, 2005.
Encyclopedia of Soils in the Environment. 2005, 428-438.

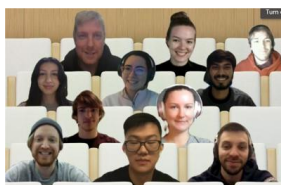
PAGE 3

Samples produced



PAGE 4

Acknowledgements



Thank you!

Dr. Derek Schipper
Jianan Wang
Mila Abaeva
Lukas Glofcheskie
Emily Verkuil
Jack Buchok
Rafael Mirabal
Javan Buratynski
Scott McNeil
Jasmin Nazarali
Giulia Sellitto

PAGE 5

Curtis Seto
Chemical Engineering
Waterloo

Utilization of Lignin for Biocarbon Production

Utilization of Lignin for Biocarbon Production

3/22/2023

Presenter: Curtis Seto
Supervisors: Prof. Mekonnen & Prof. Tzoganakis



Outline

- Introduction
- Experimental
- Characterization
- Dye adsorption

PAGE 2



Introduction - Lignin

- Lignin one of the most abundant biopolymers, over 300 billion tons present in the biosphere, 70 billion tons annual production



FIGURE 1
Lignin structure

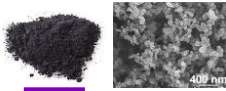


FIGURE 2
Carbon black

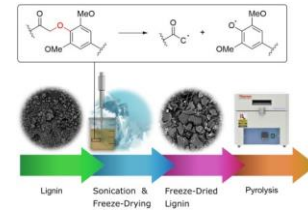
- Carbon materials
 - Carbon black, graphene, nanotubes, etc.
 - Carbon black: 17 billion USD market size (2018)

PAGE 3



Lignin for biocarbon production

- Goal: Lignin into biocarbon
- Pyrolysis is the thermal decomposition of material under inert gas
- Experiment:
 - Lignin and Freeze dried lignin
 - 600, 750, 900, 1050 °C



PAGE 4



Characterization

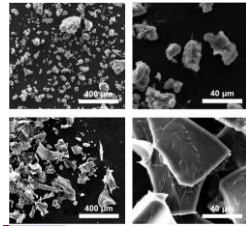


FIGURE 5
Chars from lignin (top) and treated lignin (bottom)

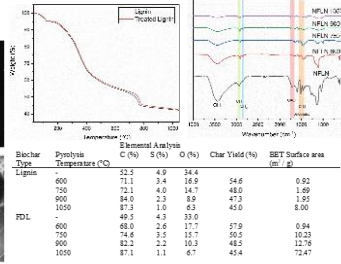


FIGURE 6
Characterization

PAGE 5



Dye adsorption

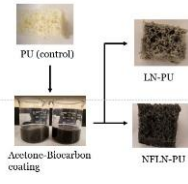


FIGURE 6
Process of coating poly urethane foam with biocarbon

PAGE 6

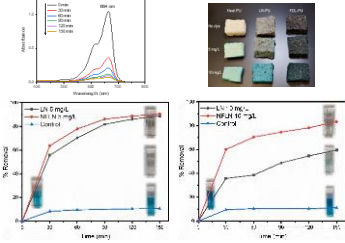


FIGURE 7
Dye adsorption results

PAGE 6



Thanks for listening

PAGE 7



Rohan Shorey
Chemical Engineering
Waterloo

Hydrophobic Modification of Lignin for Rubber Composites

Hydrophobic modification of lignin for rubber composites

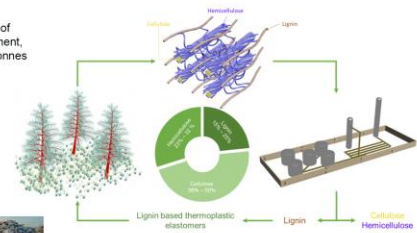
Rohan Shorey
Supervisor: Prof. Tizazu Mekonnen

May 2021



Lignin

- In Canada, an estimated 1% of plastic waste enters environment, which accounted for 29000 tonnes in 2016 alone¹.



¹ Science assessment of plastic pollution - Canada.ca. <https://www.canada.ca/en/environment-climate-change/services/evaluating-existing-substances/science-assessment/plastic-pollution.html>
² Chemists are reimagining recycling to keep plastics out of landfill | Science News. <https://www.sciencenews.org/article/chemistry-recycling-plastic-useful-green-chemistry>

Modification of lignin

- Why?
- Which functional groups to target in lignin structure?
- Functionalized lignin
 - Acetylation
 - Esterification
 - Silylation → Silylating agent
 - and many more....

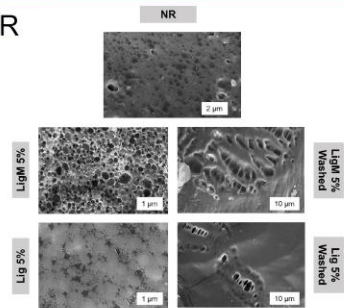
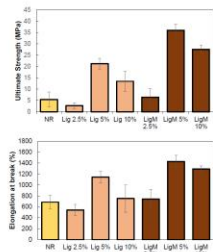
Sample	Elemental Composition (%)	
	C	N
Lignin	65.95	-
LigninM	49.5	1.53

Application in elastomeric matrices

- With the enhanced hydrophobicity imparted by the functionalized lignin, better dispersibility in nonpolar elastomeric matrix can be achieved.
- Thus, entailing composites with better mechanical properties.
- Further, the mechanical properties of Lignin-NR and Silylated Lignin-NR composites were compared with respect to the baseline NR.
- Lignin would represent the rigid segment, dispersed in elastomeric matrix, as can be observed in the figure.



Composites with NR



Conclusion

- Silylated lignin exhibited better dispersion than unmodified lignin in NR matrix.
- The tensile strength and elongation at break imparted on the composites by Silylated lignin were better than unmodified lignin, the best properties being exhibited by 5 wt% modified lignin specimen.
- The SEM images were paramount in observing the better dispersibility of silylated samples in NR.

Thank you!

Bhoomi Mavani
Chemical Engineering
Waterloo

Design of Sensitive/Selective Polymeric Materials for Detection of VOCs

Design of sensitive/selective polymeric materials for detection of VOCs

Bhoomi Mavani and Alexander Penlidis

Institute for Polymer Research, Department of Chemical Engineering, University of Waterloo

Volatile organic compounds (VOC) include any compound of carbon (excluding carbon monoxide, carbon dioxide, carbonic acid, metallic carbides or carbonates, and ammonium carbonate), which participates in atmospheric photochemical reactions, except those designated by EPA as having negligible photochemical reactivity [1]. Some common VOCs include formaldehyde (F), benzene (B), acetone (A), ethanol (E), and acetaldehyde (Ac) which can be present indoors and outdoors. Exposure to even low concentration of VOCs can cause discomfort in the eyes, nose and throat, shortness of breath, nausea, and headache. Exposure to high concentration can cause damage to the liver, kidney, and nervous system. Therefore, it is important to be able to detect and monitor the concentration of VOCs present in the surroundings. Detection of VOCs or toxic gas analytes using polymeric gas sensing materials has many applications in fields such as environmental (for air and water quality analysis), biomedical (breath and skin analysis for alcohol detection), industrial sites/environments, and finally, for chemical warfare agent (CWA) detection.

Chemical warfare agents (CWAs) are highly toxic synthetic chemicals that have lethal or incapacitating effects on humans [2] [3]. A substance can be categorized as CWA based on its characteristics such as high toxicity, imperceptibility to sense, rapidity of action, and persistency, as listed in the Chemical Weapons Convention (CWC) [4]. Sarin and Soman gases, for example, are highly toxic nerve agents, which can cause death within one minute of ingestion of 0.1 mg per kg of body weight [5]. Since CW agents are highly toxic, they are not safe to use for preliminary experiments in developing polymeric sensing materials for detection purposes. Therefore, surrogate gases are commonly used, which possess similar properties, functional groups and reactivity but are much less toxic [5]. For example, formaldehyde and acetaldehyde can be used instead of phosgene due to the characteristic carbonyl group and similar molecular size.

This research focuses on the detection of aldehydes, which can be considered as surrogate gases for toxic agents (as they have similar functional groups with several warfare agents) using several polymeric gas sensing material. Due to the chemical similarity of formaldehyde with CWAs, it was used as the target analyte and benzene has been selected as the interferent gas, as it is representative of aromatic hydrocarbons. Polymeric sensing materials that have been used for the detection of both formaldehyde and acetaldehyde include polyaniline (PANI) and its derivatives [6], and it has been established that PANI and P25DMA (poly (2,5,-dimethyl aniline)) seem to be potentially good sensing materials for the detection of formaldehyde and benzene [7].

Therefore, PANI and P25DMA were further evaluated to improve sensitivity and selectivity (and stability) by doping PANI with metal oxides such as indium oxide. In principle, metal oxide dopants can be added to improve the selectivity/sensitivity (and mechanical integrity) of a sensing material [8], [9]. The dopant can affect the sensitivity/selectivity by incorporating (dispersing) in different ways inside the polymer structure, thus increasing the surface area, enhancing the folding of the polymer chains, and improving mechanical and physical integrity. On the other hand, if homogeneous incorporation fails, then the presence of the metal oxide may destroy an otherwise good sensing (for enhanced sensitivity/selectivity) structure of the polymer. In_2O_3 was used as a dopant to improve (hopefully) the sensing properties of (undoped) PANI. In_2O_3 metal oxide enhanced sensing properties due to its unique hollow porous shell structure [10]. It is a good semiconductor with a bandgap of 3.55-3.75eV [11]. The metal oxide is typically incorporated in polymeric materials up to 20% by weight.

The sorption capabilities of the polymeric gas sensing materials were evaluated using a specialized gas chromatograph (GC) which is capable of detecting gas as low as ppb levels. PANI and PANI doped with different weight percentages (wt.%) of In_2O_3 were tested for sorption of F by exposing materials to a 10 ppm F source. Figure 1 shows a typical F sorption performance plot for undoped and doped PANI. Several independent replicates were conducted per each test, with the associated rigorous statistical analysis of the collected data.

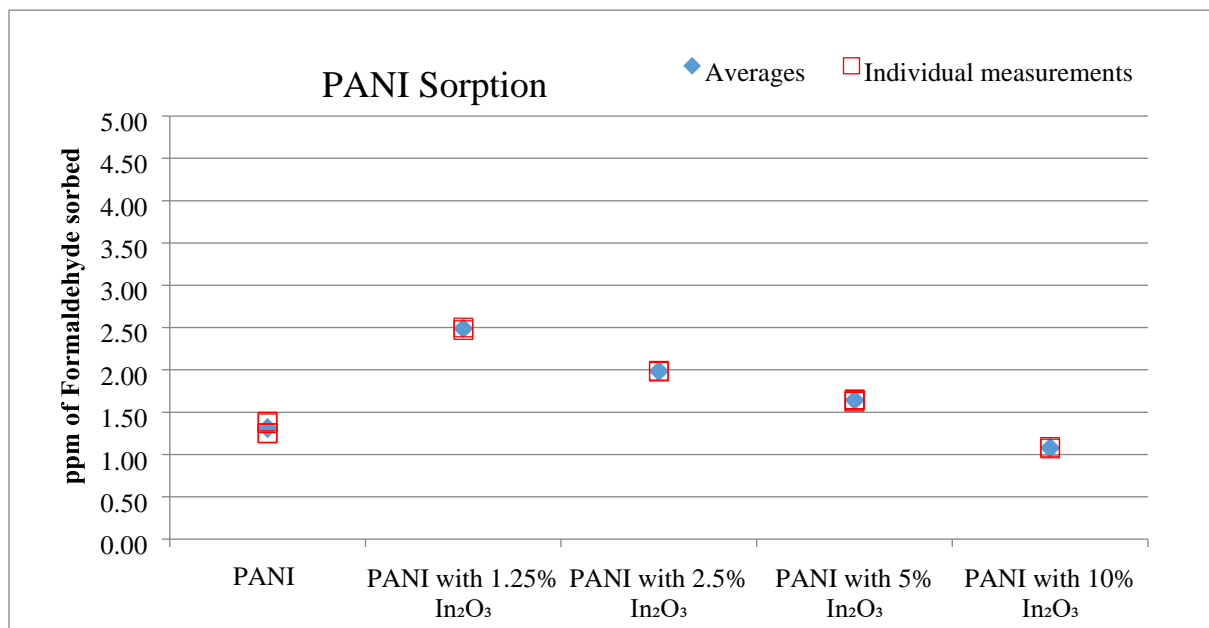


Figure 1 Formaldehyde sorption for undoped and doped PANI (source: F 10 ppm)

It is evident from Figure 1 that the sensitivity of PANI for F increases with a decrease in wt. % of In_2O_3 dopant. To confirm the trends and potential optimality of PANI with 1.25% In_2O_3 for F sorption, PANI with 0.625% In_2O_3 has been synthesized and is currently being evaluated for its

sorption of F. Of course, the trend of increasing F sorption with decreasing wt. % of In_2O_3 could be due to structural differences triggered by the incorporation of the metal oxide.

In parallel, the selectivity of the undoped and doped PANI towards a mixture of F and B was also evaluated. All the polymeric sensing materials were exposed to a mixture of F and B (5 ppm each) for the selectivity studies. Figure 2 shows a typical F and B sorption plot for undoped and doped PANI sensing materials.

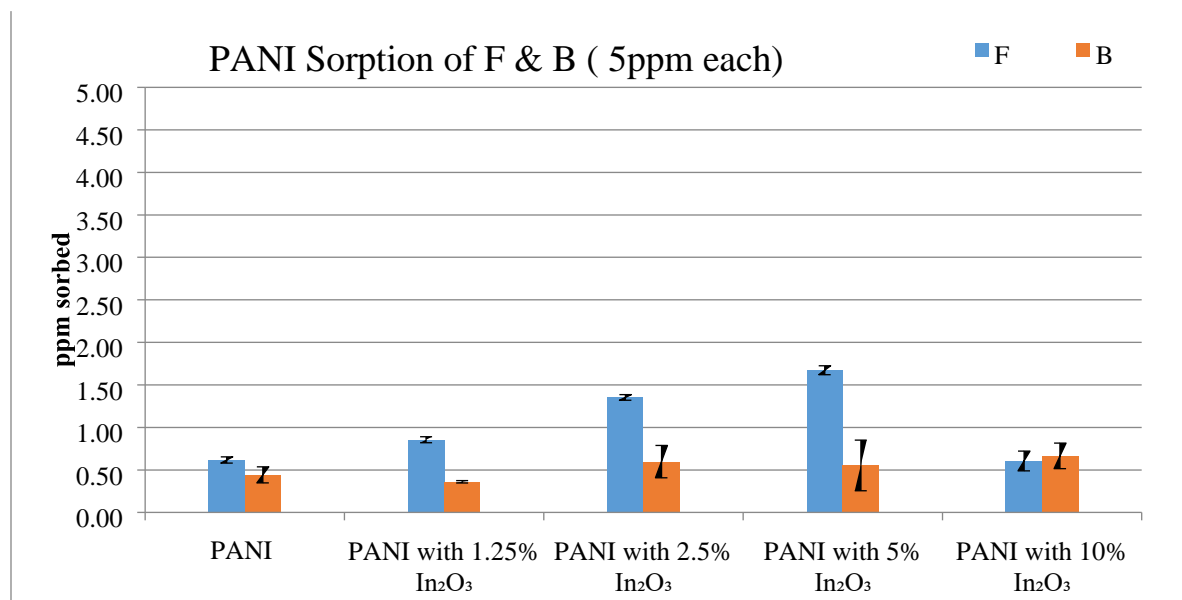


Figure 2 F and B sorption for undoped and doped PANI (source: F/B, 5/5 ppm)

It is quite clear from Figure 2 that PANI with 5% In_2O_3 seems to be optimal with an average selectivity of 3.91 of F over B. Therefore, improvement in sorption of F with a decrease in wt.% of In_2O_3 in PANI from 5% to 1.25% does not stand true for sorption of F from an F/B mix. To further evaluate the sensing material structures and complement the sensitivity and selectivity sorption trends, Scanning Electron Microscopy (SEM) with Energy Dispersive X-Ray Analysis (EDX), and X-ray Diffraction (XRD) studies are being conducted and analyzed. Results from these more recent and ongoing research studies will be presented at the IPR Symposium in May 2021.

References

- [1] "Code of Federal Regulations, 40: Chapter 1, Subchapter C, Part 51, Subpart F, 51100.," EPA. [Online]. [Accessed 8 March 2021].
- [2] P. Aas, "The threat of mid-spectrum chemical warfare agents," *Prehospital and Disaster Medicine*, vol. 18, no. 4, pp. 306-312, 2003.

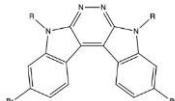
- [3] K. Ganesan, S. K. Raza and R. Vijayaraghavan, "Chemical warfare agents," *Journal of pharmacy and bioallied sciences*, vol. 2, no. 3, pp. 166-178, 2010.
- [4] H. FOLLOWS, "Convention on the prohibition of the development, production, stockpiling and use of chemical weapons and on their destruction," in *Organisation for the Prohibition of Chemical Weapons*, The Hague, The Netherlands, 2005.
- [5] H. Sohn, S. Létant, M. J. Sailor and W. C. Trogler, "Detection of fluorophosphonate chemical warfare agents by catalytic hydrolysis with a porous silicon interferometer," *Journal of the American Chemical Society*, vol. 122, no. 22, pp. 5399-5400, 2000.
- [6] K. M. E. Stewart, N. M. McManus, E. Abdel-Rahman and A. Penlidis, "Doped polyaniline for the detection of formaldehyde," *Journal of Macromolecular Science*, vol. Part A 49, no. 1, pp. 1-6, 2012.
- [7] N. Majdabadifarahani, *Evaluating Polymeric Materials for Sensing of Gaseous Analytes*, Waterloo, ON, Canada: Master's thesis, University of Waterloo, 2019.
- [8] K. M. Stewart and A. Penlidis, "Designing polymeric sensing materials for analyte detection and related mechanisms," *In Macromolecular Symposia*, pp. 123-132, 2016.
- [9] A. Dey, "Semiconductor metal oxide gas sensors: A review," *Materials Science and Engineering*, pp. 206-217, 2018.
- [10] R. Dong, L. Zhang, Z. Zhu, J. Yang, X. Gao, and S. Wang, "Fabrication and formaldehyde sensing performance of Fe-doped In₂O₃ hollow microspheres via a one-pot method," *CrystEngComm*, pp. 562-569, 2017.
- [11] T. Chen, Q. J. Liu, Z. L. Zhou and Y. D. Wang., "The fabrication and gas-sensing characteristics of the formaldehyde gas sensors with high sensitivity," *Sensors and Actuators*, pp. 301-305, 2008.

Daniel Afzal
Chemical Engineering
Waterloo

Synthesis and Characterization of Isopyridazine Derived from Isoindigo

Synthesis and Characterization of Isopyridazine derived from Isoindigo

Presented By: Daniel Afzal
Supervisor: Dr. Yuning Li



1

Overview of Isoindigo

- High yielding and scalable synthesis allows for rapid development for high performance organic electronics (OPV's, OFET's, etc.)
- The combination of low frontier orbital energy, backbone planarity, extended conjugation, large local dipole, good solubility is what makes isoindigo great for high performance



Overview of Isoindigo

PAGE 2



Purpose of Synthesizing Isopyridazine

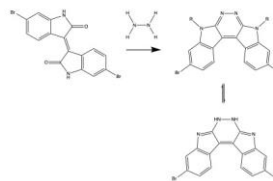
- Novel
- More coplanar than isoindigo
- Contains side chains on one side which may improve the solubility
- LUMO energy maybe higher so it could be used for solar cells
- =N-N= contain pyrazine which may be sensitive to acidic substances and metal ions, so it may be used as chemical sensors

Purpose of Synthesizing Isopyridazine

PAGE 3



Synthesis of Isopyridazine



- The isoindigo reacts with the hydrazine to give pyrazines in tautomeric form
- Avoid formation of isomer where the proton can be on the pyridazine disrupting coplanarity

Synthesis of Isopyridazine

PAGE 4



References

- Stalder, R., Mei, J., Graham, K. R., Estrada, L. A., & Reynolds, J. R. (2013). Isoindigo, a versatile electron-deficient unit for HIGH-PERFORMANCE ORGANIC ELECTRONICS. *Chemistry of Materials*, 26(1), 664-678. doi:10.1021/cm402219v
- Sattar, A. S., & Atta-Allah, S. (2008). Synthesis and Reactivity of Isoindigo: A Revisit. *AFINIDAD LXV*, 534, Marzo-Abril 2008.
- 25th Anniversary Article: Isoindigo-Based Polymers and Small Molecules for Bulk Heterojunction Solar Cells and Field Effect Transistors Deng, P., & Zhang, Q. (2014). Recent developments on isoindigo-based conjugated polymers. *Polym. Chem.*, 5(10), 3298-3305. doi:10.1039/c3py01598j

References

PAGE 5



Thank You For Listening

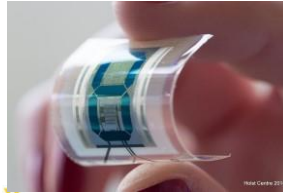
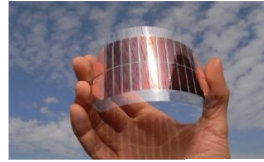
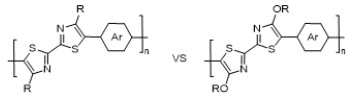


6

Javan Buratynski
Chemistry
Waterloo

Tuning the Bandgap of Bithiazole Based Polymers

Tuning the Bandgap of Bithiazole Based Polymers



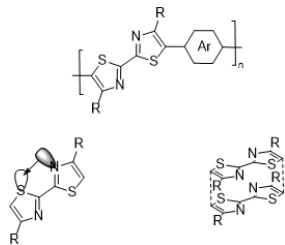
Javan Buratynski

2

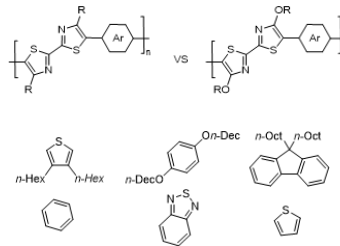
Thiazoles

Objective

- Bithiazoles exist as a promising backbone for conductive polymers

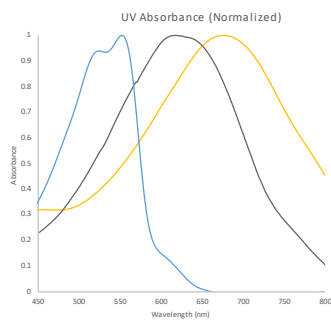


- Observe the differences in polymer size and band gap through the modification of spacers and side chains



Results

Acknowledgements



- Thanks to:
- Rafael Mirabel
 - Jianan Wang
 - Boris Nazareth
 - Mila Abaeva
 - Geoff Sinclair
 - Emily Verkuil
 - Lukas Glofcheskie



- Special Thanks to:
- Dr. Derek Schipper
 - Dr. Jean Duhamel
 - Kim Rawson

Yunsheng Jiang
Chemical Engineering
Waterloo

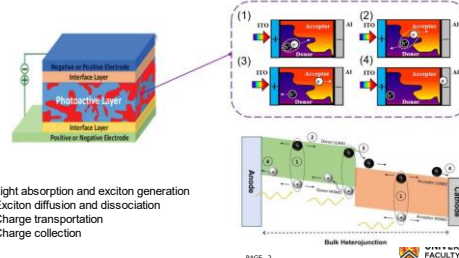
A Conjugated Polymer Donor Based on
Alkyloxime Substituted Thiophene for BHJ
Organic Solar Cells

A Conjugated Polymer Donor based on Alkyloxime Substituted Thiophene for BHJ Organic Solar Cells

Yunsheng (Belle) Jiang
 Supervisor: Yuning Li
 March 25th, 2021

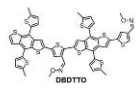


Bulk Heterojunction OSC Working Mechanism

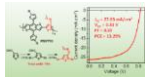


Design Rationale

Objective: To improve the planarity and lower the energy loss of DBDFTO

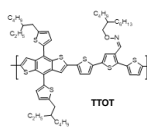


- Twisted polymer backbone
- Considerable energy loss
- PCE: 13.3%



- BDT unit (D unit)**
 - Rigid and planar molecular structure
 - favorable for achieving high hole mobility
 - facile side chains
 - tunable bandgaps and energy level

D- π -A type

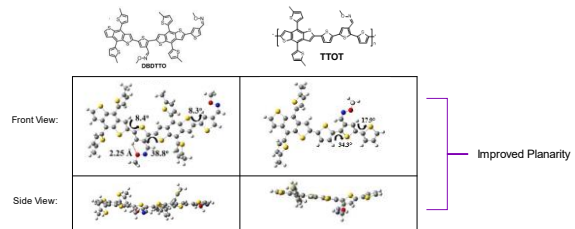


- Thiophene unit (D unit)**
 - π - π bridge
 - improve planarity and reduce steric hindrance
 - hole mobility enhancement

- Branched Alkyloxime (A unit)**
 - electron-withdrawing group
 - readily synthesized



DFT Simulations:



Optical and Electrochemical Properties:

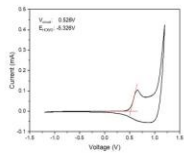


Figure 1. Cyclic voltammetry of TTOT film.

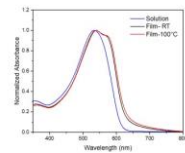


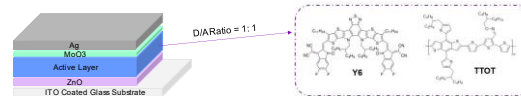
Figure 2. UV-vis absorption spectra of the RT & 100°C annealed TTOT film and chloroform solution

Polymer	λ_{max} (nm)	λ_{onset} (nm)	E_g^{opt} (eV)	E_{HOMO} (eV)	E_{LUMO} (eV)
TTOT	539, 570	627	1.98	-5.33	-3.35

Table 1. Optical and electrochemical properties of TTOT12.



Photovoltaic Performance:



Solvent	Temperature	Thickness (nm)	J_{sc} (mA/cm ²)	V_{oc} (V)	FF	PCE (%)
CF	RT	180	20.57	0.66	0.44	6.00
CF	RT	108	23.58	0.62	0.52	7.65
CF	RT	100	21.34	0.63	0.54	7.29
CB	RT	105	17.03	0.57	0.59	5.77
CF	100°C-20min	95	21.96	0.59	0.49	6.24

Table 2. Photovoltaic parameters of the OSCs based on TTOT:Y6.

- Possible Improvements
 - Measure SCLC mobility and improve D/A ratio
 - Lower the HOMO of TTOT by polymerize the monomer with fluorinated BDT



Xiguang Gao
Chemical Engineering
Waterloo

An In-Situ Formed Conductive Polymer for Enhancing the Performance of Li-S Batteries

An In-situ Formed Conductive Polymer for Enhancing the Performance of Li-S Batteries

Xiguang Gao

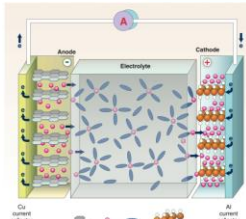
PhD Candidate, Department of Chemical Engineering

Supervisor: Prof. Yuning Li

May 5, 2021



Current Li-ion Batteries



Intercalation cathode materials	Specific capacity (mAh g ⁻¹) (theoretical/commercial)
LiTFSi ₂	225/210
LiCoO ₂	274/145
LiNi _{0.33} Mn _{0.33} Co _{0.33} O ₂	280/160
LiNi _{0.47} Co _{0.07} Al _{0.46} O ₂	279/199
LiMn ₂ O ₄	148/120
LiFePO ₄	170/165

Nitta et al., Mater. Today, 2015, 18, 252-264

- Capacities approaching the theoretical limits
- High cost of Co, Ni, Mn, etc.



Dunn et al., Science, 2011, 334, 928-935

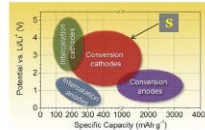
2

Demand for Clean Energy Sources

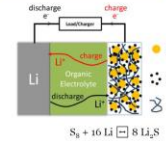


1

Lithium-sulfur (Li-S) Batteries



Nitta et al., Mater. Today, 2015, 18, 252-264



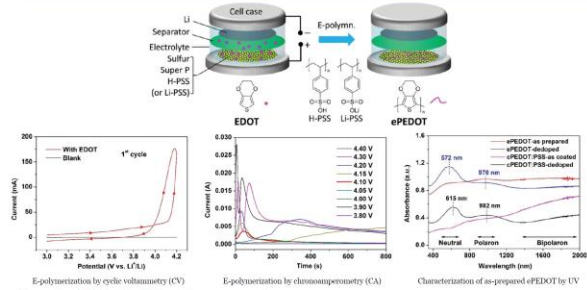
Manthiram et al., Chem. Rev., 2014, 114, 11751-11787

- Pros**
 - Ultrahigh specific capacity (1672 mAh g⁻¹) and specific energy (2567 Wh kg⁻¹)
 - Natural abundance and low cost
 - Environmental friendliness
- Cons**
 - Drastic capacity fading due to the dissolution of lithium polysulfide intermediates
 - Low electrical conductivity of sulfur



3

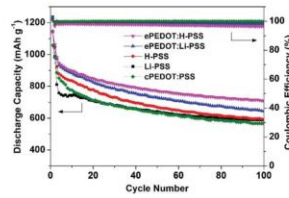
Formation of PEDOT by electro-polymerization (e-polymerization)



Xiguang Gao and Yuning Li, et al. Mater. Adv., 2021, 2, 974-984

4

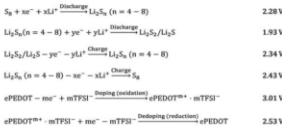
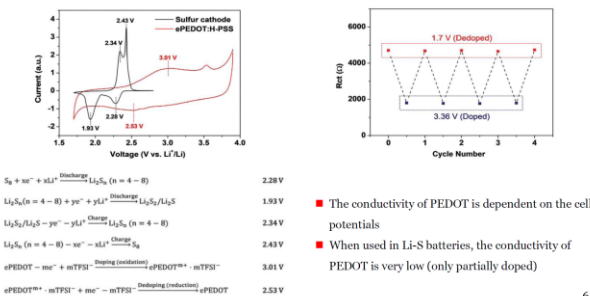
Performance of Li-S batteries with the in-situ formed PEDOT:PSS



- Improved capacity retention with ePEDOT
- The as-formed ePEDOT:H-PSS is better than commercial cPEDOT:PSS

5

Conductive polymers for Li-S batteries – Conductive or Not?



- The conductivity of PEDOT is dependent on the cell potentials
- When used in Li-S batteries, the conductivity of PEDOT is very low (only partially doped)

6

THANK YOU



Yi Yuan
Chemical Engineering
Waterloo

Designing Low-cost Polymer Donor for High
Performance Non-fullerene Acceptor Based
Organic Solar Cells

Designing low-cost polymer donor for high performance non-fullerene acceptor based organic solar cells

Presenter: Yi Yuan
 Supervisor: Prof. Yuming Li
 Date: May 5th, 2021

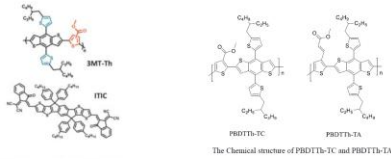


Table 1. Summary of the photovoltaic parameters of the OSCs investigated in this study.

Device	Substrate	TC	TA	TC	TA
PBDTh-TC	ITO/Ag	18.43 (18.43)	19.0 (19.0)	19.2 (19.2)	19.2 (19.2)
PBDTh-TA	ITO/Ag	19.1 (19.1)	19.0 (19.0)	19.0 (19.0)	19.0 (19.0)
ITIC	ITO/Ag	19.0 (19.0)	19.0 (19.0)	19.0 (19.0)	19.0 (19.0)
BMT-Th	ITO/Ag	19.0 (19.0)	19.0 (19.0)	19.0 (19.0)	19.0 (19.0)
ITIC	ITO/Ag	19.0 (19.0)	19.0 (19.0)	19.0 (19.0)	19.0 (19.0)
BMT-Th	ITO/Ag	19.0 (19.0)	19.0 (19.0)	19.0 (19.0)	19.0 (19.0)
ITIC	ITO/Ag	19.0 (19.0)	19.0 (19.0)	19.0 (19.0)	19.0 (19.0)
BMT-Th	ITO/Ag	19.0 (19.0)	19.0 (19.0)	19.0 (19.0)	19.0 (19.0)
ITIC	ITO/Ag	19.0 (19.0)	19.0 (19.0)	19.0 (19.0)	19.0 (19.0)
BMT-Th	ITO/Ag	19.0 (19.0)	19.0 (19.0)	19.0 (19.0)	19.0 (19.0)

Reference: Energy Mater. 2017, 7, 1700566.



Photovoltaic performance

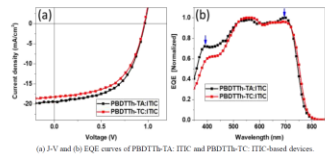


Table. Photovoltaic parameters of PBDTh-TA/ITIC and PBDTh-TC/ITIC.

Active layer	Solvent	J _{sc} (mA/cm ²)	V _{oc} (V)	FF	PCE (%)
PBDTh-TA/ITIC	DCB	19.43	0.96	0.56	10.47
PBDTh-TA/ITIC	Xylene	19.63	0.98	0.51	9.76
PBDTh-TC/ITIC	DCB	18.23	0.96	0.55	9.68



Organic Solar Cell:

- Low-cost
- Lightweight
- Flexible
- Large-area fabrication

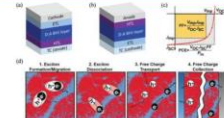


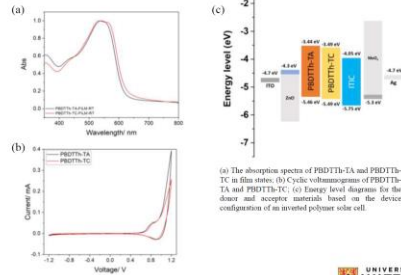
Fig. 1 (a) Conventional and (b) inverted OSC architectures. (c) solar cell figures-of-merit: short-circuit current density (J_{sc} , mA cm⁻²), open-circuit voltage (V_{oc} , V), fill factor (FF) and PCE (%) and (d) working mechanism of the BDT layer in OSCs (red and blue areas represent donor and acceptor domains, respectively).¹⁰ Reproduced from ref. 42 with permission from John Wiley and Sons, copyright 2019.



Fig. 2. Chemical structures of representative D and A building blocks used for high-performance D-A polymers, where R₁ or R₂ is a side chain (hydrogen, alkyl, alkoxy, aliphatic and aryl groups, etc.) and n or m is an appropriate integer.



Physicochemical properties



UNIVERSITY OF WATERLOO



THANK YOU

Lukas Bauman
Chemical Engineering
Waterloo

The Development and Characterization of 3D Printable Double-network Hydrogels

The development and characterization of 3D Printable Double-network Hydrogels

Lukas Bauman

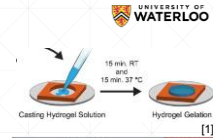
Surface Science and Bio-nanomaterial Lab
 Supervisor: Boxin Zhao
 Department of Chemical Engineering, University of Waterloo



Motivation

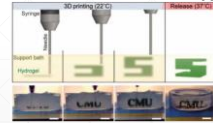
Hydrogels

- Casting → limited geometries
- 3D Printing → limited by hydrogel strength and machine cost



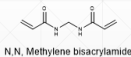
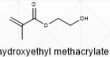
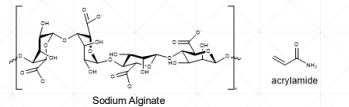
Strong hydrogel fabrication with consumer grade 3D printers has seen significant growth recently

- Sodium Alginate is used to reinforce the hydrogel for casting but its viscosity and solubility limits use in resin 3D printers

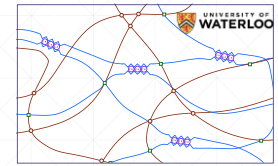
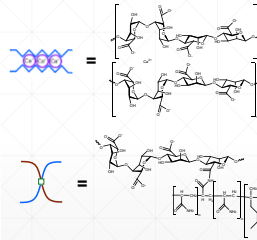


Lukas Bauman
 [1] LeGendre, B. L.; Saha, N. A.; Miel, C. M.; Halilovic, S. C. Production of Elastin-like Protein Hydrogels for Encapsulation and Immunostaining of Cells in 3D. *Adv. Mater.* 2019, No. 19, 57736.
 [2] Li, H.; Tan, C.; Li, L. Review of 3D Printable Hydrogels and Constructs. *Materials & Design* 2018, 159, 35–58. <https://doi.org/10.1016/j.matdes.2018.08.033>

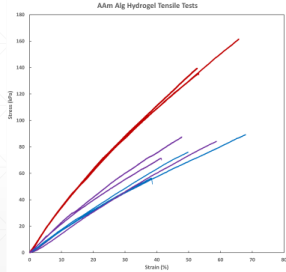
Resin Formulation



Theory

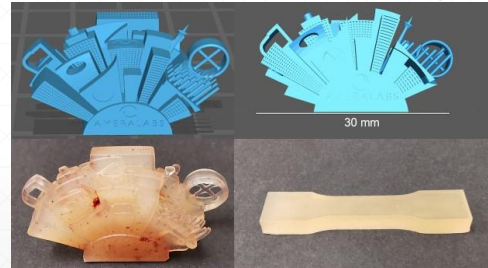


Acrylamide Hydrogel Formulations



Resin (Monomer:Alginate)	AA80:20	AA85:15	AA90:10
Cure time (s)	60 s	50s	40s
Youngs Modulus (kPa)	172 kPa	230 kPa	353 kPa
Ultimate Tensile Stress (kPa)	90±4.6	75±16 kPa	142±13 kPa
Ultimate Tensile Strain	62±7.0%	47±9.3%	56±6.3%
Swelling Volume	246%	223%	204%
Swelling Weight	200%	240%	210%

Fabrication Capability



Jun-Zhi (Oliver) Wang
Chemistry
Waterloo

pH Responsive Polypeptides for Drug Delivery

pH-Responsive Polypeptides for Drug Delivery

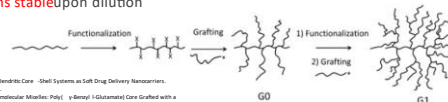
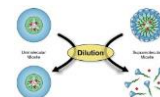
JUN -ZHI (OLIVER) WANG

SUPERVISED BY: DR. MARIO GAUTHIER



Polymer Micelles for Drug Delivery

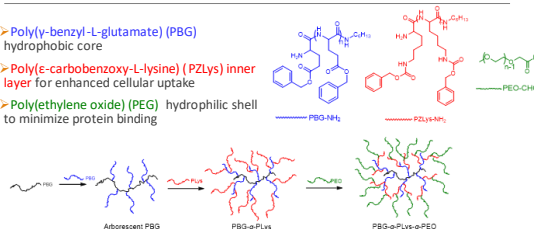
- > **Block copolymers**
 - > Aggregation through **hydrophobic interactions**
 - > **Dissociate** below the critical micelle concentration
- > **Arborescent copolymer micelles**
 - > Micelle structure maintained by **covalent bonds**
 - > **Remains stable** upon dilution



Ikawa, M. C.; Thota, B. S.; Wang, J. Dendritic Core-Shell Systems as Soft Drug Delivery Nanocarriers. *Biomaterials* 2015, 37 (2), 1227-1240.
Gauthier, M.; Whitten, G. Arborescent Ultramolecular Micelles: Poly(γ -Benzyl-L-Glutamate) Core Grafted with a Hydrophilic Shell by Copper(I)-Catalyzed Atom Transfer Radical Copolymerization. *Polymers* 2017, 8, 549.

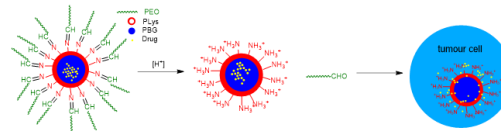
Arborescent Micelles for Drug Delivery

- > **Poly(γ -benzyl-L-glutamate) (PBG)** hydrophobic core
- > **Poly(ϵ -carbobenzoxy-L-lysine) (PZLys) inner layer** for enhanced cellular uptake
- > **Poly(ethylene oxide) (PEG)** hydrophilic shell to minimize protein binding



pH-Responsive Drug Release

- > Many tumour cells produce a slightly **acidic environment**
- > Imine bond allows **pH-stimulated cleavage** of the PEO shell for enhanced cell membrane penetration and targeted drug release at tumour sites
- > Positive charge on exposed lysine side chains **enhances cellular uptake**



Characterization

Polymer Sample	M_n (MALLS)	M_w/M_n	f_n	C_p (%)	G_p (%)
Linear PBG	5100	1.07	--	--	--
G0PBG	3.3×10^4	1.08	4.2	40	60
G0PBG-g-PZLys	1.2×10^5	1.09	16.3	52	54
G1PBG	1.2×10^5	1.07	16.6	53	44
G1PBG-g-PZLys	4.7×10^5	1.07	76.6	46	44

C_p : Coupling efficiency, G_p : Grafting Yield, f_n : branching functionality

- > **Rapid increase of molecular weight** over successive generations
- > **Narrow molecular weight distribution** maintained up to the G2 polypeptide

Future Work and Acknowledgements

- > **Future Work**
 - > Coupling of **aldehyde-terminated PEO shell** with arborescent polypeptides
 - > Characterization by **dynamic light scattering** and **zeta-potential** measurements
 - > Study the **pH-stimulated cleavage** of the PEO shells
- > **Acknowledgements**
 - > Professor Mario Gauthier
 - > Gauthier Lab Members

Abdullah Basalem
Chemistry
Waterloo

Characterization of Gemini Surfactants and
their Interactions with DNA by PEF

Characterization of Gemini Surfactants as they Interact with DNA by PEF

Abdullah Basalem, and Jean Duhamel

Institute for Polymer Research, Waterloo Institute for Nanotechnology, Department of Chemistry, University of Waterloo, Waterloo, Ontario, Canada, N2L 3G1

INTRODUCTION

Gemini surfactants have attracted considerable scientific attention due to their unique structure and properties. Their structure resemblance to cell membrane lipids makes them ideal candidates as non-viral vectors for DNA delivery.¹⁻² A major challenge in gene therapy is the transport of therapeutic genes across the lipid membranes of the proper cells for gene expression.³ To better determine the behavior of the surfactant in complexes made of gemini surfactants and DNA, two pyrene-labeled gemini surfactant were synthesized and their fluorescence was characterized.⁴ These experiments took advantage of the ability of an excited pyrene to form an excimer upon encounter with a ground-state pyrene. The interactions of two pyrene substituted gemini surfactants (Py-3-12) and (PyO-3-12) with calf thymus (CT) DNA led to excimer formation, which reflected their aggregation along the DNA backbone. These interactions were studied using steady-state and time-resolved fluorescence. Model free analysis (MFA) was used to analyze the fluorescence decays for the solutions of DNA and gemini surfactants. The main results of this fluorescence study indicate that the nature of the surfactant clusters generated along the DNA backbone remained the same regardless of the amount of surfactant bound to the DNA. Increasing the DNA concentration did not lead to a disaggregation of the surfactant clusters; rather it simply resulted in the dilution of the surfactant clusters along the DNA backbone, with the surfactant clusters retaining the same structure.

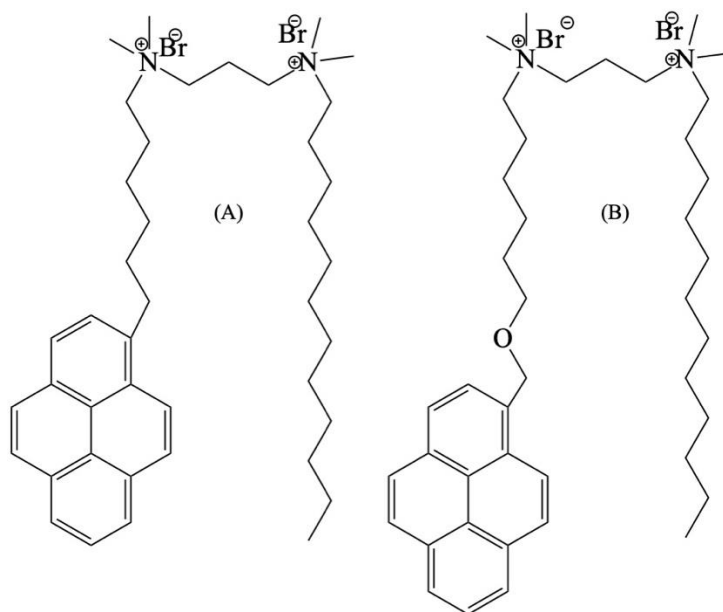


Figure 1. Structures of (A) Py-3-12 and (B) PyO-3-12.

EXPERIMENTAL

Materials: All chemicals were purchased from Sigma-Aldrich Canada. All solvents were HPLC grade. Water was obtained from a Millipore Milli-Q filtration system.

Steady-state Fluorescence: Steady-state fluorescence spectra were acquired with a Photon Technology International (PTI) spectrofluorometer using an Ushio UXL-75Xe Xenon lamp and a PTI 814 photomultiplier detection system. The samples were excited at 344 nm and their fluorescence intensity was scanned from 350 to 600 nm. The I_E/I_M ratio was calculated by dividing the area underneath the excimer fluorescence signal from 500 to 530 nm to yield I_E by the area underneath the first monomer fluorescence peak from 372 to 378 nm to yield I_M .

Time-resolved fluorescence: The fluorescence decays of the pyrene monomer and excimer were acquired on an IBH time-resolved fluorometer using a 340 nm *nanoLED* to excite the solutions and monitoring the fluorescence intensities for the pyrene monomer and excimer at 375 and 510 nm, respectively. The monomer and excimer decays were fitted globally using the Model Free Analysis (MFA).

RESULTS AND DISCUSSION

The interactions between DNA and the pyrene-labeled gemini surfactants in solution were probed by taking advantage of the ability of an excited pyrene to form excimer upon encounter with a ground-state pyrene. The concentration (0.1 mM) of the two surfactants was kept below their CMC so that the observation of pyrene excimer formation (PEF) upon adding DNA to the surfactant solution could only be the results of surfactants, that would bind to and cluster on DNA. The (-/+) ratio was used to express the concentration of DNA, which ranged from 0.01 to 1.15 mM, to that of the gemini surfactants equal to 0.1 mM. The SSF spectra of these solutions were analyzed to calculate the I_E/I_M ratios, which were plotted against the (-/+) ratio. Figure 2 shows the I_E/I_M ratios, that were determined from the analysis of the SSF spectra and from the MFA of the TRF decays for both surfactants Py-3-12 and PyO-3-12. The shape of the two I_E/I_M traces were similar, with I_E/I_M taking a low value at low (-/+) ratios, where the surfactants were unassociated and could not form excimer, before shooting up as the (-/+) ratio approached unity, corresponding to an equimolar [DNA]:[GS] ratio. For (-/+) ratios larger than unity, the I_E/I_M ratio remained large and somewhat constant. The good agreement observed between the I_E/I_M ratios obtained by SSF and TRF suggested that the parameters obtained by TRF reflected accurately the photophysical processes that led to the SSF spectra.

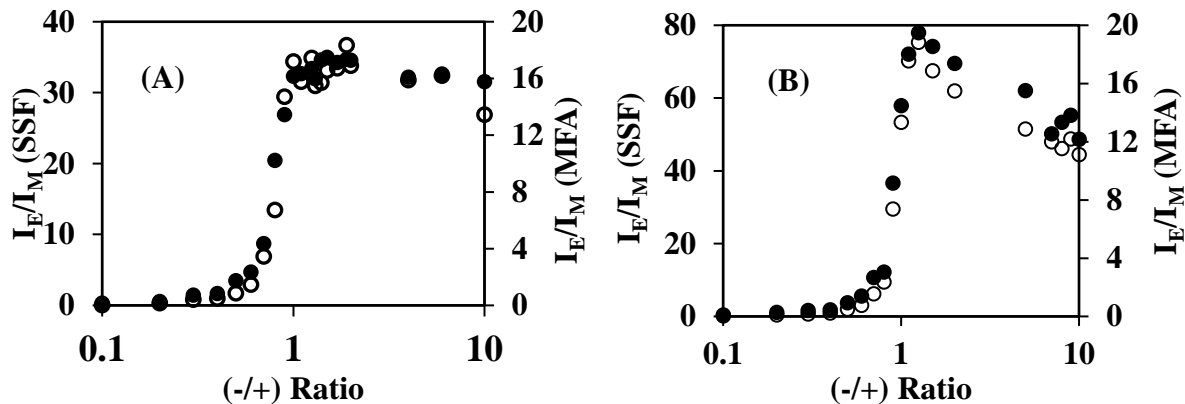


Figure 2. Plot of I_E/I_M from the analysis of the SSF spectra (hollow) and I_E/I_M from the MFA of the TRF decays (solid) as function of the (-/+) ratio for (A) Py-3-12 and (B) PyO-3-12.

Figure 3 shows the average rate constant of excimer formation $\langle k \rangle$ obtained from the MFA of the fluorescence decays for both surfactants Py-3-12 and PyO-3-12. $\langle k \rangle$ for both surfactants is more or less constant throughout the entire range of (-/+) ratios where it averages $0.25 \pm 0.02 \text{ ns}^{-1}$ and $0.20 \pm 0.04 \text{ ns}^{-1}$ for Py-3-12 and PyO-3-12 respectively. The constancy of $\langle k \rangle$ indicates that pyrene resides in the same microenvironment at all DNA concentrations. This result suggests that the nature of the surfactant aggregates, that are generated along the DNA as the surfactants bind to the DNA, are the same at all DNA concentrations, regardless of whether the DNA concentration is below or above the equimolar point. It suggests that even at high DNA concentration, where the surfactants are more sparsely distributed along the DNA backbone, they cluster in a same manner as when they are present in large excess at low (-/+) ratios.

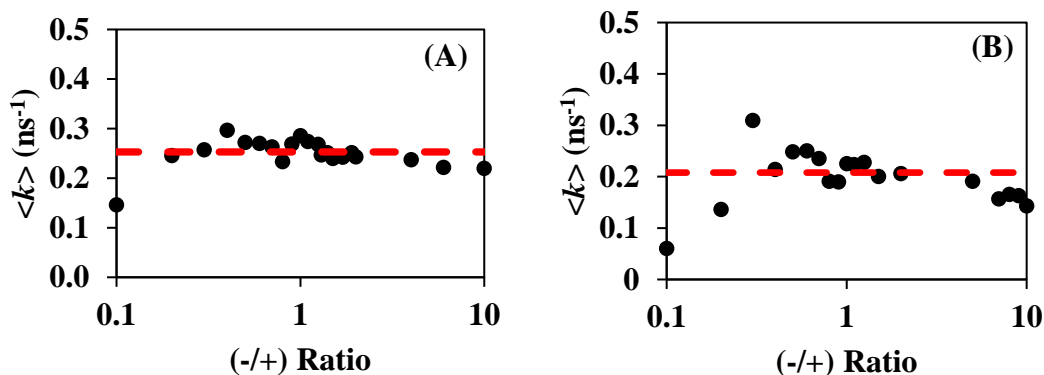


Figure 3. Plots of $\langle k \rangle$ as a function of the (-/+) ratio for (A) Py-3-12 and (B) PyO-3-12.

Finally, Figure 4 shows the molar fractions of the pyrene species, that are involved in PEF, namely the fractions f_{free} (solid circles), f_{diff} (empty circles), and f_{agg} (crosses) of pyrenyl labels that are free, cannot form excimer, and represent the unassociated surfactants, that are forming excimer by diffusive encounters, and that are aggregated, respectively, as a function of the (-/+) ratio. At low (-/+) ratios, most surfactants are unassociated, f_{free} is large, and f_{diff} and f_{agg} are small. As the (-/+) ratio increases and the surfactants bind to and cluster on DNA, f_{free} decreases until it reaches

zero for (-/+) ratios larger than unity. f_{diff} and f_{agg} increase with increasing (-/+) ratio as the surfactants bind to DNA and generate surfactant clusters that are the loci for PEF, before plateauing for (-/+) ratios larger than unity. This result also supports the conclusion that as the DNA concentration is increased past a (-/+) ratio of 1 and the surfactants become sparsely distributed along the DNA backbone, they form excimer in the same manner with the same $\langle k \rangle$, f_{diff} , and f_{agg} values indicating that they are generating the same surfactant clusters at low and high (-/+) ratios.

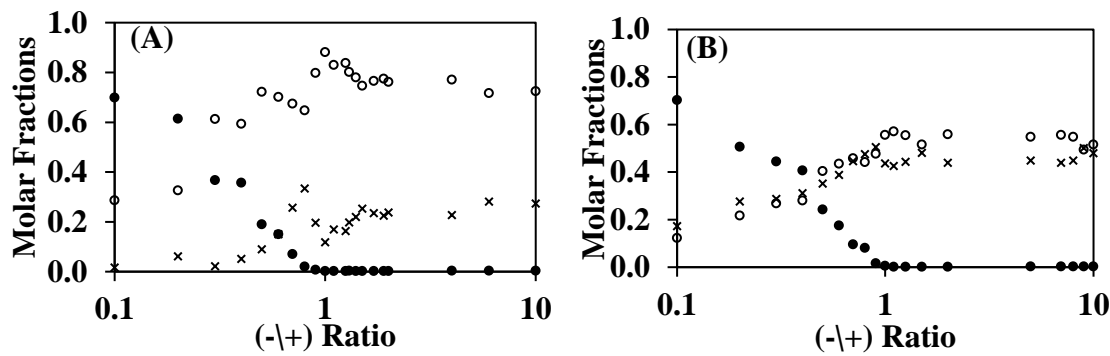


Figure 4. Plots of the molar fractions (●) f_{free} , (○) f_{diff} , and (×) f_{agg} as a function of the (-/+) ratio for surfactants (A) Py-3-12 and (B) PyO-3-12.

CONCLUSIONS

The interactions between two pyrene-labeled gemini surfactants and DNA were probed using pyrene excimer fluorescence. SSF and TRF experiments yielded the I_E/I_M curves as a function of the (-/+) ratio shown in Figure 2. Both curves showed similar profiles, which indicated good agreement between the two techniques. MFA of the TRF decays yielded the molar fractions of the different pyrene species in solution and the average rate constant of excimer formation. Their constant values obtained for (-/+) ratios larger than unity indicate that as the DNA concentration is increased past the equimolar point and the surfactants become more diluted along the DNA backbone, they generate the same environment with a constant level of PEF. It thus suggests, that the density of surfactant clusters along the DNA backbone decreases with increasing (-/+) ratio, but that the nature of the surfactant clusters does not change.

REFERENCES

1. Menger, F. M.; Littau, C. A. Gemini Surfactants: Synthesis and Properties. *J. Am. Chem. Soc.* **1991**, *113*, 1451-1452.
2. Kirby, A. J.; Camilleri, P.; Engberts, J. B. F. N.; Feiters, M. C.; Nolte, R. J. M.; Söderman, O.; Bergsma, M.; Bell, P. C.; Fielden, M. L.; Garcia Rodriguez, C. L.; Guédat, P.; Kermer, A.; McGregor, C.; Perrin, C.; Ronsin, G.; van Eijk, Gemini Surfactants: New Synthetic Vectors for Gene Transfection. *Angew. Chem. Int. Ed.* **2003**, *42*, 1448-1457.
3. Wolff, J. A. The “Grand” Problem of Synthetic Delivery. *Nat. Biotechnol.* **2002**, *20*, 768 – 769.
4. Wang, C.; Wettig, S. D.; Foldvari, M.; Verrall, R. E. Synthesis, Characterization, and Use of Asymmetric Pyrenyl-Gemini Surfactants as Emissive Components in DNA-Lipoplex Systems. *Langmuir* **2007**, *23*, 8995–9001.

Dr. Valerie Farrugia
Senior Researcher
Xerox

The 2D and 3D Printing of Engineered Particles

The 2D and 3D Printing of Engineered Particles

**Valerie Farrugia MASC
Senior Research Scientist
Xerox Research Centre of Canada**

Valerie joined Xerox in 1998. She received her Bachelor of Science from Ryerson University in 1995 followed by her Master of Applied Science from University of Toronto in the area of Environmental Engineering for the Pulp and Paper Industry in 1998. Valerie currently holds 136 U.S patents related to imaging materials and processes. Valerie's first assignment within Xerox involved aqueous-based inkjet development. She transferred to Emulsion Aggregation (EA) toner technology in 2000. In 2007, she started working on polymer synthesis for next generation EA toners. Valerie earned her Design for Lean Six Sigma (DfLSS) Black Belt certification in 2009, completing several key studies for a low melt toner project, as well as training in Project Management. Her interests include emulsion polymerization (EP), nanocomposite material design and functional polymers. Her most recent work involves the design of engineered particles for additive manufacturing. She is currently leading a team of scientists to deliver innovative and cutting-edge materials for 3D printing.

The 2D and 3D Printing of Engineered Particles

Established in the Toronto suburb of Mississauga, Ontario, in 1974, Xerox Research Centre of Canada has Xerox' global mandate for materials innovations. After 47 years, this laboratory continues to help push the boundaries of advanced materials science in Canada. With the 3D printing materials market undergoing enormous growth in the past 5 years, materials research in this area is a natural transition from the 2D material development for the researchers at XRCC. There is an opportunity for Xerox to provide high value 3D printing materials to this market to meet the requirements of end-use applications such as automotive and aerospace. XRCC's focus is to apply polymer and particle expertise to this emerging market with particular interest in selective laser sintering (SLS) powders. The range of polymers used in the additive manufacturing space is vast and expands beyond thermoplastics to thermosets, elastomers, hydrogels and composites. Conventional particle processing methods such as cryomilling produce roughly shaped particles but XRCC has developed a process to form spherical particles directly from a variety of polymeric materials. In some cases, speciality additives are incorporated into the particle design for processing, stability and flow. To serve specific application areas, particles are designed with certain functionality, including surface finish, porosity and mechanical properties. This talk will describe some of the key material innovations XRCC has used to design and produce engineered particles for the 3D printing revolution.

Audren Marquez
Chemistry
Waterloo

The Role of Water in Self-Assembly

Water as an assembling component in aqueous assemblies

Abstract: Self-assembled vesicles that contain structured (tetrahedral order with strong hydrogen bonds) interstitial water in the membrane was studied. Hydrophobic FpR ((Fp = Fe(CO)(CO-)(C₅H₄)(PPh₃)) (R= C₆, C₆Pyrene, C₃Bithiophene)) self-assemble into metal carbonyl vesicles (MCsomes) with Fp exposed to water and R groups associated into the vesicular membrane. Water interacts with the CO groups in the Fp head. This is due to the water carbonyl interaction of the CO groups, which is supported by the negative zeta potential through cyclic voltammetry (CV) analysis. The R groups are quite distant and are only slightly in contact as analyzed previously through FTIR and CV. Moreover, FpR MCsomes swell over time in where a longer alkyl chain has smaller degrees of swelling. Therefore, the possible absence of conventional hydrophobic interactions in MCsomes was investigated.

The water structure was examined using Raman spectroscopy with the data analyzed by HAMAND (hypothetical addition multivariate analysis with numerical differentiation), which allows the comparison of the spectrum of water against the spectrum of FpC₆Pyrene MCsomes in water as seen in figure 1a). As seen in the figure, there are differences in the Raman spectrum in where FpC₆Pyrene MCsomes in water have a much higher amount of tetrahedrally coordinated water at 3250 cm⁻¹ in comparison to nontetrahedral coordinated water at 3400 cm⁻¹. Furthermore, the presence of a peak at 3600 cm⁻¹ is attributed to interactions between the dangling -OH of water and the non-polar aromatic group suggesting a clathrate-like interstitial water surrounding the non-polar pyrene group in the membrane. To further investigate this, fluorescence analysis was done in where the pyrene group is used as a probe for hydrophobic collapse. As seen in figure 1b, there is an absence of an excimer peak at 460 nm suggesting no hydrophobic collapse occurring in the assembly. Analysis via TEM further supports this as FpC₆ MCsomes cannot be imaged using conventional TEM, while the FpC₆Pyrene MCsomes can be imaged due to the

increased π - π interaction upon the removal of water, which is caused by the hydrophobic collapse. Thus, Raman spectroscopy of FpC₆Pyrene MCsomes in water suggests the presence of interstitial water within the membrane while fluorescence analysis suggests the absence of hydrophobic collapse. This shows that conventional hydrophobic interactions are absent in MCsomes while the interstitial water remains an integral part of the vesicular membrane.

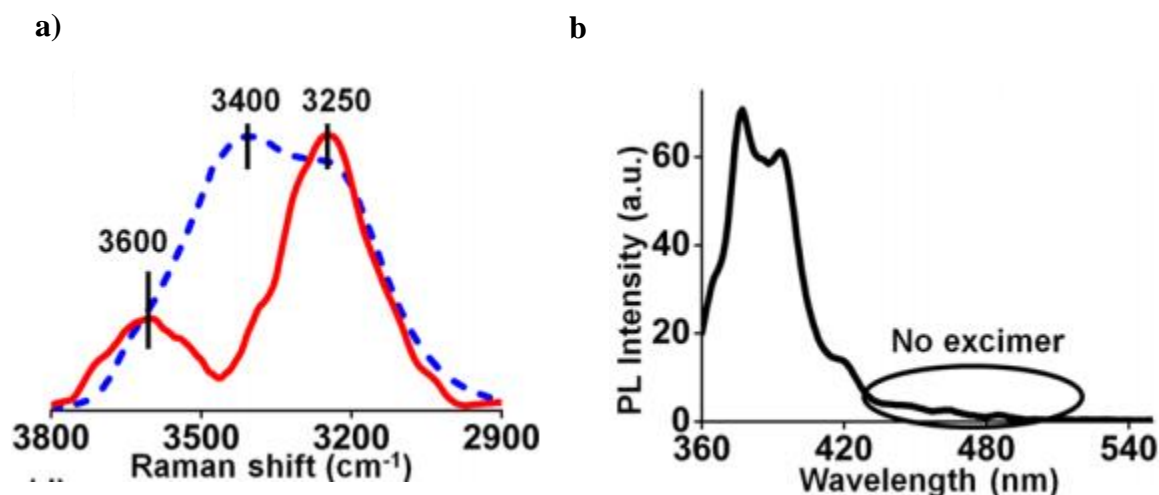


Figure 1: a) Raman spectroscopy of water (blue), and the resulting solute-correlated (SC) spectrum for FpC₆Pyrene MCsomes in water shows the difference in water structure. b) The fluorescence spectrum of FpC₆Pyrene MCsomes in water that shows the absence of the excimer peak, which suggests no hydrophobic collapse.

To further investigate the interstitial water in the membrane of MCsomes, the various FpR MCsomes in water were aged over time to investigate their stability as seen in figure 2a. As seen in the figure, the stability of the MCsomes is dependent on the R group. To further investigate this, Raman spectroscopy followed by HAMAND analysis was done on the various FpR MCsomes in water. As seen in figure 2b, the SC spectrum of various FpR MCsomes are different from each other. This suggests that there are differences in the water structure of the interstitial water, which is attributed to the hydrophobicity of the R group. The differences in water structure are influential and crucial to the overall stability and swelling behaviour of the MCsomes.

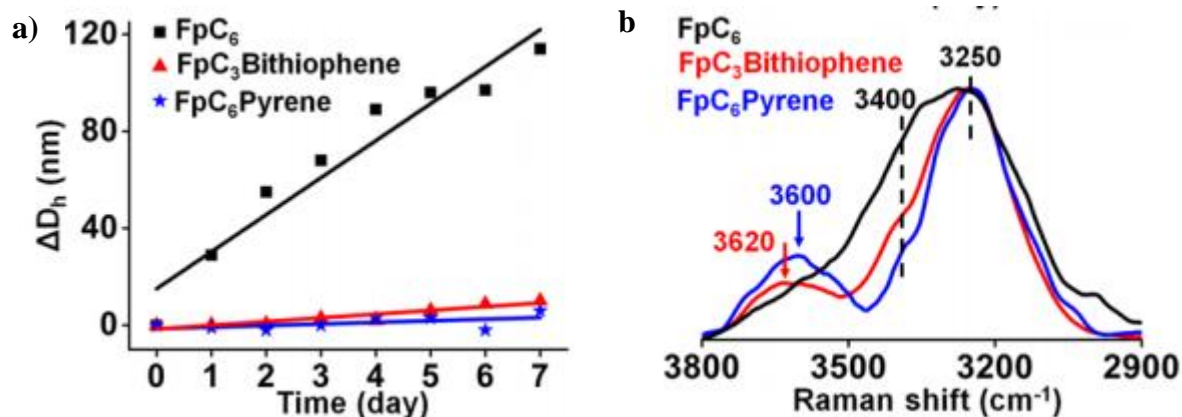


Figure 2: a) DLS analysis of various FpR MCsomes in water over time suggests that the swelling behaviour of MCsomes is dependent on the R group present. b) Raman spectroscopy of SC spectrum for various FpR MCsomes in water. The variation in the SC spectrum suggests that the interstitial water is influenced by the R-group.

The interstitial water in the membrane of the FpR MCsomes can be used to influence the fluorescence of the R-group as demonstrated by FpC₃Bithiophene MCsomes. The interstitial water of FpC₃Bithiophene MCsomes was varied through variations in removal and addition of THF, and variations in UV-irradiation times. The intramolecular rotation of the bithiophene group was found to be fixed at a relative position depending on the interstitial water, which gave rise to through-space conjugation (TSC). This suggests that the intramolecular rotation of the bithiophene group was influenced by the overall strength of the interstitial water.

Overall, FpR MCsomes in water was discovered to contain interstitial water in the membrane. The interstitial water was investigated and its strength is dependent on the hydrophobicity of the R-groups, which influences the stability and swelling behaviour of the MCsomes. Variations in removing the THF solvent from the MCsomes can vary the interstitial water. This study highlights that water can act as an assembling component besides being just a solvent.

Kristijan Lulic
Chemistry
Waterloo

Self Association of Oligoquinoline Foldamers
Probed by Fluorescence Anisotropy

Self-Association of Oligoquinoline Foldamers Probed by Fluorescence Anisotropy

Kristijan Lulic, Jingqi Wang, Victor Maurizot,* Ivan Huc,* Jean Duhamel*

Institute for Polymer Research, Waterloo Institute for Nanotechnology, Department of Chemistry, University of Waterloo, ON N2L 3G1, Canada

INTRODUCTION

Foldamers are a class of synthetic oligomers, that fold into specific conformations in solution by way of intramolecular non-covalent interactions.¹ On the other hand, intermolecular non-covalent interactions are often involved in the self-assembly of macromolecules. In particular, self-assembly enables the production of complex architectures by spontaneous association under equilibrium conditions.² This process is the guiding principle for many biological processes and has been applied to various areas of chemistry and material sciences.³ The forces at play in a typical self-assembling system are both weak and reversible, such as hydrogen-bonding or hydrophobic and aromatic interactions.⁴ If applied to oligomeric foldamers, the self-assembly of foldamers could generate structures, that go beyond the realm of conventional synthetic strategies and find potential applications in molecular electronics or medicine.⁵ In this context, it would be interesting to investigate whether oligoquinoline foldamers could be designed to self-assemble into interesting structures, since they form rigid helices on their own in solution, stabilized by intramolecular hydrogen bonding and aromatic stacking.⁶ Characterization of these foldamers in solution has been the focus of a concerted research effort due to their potential use in different fields such as molecular wires due to their helical conformation combined with an electron rich backbone.⁷

Many analytical techniques have been applied to characterize oligoquinoline foldamers in solution.⁵ These include nuclear magnetic resonance spectroscopy (NMR), UV-Visible absorption spectroscopy, and time-resolved fluorescence anisotropy (TRFA). Since the latter method has already been employed to probe the helical conformation of oligoquinoline foldamers in solution, it was selected as a characterization technique due to its exceptional sensitivity, which enables its utilization at concentrations of macromolecule, which are orders of magnitude lower than those used for most other characterization techniques.⁸

In a typical TRFA experiment, a fluorophore is rigidly attached to a macromolecule and is irradiated with vertically polarized light. The tumbling of the fluorophore in solution reflects the tumbling of the macromolecule and by measuring the intensities of the vertically and horizontally polarized emissions, the fluorescence anisotropy can be determined.⁹ As time elapses, the vertically and horizontally polarized fluorescence intensities, which are initially different, merge to a same value and the anisotropy reaches zero. A measure of the time taken by the anisotropy to reach zero is related to the rotational time (ϕ) of the macromolecule. As seen in Equation 1, ϕ is a function of solvent viscosity (η), and more importantly, the hydrodynamic volume (V_h) of the macromolecule. Equation 1 allows the application of TRFA to measure the size of a macromolecular object in solution from its ϕ .

$$\phi = \eta V_h / RT \quad (1)$$

The linear relationship between ϕ and V_h implied by Equation 1 was taken advantage of to establish a calibration curve from the straight line obtained by plotting the ϕ of a series of oligoquinoline foldamers capped at one end with a methyl ester and at the other end with an oligo(phenylene vinylene) (OPV) dye as a function of the number of quinoline units (NU s) constituting the foldamer.¹⁰ The ϕ -vs- NU straight line could then be applied to predict the size of a series of four oligoquinoline foldamers, where the terminal ester had been hydrolysed to yield a carboxylic acid function. These hydrolysed foldamers could self-assemble in apolar chloroform after deprotonation of the acid with the addition of a drop of 16 M NaOH_(aq). A similar self-assembly was observed when mixing an OPV-labeled foldamer with an excess of unlabeled foldamer, where the acid of both foldamers had been deprotonated.

TRFA was applied to determine the ϕ of the self-assembled foldamers, which was found to increase with increasing foldamer concentration until it reached a plateau for foldamer concentrations above 1 mM. The ϕ -vs- NU calibration curve was applied to determine the size of the self-assembled foldamers, which led to the conclusion that the foldamer solutions were constituted of unassociated foldamers and dimers, with the dimer concentration increasing with increasing foldamer concentration. In turn, these trends could be analyzed to extract the equilibrium constant for the dimerization of these foldamers. This study provides further support for the use of TRFA as an important technique in the characterization of foldamers and their self-assemblies.

EXPERIMENTAL

All foldamers used were provided by the HUC Group at the University of Bordeaux. The nomenclature OPV-Q_nA was applied in this report for a foldamer constituted of n quinolines and labeled at one end with OPV and terminated at the other end with a carboxylic acid (A). To date, the self-assembly of three different OPV-labeled foldamers have been investigated under five different conditions across a concentration range spanning 6 orders of magnitude. These studies include the dimerization of OPV-Q₈A, OPV-Q₁₇A, and OPV-Q₃₃A, and the complexation of OPV-Q₈A with Q₁₆A. The concentrations of each species in solution was determined by UV-Visible absorption spectroscopy, using a molar extinction coefficient of 32,400 M⁻¹cm⁻¹ at 450 nm for OPV and 5,600 M⁻¹cm⁻¹ at 326 nm per quinoline unit. To induce dimerization, approximately 1.0 g of chloroform solution of an OPV- labeled foldamer was placed in a 4 mL scintillation vial to which a drop of 16 M NaOH_(aq) was added. The solutions were vortexed for two minutes and left unperturbed until the organic layer was no longer turbid. For concentrations greater than 80 μ M, front face geometry was applied with a 1 mm absorption cell to minimize reabsorption and inner filter effects, that would otherwise skew the analysis of the fluorescence decays. For concentrations below this threshold, the right-angle geometry was used for the decay acquisition. In these experiments, polarized decays were obtained using vertically polarized excitation light at a wavelength of 479 nm and subsequently polarized emissions were collected at 510 nm at angles parallel and perpendicular to the orientation of the polarized excitation light as well as at the magic angle (54.7°), where polarization effects are eliminated. Analysis of the decays involved first fitting the fluorescence decays acquired at the magic angle with a monoexponential function shown in Equation 2 to determine the lifetime (τ_0) of OPV-bound to the foldamer.

$$I_{VM}(t) = I_0 e^{\left(\frac{-t}{\tau_0}\right)} \quad (2)$$

In Equation 2, I_o is the initial fluorescence intensity and t is the time in nanoseconds. The vertically and horizontally polarized decays were then fit globally according to Equations 3 and 4, respectively.

$$I_{VV}(t) = \frac{I_{VM}(t)}{3} (1 + 2r(t)) \quad (3)$$

$$I_{VH}(t) = \frac{I_{VM}(t)}{3G} (1 - r(t)) \quad (4)$$

In Equations 2 and 3, the G-factor is a scaling factor that is optimized during the analysis and $r(t)$ is the time-dependent anisotropy. The anisotropy $r(t)$ is well represented by a sum of exponentials as shown in Equation 5.

$$r(t) = r_o \sum_{i=1}^n a_i e^{\left(\frac{-t}{\phi_i}\right)} \quad (5)$$

In Equation 5, r_o is the intrinsic anisotropy or the anisotropy at time equal to zero. The pre-exponential factors a_i correspond to the i^{th} rotational time ϕ_i . For the relatively short foldamers investigated so far, $r(t)$ only needed one rotational time ($n = 1$ in Equation 5). Global analysis of the polarized decays $I_{VV}(t)$ and $I_{VH}(t)$ yielded the rotational time of the macromolecules, which could be related to their hydrodynamic volume.

RESULTS AND DISCUSSION

Four foldamer species have been studied by time-resolved fluorescence anisotropy (TRFA). Measurements were performed in chloroform without or with the addition of a drop of 16 M NaOH_(aq) solution. The trends obtained with ϕ determined by TRFA are shown in Figure 1. As the foldamer concentration increased, ϕ remained constant when in chloroform without NaOH. However, upon addition of base, ϕ increased with increasing foldamer concentration until it reached a plateau. The increase in ϕ reflects the association of the OPV-Q_nA foldamers into larger objects, when NaOH was added to the chloroform solution. The plateau indicates that this association proceeds according to a closed mechanism that led to a thermodynamically stable species.

Accounting for the chemical structure of the deprotonated OPV-Q_nA foldamers with a carboxylate anion at one end, the foldamers might be able to dimerize by forming contact ion pairs between their ends. As for the dimerization of ion pairs generated between the propagating ends of growing chains in anionic polymerization, dimerization of the foldamers would minimize exposure of the carboxylate anions to the apolar chloroform, while the foldamers would stabilize the ion pairs. Dimerization of foldamers would also agree with the notion of a closed association mechanism suggested by the ϕ -vs-[foldamer] plots shown in Figure 1.

Confirmation, that dimerization took place, was obtained by plotting the ϕ obtained in the plateau region [$\phi(\infty)$] at high foldamer concentration as a function of NU and $2 \times NU$ in Figure 2. $\phi(\infty)$ increased linearly with increasing NU in Figure 2 indicating that the size of the complexes formed in the chloroform solution with NaOH was strongly related to the size of the foldamer. Furthermore, the fact, that $\phi(\infty)$ increased linearly with $2 \times NU$ with the same slope as that found for the straight line obtained by plotting ϕ as a function of NU for the unassociated foldamers in

chloroform, was taken as strong evidence that the complexes were in fact dimers. It was noticeable that the $\phi(\infty)$ -vs- $2 \times NU$ trend obtained for the dimerized foldamers was slightly offset by a constant value with respect to the ϕ -vs- NU trend obtained for the unassociated foldamers in chloroform without NaOH. This offset was attributed to the two OPV moieties, that were part of the foldamer dimers, and thus added a constant volume to the V_h probed by ϕ . In contrast, the unassociated foldamers, which contained only one OPV moiety, resulted in a smaller V_h compared to the dimerized foldamers.

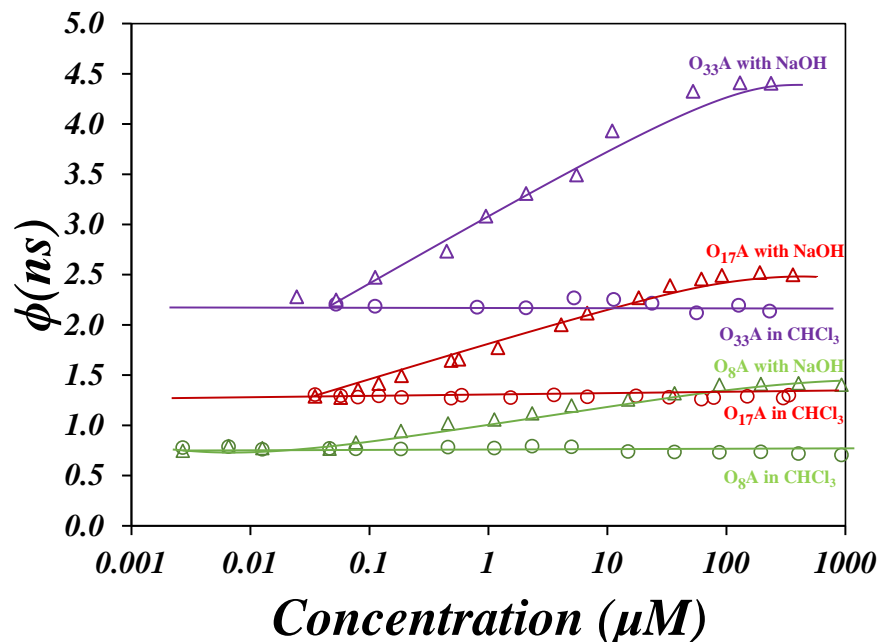


Figure 1. Plots of the rotational time as a function of foldamer concentration (green) OPV-Q₈A, (red) OPV-Q₁₇A, and (purple) OPV-Q₃₃A with (triangles) and without (circles) NaOH.

The trends shown in Figure 1 were analyzed to extract the equilibrium constant (K) for the dimerization of OPV-Q_nA foldamers by applying the law of conservation of mass to derive Equation 6, which yielded a mathematical expression for the average rotational time ($\langle \phi \rangle$) obtained by TRFA measurements. In Equation 6, ϕ_1 and ϕ_2 represent the rotational times of the unimers and the dimers and were determined experimentally from the ϕ of the unassociated foldamers in chloroform without NaOH and $\phi(\infty)$ obtained for the foldamers in chloroform with NaOH at high foldamer concentration, respectively. The concentrations of unassociated and dimerized foldamers were referred to as $[A]$ and $[A_2]$, respectively.

$$\langle \phi \rangle_{cal} = \frac{[A] \times \phi_1 + 2 \times [A_2] \times \phi_2}{[A]_o} \quad (6)$$

Since the concentrations $[A]$ and $[A_2]$ could be expressed as a function of the known concentration of foldamer in the solution and the equilibrium constant (K), $[A]$ and $[A_2]$ were calculated at each foldamer concentration studied for different K values and they were used to determine a theoretical $\langle \phi \rangle$ value according to Equation 6. Comparison of the experimental and

theoretical $\langle\phi\rangle$ values led to a routine to search for the optimal K value, that would minimize the χ^2 . A representative plot of χ^2 versus K is shown in Figure 3A. The K value at the χ^2 minimum was taken as the equilibrium constant for dimerization, and it was used to calculate the molar fractions of unassociated (f_A) and dimerized (f_{A2}) foldamers as well as the predicted $\langle\phi\rangle$, which were compared to the experimental values in Figures 3B and C, respectively.

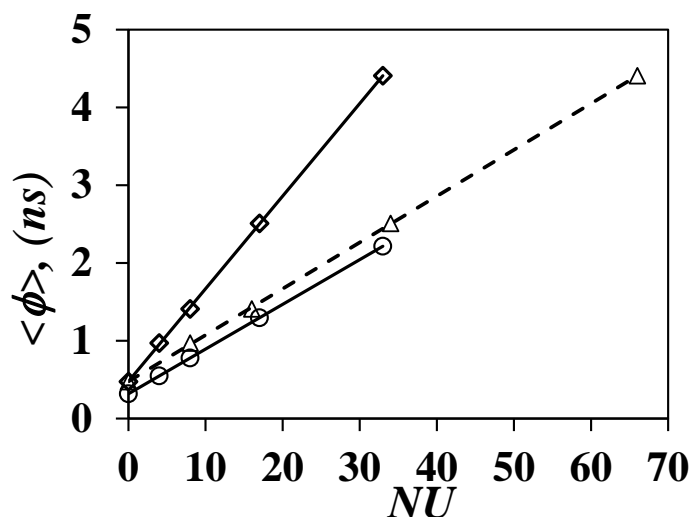


Figure 2. Plots of ϕ as a function of the number of quinolines for (○) the unassociated foldamer acids obtained in chloroform without NaOH, (◇) $\phi(\infty)$ for the foldamer acids in chloroform with NaOH as a function of NU , and (△) $\phi(\infty)$ for the foldamer acids in chloroform with NaOH as a function of $2 \times NU$.

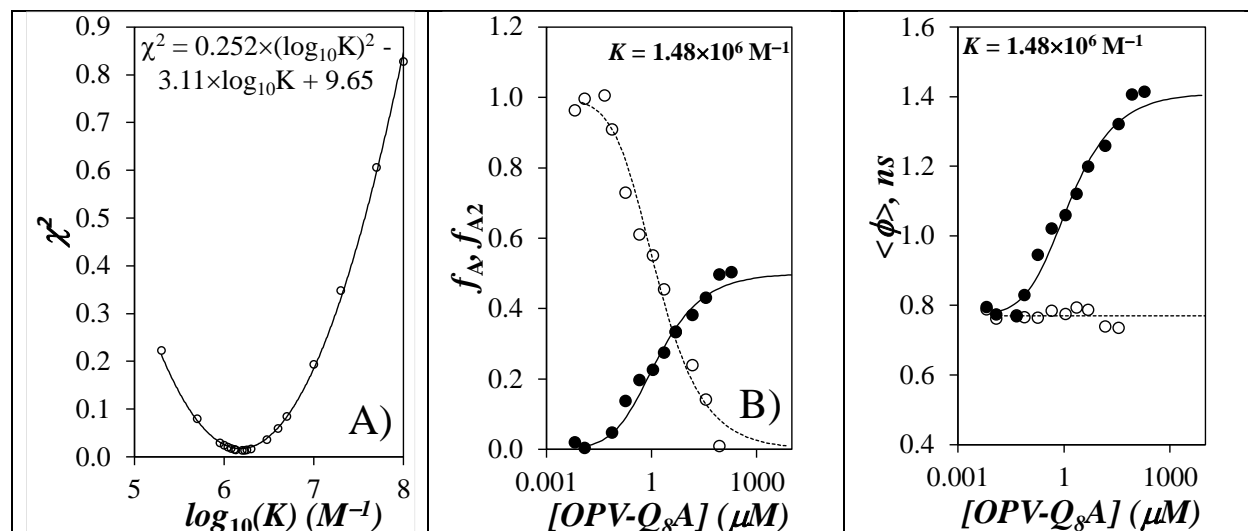


Figure 2. Plot of χ^2 as a function of $\log_{10}(K)$ fitted with a second order polynomial yielding a K -value of $1.48 \times 10^6 \text{ M}^{-1}$ at the minimum. B) the molar fractions of (○) unimer and (●) dimer and C) the average rotational time as a function of OPV- Q_8A concentration. Solutions (●) with and (○) without one drop of 16 M NaOH aqueous solution.

These optimizations were conducted for all the traces shown in Figure 1 and for the equilibrium of OPV-Q₈A and Q₁₆A, yielding Figure 4, where K was plotted as a function of the NU expected from the complex formed by the different foldamer mixtures. The equilibrium constant remained constant with NU taking an average value of $1.21 \times 10^6 \pm 1.51 \times 10^5 \text{ M}^{-1}$. The constant K value obtained for the different foldamers indicates that it does not change with foldamer length. Furthermore, equilibrium constants of this magnitude reflect a strong association, which is conducive of self-assembly as illustrated in Figure 1, and show that these foldamers are in an equilibrium driven by concentration, regardless of their size.

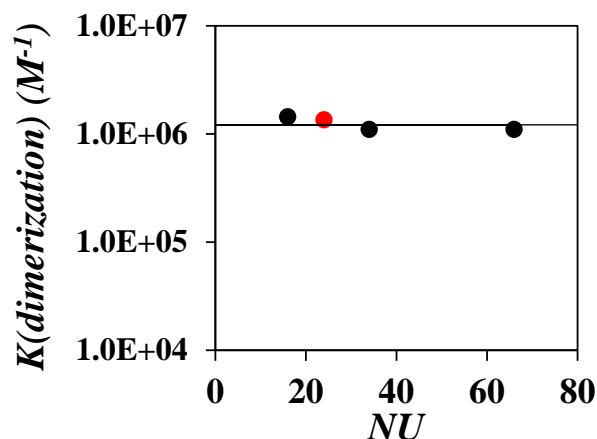


Figure 4. Plot of K as a function of the expected NU for the complex generated in the different foldamer mixtures for (black) the dimers and (red) the OPV-Q₈A and Q₁₆A complex.

CONCLUSIONS

This study has demonstrated that TRFA represents a robust experimental tool to characterize the size of unassociated and complexed foldamers. In particular, it led to the conclusion that the deprotonated OPV-Q_nA foldamers dimerized in chloroform with NaOH. In all cases, the data could be analyzed to yield the equilibrium constant for complexation. The K values were large enough to promote foldamer self-assembly as illustrated in Figure 1.

REFERENCES

- (1)Gellman, S. H. Foldamers: A Manifesto. *Acc. Chem. res.* **1998**, *31*, 173-180.(2)Whitesides, G. M.; Boncheva, M. Beyond Molecules: Self-Assembly of Mesoscopic and Macroscopic Components. *Proc. Natl. Acad. Sci. U S A.* **2002**, *99*, 4769-4774.
- (3)Douglas, P.; Stoddart, J. F. Self-Assembly in Natural and Unnatural Systems. *Angew. Chem. Int. Ed. Engl.* **1996**, *35*, 1154-1196.(4)Lehn, J. Toward Self-Organization and Complex Matter. *Science* **2002**, *295*, 2400-2403.(5) Wang, J. Characterization of Self-Assembling Quinoline-Based Foldamers by Fluorescence Anisotropy. M. Sc. Thesis at the University of Waterloo, 2019.(6)Jiang, H.; Léger, J.-M.; Huc, I. Aromatic δ -Peptides. *J. Am. Chem. Soc.* **2003**, *125*, 3448-3449.(7) Li, X.; Qi, T.; Srinivas, K.; Massip, S.; Maurizot, V.; Huc, I. Synthesis and Multibromination of Nanosized Helical Aromatic Amide Foldamers via Segment-Doubling Condensation. *Org. Lett.* **2016**, *18*, 1044-1047.(8) Chuang, T. J.; Eisenthal, K. B. Theory of Fluorescence Depolarization by Anisotropic Rotational Diffusion. *J. Chem. Phys.* **1972**, *57*, 5094-5097.(9) Lakowicz, J. R. Principles of Fluorescence Spectroscopy 2nd Ed., Kluwer Acad. New York, 1999.(10) Wang, J.; Little, H.; Duhamel, J.; Li, X.; Markandeya, N.; Maurizot, V.; Huc, I. Application of Time-Resolved Fluorescence Anisotropy to Probe Quinoline-Based Foldamers Labeled with Oligo(phenylene vinylene). *Macromolecules* **2019**, *52*, 5829-5837.(11) Engel, J. Thermodynamics and Kinetics of Self-Assembly. In *Biophysics*; Eds. Hoppe, W.; Lohmann, W.; Markl, H.; Ziegler, H. Springer-Verlag: Berlin, Heidelberg, New York, Tokyo **1983**, Chapter 11, pp 408-412.

Damin Kim
Chemistry
Waterloo

Compressibility of Amylopectin Characterized
by Pyrene Excimer Formation

Winner of the 2021 IPR Award for Academic
Excellence in Polymer Science/Engineering

Compressibility of Amylopectin Characterized by Pyrene Excimer Formation

Damin Kim and Jean Duhamel

IPR Symposium, University of Waterloo, Waterloo, ON, N2L 3G1, Canada

INTRODUCTION

Amylopectin is a polysaccharide that is found in various botanical sources, such as in corn and potato. The structure of amylopectin has been studied widely using a variety of techniques such as enzymatic treatment, acid hydrolysis, etc. These studies have revealed that amylopectin is a highly branched polysaccharide, where linear segments composed of glucose units linked by α -(1,4) glycosidic bonds are joined to each other by α -(1,6) glycosidic bonds. Incomplete acid hydrolysis of amylopectin indicated that amylopectin is composed of both amorphous and crystalline domains.¹ It was later demonstrated by SAXS that in the solid state, the linear segments of amylopectin are arranged in clusters. They adopt a helical conformation and form crystalline lamellae, that are connected to each other by longer oligosaccharide chains, which are found in the amorphous domains. X-ray diffraction experiments on starch granules showed that the crystalline domains have a density of 1.5 g/mL with the helices spread approximately 1.1 nm apart.²

The solution cluster model (SCM) was proposed in 2020 to predict the internal structure of amylopectin in solution.³ The model is based on the cluster model for amylopectin and assumes that the helices generated by a cluster of short oligosaccharides are hexagonally packed. The SCM predicts that the interhelical distance (d_{h-h}) between the side chains of amylopectin in DMSO equals 2.9 nm, resulting in a density of 0.28 ± 0.01 g/mL. Since the diameter of a single helix with 7 anhydroglucose units per turn equals 1.5 nm,⁴ d_{h-h} values much shorter than 2.9 nm could be obtained if the side chains of amylopectin could be induced to come even closer in DMSO. To investigate how close the short helical oligosaccharide side chains of amylopectin could be brought to each other in DMSO, the compressibility of amylopectin and three different research-grade nanosized amylopectin fragments (NAFs) obtained from EcoSynthetix was examined.

To this end, amylopectin and the NAFs were labeled with 1-pyrenebutyric acid to take advantage of the ability of an excited pyrenyl label to form an excimer upon encounter with a ground-state pyrenyl. Since pyrene excimer formation (PEF) depends on the local concentration ($[Py]_{loc}$) of pyrenyl labels covalently attached to the macromolecule, PEF reflects the internal density of the macromolecule, an effect that could be employed to assess by how much amylopectin and NAFs could be compressed in DMSO. The PEF efficiency could be gauged from the fluorescence intensity ratio of the excimer (I_E) over that of the monomer (I_M), namely the I_E/I_M ratio, which depends on the local pyrene concentration ($[Py]_{loc}$). More quantitative information about $[Py]_{loc}$ could be obtained by analyzing the monomer and excimer fluorescence decays of the pyrene-labeled polysaccharides in DMSO according to the Fluorescence Blob Model (FBM). The FBM yields the number (N_{blob}) of structural units present in a *blob*, which represents the volume probed by a pyrenyl label, while it remains excited. A denser macromolecule yields a larger N_{blob} as more structural units can be found inside a *blob*. Unlabeled starch was added to the solutions of pyrene-labeled amylopectin or NAFs in DMSO as a means to increase the osmotic pressure, which triggered the compression of the pyrene-labeled polysaccharides and increased $[Py]_{loc}$. Changes in $[Py]_{loc}$ were monitored by following how I_E/I_M and N_{blob} changed as a function of starch concentration.

I_E/I_M and N_{blob} were found to increase with increasing starch concentration reflecting the compression of amylopectin at concentrations above its overlap concentration (C^*). This compression resulted in an increase in the local concentration of pyrene due to a decrease in d_{h-h} .

Smaller polysaccharides showed a weaker increase in PEF compared to larger ones, an effect which might be attributed to the number of helices involved in PEF. Consequently, the relationship presented earlier between N_{blob} and $d_{\text{h-h}}$, that assumed that infinite clusters of helices were present in amylopectin, might not be true for smaller polysaccharides like the NAFs. The relationship between N_{blob} and $d_{\text{h-h}}$ was re-examined by taking into account the number of helices, that might be involved in PEF in a given pyrene-labeled polysaccharide. The revised relationship was then used to predict the number of helices, that participate in PEF for each polysaccharide.

EXPERIMENTAL

Materials: NAFs were obtained from EcoSynthetix, purified by dialysis against water, and lyophilized prior to use. Amylopectin and all other chemicals were purchased from Sigma Aldrich. Amylopectin was purified by dissolving it in DMSO and precipitating it in acetone.

Size of Amylopectin and NAFs: The number-average hydrodynamic diameter (D_h) of NAFs was determined by Dynamic Light Scattering (DLS) using 0.1 wt% NAF dispersions in DMSO at 25 °C. For example, a NAF with a D_h of 56 nm was represented as NAF(56). Amylopectin(220), NAF(8), NAF(17), and NAF(56) were used in this study. The intrinsic viscosity of amylopectin was determined with an Ubbelohde viscometer and used to determine the diameter of amylopectin, found to equal 200 nm, by applying the equation relating intrinsic viscosity and the diameter of amylopectin, which had been established earlier.^{Error! Bookmark not defined.}

Preparation of Pyrene Labeled Amylopectin (Py-Amylopectin) and NAFs (Py-NAFs): The synthesis, purification, and determination of the pyrene content of the pyrene-labeled polysaccharides followed a procedure that was developed for amylose and which has been described earlier.^{Error! Bookmark not defined.} Py(x)-Amylopectin or Py(x)-NAF describe a polysaccharide where a molar percentage x of the anhydroglucose units were labeled with 1-pyrenebutyric acid.

Preparation of Mixtures of Py-Amylopectin or Py-NAF and Unlabeled NAF(56): Dispersions of naked NAF(56) with a concentration smaller than 30 wt% were prepared by adding the required amount of unlabelled NAF(56) (0-30 wt %) to a dispersion of pyrene-labeled polysaccharide (PyLP) in DMSO with a pyrene concentration equal to 24 μM . The dispersions were stirred for two days at room temperature to obtain a homogeneous dispersion. For dispersions with a NAF(56) content greater than 30 wt%, the proper mass of NAF(56) was added to a dilute PyLP dispersion in DMSO. The DMSO was then evaporated so that the final dispersion would contain about 24 μM pyrene from the Py-NAF sample and a large excess of NAF(56) sample that would result in the desired starch concentration (> 30 wt%). In each case, the PyLP dispersion was sufficiently dilute to prevent intermolecular PEF. The dispersions were analyzed by steady-state (SSF) and time-resolved (TRF) fluorescence without degassing.

RESULTS AND DISCUSSION

Amylopectin and NAFs with a pyrene content of $\sim 6 (\pm 1)$ mol% were examined to monitor the change in I_E/I_M and N_{blob} as a function of [NAF(56)]. The formation of excimer was enhanced with increasing [NAF(56)]. I_E/I_M and N_{blob} began to increase at 10.2 ± 0.8 wt% and at 11.5 ± 1.7 wt% for Py-amylopectin and Py-NAFs, respectively, while the formation of excimer remained mainly unchanged for amylose. The increase in the I_E/I_M ratio observed in Figure 1 is due to an increase in $[Py]_{\text{loc}}$ induced by the compression of the PyLPs as interpenetration of these highly branched polysaccharides is not possible. In the case of amylose, which is fully exposed to the solvent and

where compression does not take a place, $[Py]_{loc}$ is unaffected and I_E/I_M remains constant within experimental error.

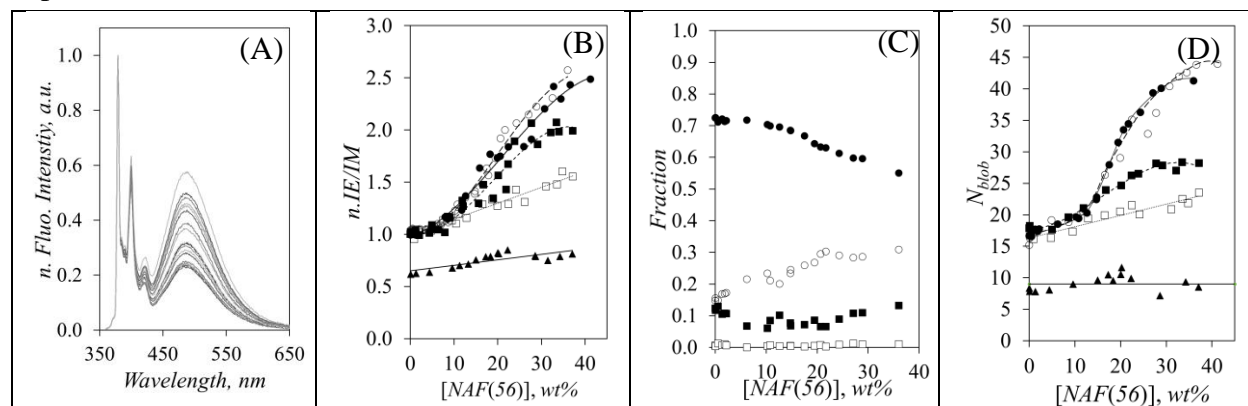


Figure 1. A) Fluorescence spectra of Py(6.7)-NAF(56) acquired with increasing [NAF(56)]. B) Plot of the normalized I_E/I_M ratios. C) Plot of the molar fractions for the pyrene species in Py(6.7)-NAF(56) Py_{diff} (●), Py_{k2} (○), Py_{agg} (■) and Py_{free} (□) as a function of NAF(56) concentration. D) Plot of N_{blob} a function of [NAF(56)]. Symbols in Figures 1B and D: (○) Py(4.2)-Amylopectin, (●) Py(6.7)-NAF(56), (■) Py(5.8)-NAF(16), (□) Py(5.8)-NAF(8), and (▲) Py(5.5)-amylose (▲).

Numerous studies of PEF in pyrene-labeled macromolecules have identified four pyrene species, that are defined by the type of photophysical pathway, that they undergo during PEF. Py_{free}^* is the pyrene species that does not form excimer and emits with the natural lifetime of the pyrene monomer as if it was free in solution. Py_{diff}^* represents the pyrene species, that diffuses slowly in solution according to the mobility of the structural unit it is attached to, before two structural units, one bearing Py_{diff}^* and the other bearing a ground-state pyrene, encounter. At this point, Py_{diff}^* transforms into Py_{k2}^* , which undergoes a rapid re-arrangement with a rate constant k_2 to form an excimer. Py_{agg}^* represents the pyrene species being part of a pyrene aggregate and forms excimer instantaneously upon absorption of a photon. The population of each pyrene species contributing to PEF was determined through the FBM analysis of the fluorescence decays of the PyLPs and a representative plot of the molar fractions is shown in Figure 1C for Py(6.7)-NAF(56). The most visible change in the contribution of each pyrene species was observed for Py_{diff}^* and Py_{k2}^* . While the contributions from Py_{free}^* and Py_{agg}^* remained small and constant with [NAF(56)], less excimer formed by diffusion and more excimer formed through a rapid rearrangement of the pyrene species as the [NAF(56)] increased. The decrease in d_{h-h} following the compression of the PyLPs brought more excited pyrene molecules close to a ground-state pyrene, which generated more Py_{k2}^* species that formed excimer by a rapid rearrangement.

N_{blob} increased with increasing [NAF(56)] for all PyLPs in Figure 1D. The maximum N_{blob} value determined experimentally (N_{blob}^{exp}) was found to increase with increasing particle size and was determined to reach a maximum value of 43, 40, 28, and 24 for Amylopectin (220), NAF(56), NAF(16), and NAF(8), respectively. A relationship between N_{blob} and d_{h-h} was previously established by considering a cluster of 7 helices with the assumption that the 7 helices were representative of an infinite array of hexagonally packed helices. ^{Error! Bookmark not defined.} This relationship predicted that the theoretically determined N_{blob} (N_{blob}^{theo}) would increase with decreasing d_{h-h} . While this behavior could qualitatively rationalize the increase observed for the experimentally obtained N_{blob} (N_{blob}^{exp}) values in Figure 1C with increasing [NAF(56)], it could

not explain two features of the plots. First, the maximum $N_{\text{blob}}^{\text{theo}}$ obtained by assuming an infinite array of helices was 37, a value that was lower than the $N_{\text{blob}}^{\text{exp}}$ values of 41 (± 2) obtained for Amylopectin(220) and NAF(56) in Figure 1C at high [NAF(56)]. Second, the maximum value taken by $N_{\text{blob}}^{\text{exp}}$ in Figure 1C depended on the size of the particles, something that could not be accounted for by the earlier $N_{\text{blob}}^{\text{theo}}-v_s-d_{h-h}$ relationship. These discrepancies were attributed to the fact, that the earlier $N_{\text{blob}}^{\text{theo}}-v_s-d_{h-h}$ relationship was derived by assuming an infinite array of oligosaccharide helices separated by d_{h-h} . While this assumption might have been justified for large polysaccharides like Amylopectin(220) and NAF(56), smaller polysaccharides like NAF(8) and NAF(16) might not contain enough helices to generate an infinite array of helices. Furthermore, the derivation used one central helix surrounded by six others in the hexagonal array and separated by d_{h-h} . Since the onset distance for interactions between pyrenyl labels attached onto helices equals 3.2 nm, the assumption, that a central helix could interact with six helices located in a first ring (see Figure 2A), was correct for d_{h-h} values larger than 1.6 nm, but not for d_{h-h} values smaller than 1.6 nm, which could allow interactions between the pyrenyl labels of helices in a ring located $2 \times d_{h-h}$ away. Consequently, a second ring of helices in the hexagonal array located $2 \times d_{h-h}$ away from the central helix needed to be included in the calculation of $N_{\text{blob}}^{\text{theo}}$ as shown in Figure 2A to represent the regime of high [NAF(56)] in Figure 1C. The $N_{\text{blob}}^{\text{theo}}$ values were recalculated as a function of the number of helices in an hexagonal array and d_{h-h} and they are shown in Figure 2B. In Figure 2B, $N_{\text{blob}}^{\text{theo}}$ was found to increase with an increasing number of helices and decreasing d_{h-h} .

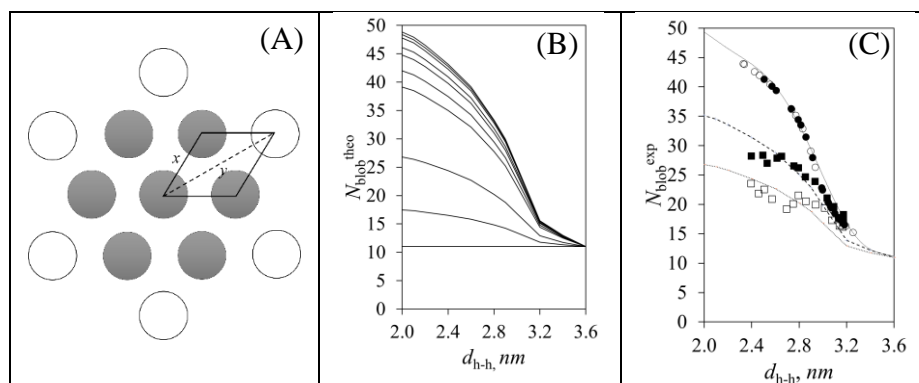


Figure 2. A) Illustration of an array of 7 hexagonally packed helices with additional helices located at 30° and 90° on a second ring with respect to the center helix. B) Plot of $N_{\text{blob}}^{\text{theo}}$ as a function of d_{h-h} where the number of helices in the array equal one, two, four, 19, 37, 91, 169, 547, 1027, and 2107 from the bottom to top. C) Plot of N_{blob} as a function of d_{h-h} as a function of [NAF(56)] for Py(4.2)-Amylopectin(220) (\circ), Py(6.7)-NAF(56) (\bullet), Py(5.8)-NAF(16) (\blacksquare), and Py(5.8)-NAF(8) (\square) where the solid (-), dash (--) and dotted (...) lines represent the $N_{\text{blob}}^{\text{theo}}$ for a number of helices equal to ∞ , 9, and 4, respectively.

The overlapping $N_{\text{blob}}^{\text{exp}}$ trends obtained for Py(4.2)-Amylopectin(220) and Py(6.7)-NAF(56) in Figure 1D suggest that these PyLPs are well-described by an infinite array of helices since $N_{\text{blob}}^{\text{exp}}$ at high [NAF(56)] in Figure 1D matches $N_{\text{blob}}^{\text{theo}}$ for low d_{h-h} in Figure 2B. Consequently, the $N_{\text{blob}}^{\text{exp}}$ values of Amylopectin(220) and NAF(56) were used to predict d_{h-h} at a given concentration of NAF(56) for all PyLPs, since all PyLPs were expected to be subject to the same osmotic pressure at a given [NAF(56)]. Since d_{h-h} was known in Figure 2B, $N_{\text{blob}}^{\text{exp}}$ of a given

PyLP could then be related to the number of helices required to generate a PEF signal at a given d_{h-h} based on the calibration curve shown in Figure 2B. Matching the trends obtained for $N_{\text{blob}}^{\text{exp}}$ in Figure 1D and $N_{\text{blob}}^{\text{theo}}$ in Figure 2B as a function of d_{h-h} resulted in the plots in Figure 2C, which suggested that PEF in Amylopectin(220) and NAF(56) involved a few hundreds of helices while PEF in NAF(16) and NAF(8) only involved 9 and 4 helices, respectively. Figure 3 is introduced to illustrate the effect discussed in Figures 1 and 2. In a same array of most likely disordered helices, the helices, that are involved in PEF, are separated by a distance d_{h-h} on average. The PEF response depends on the osmotic pressure as d_{h-h} decreases with increasing osmotic pressure. The array becomes smaller and contains more peripheral helices as the size of the NAFs decreases. Since the peripheral helices experience fewer interhelical interactions compared to the helices inside the array, the smaller NAFs yielded lower N_{blob} values. The effect of the peripheral helices resulted in lower maximum $N_{\text{blob}}^{\text{exp}}$ values for NAF(16) and NAF(8) compared to the maximum $N_{\text{blob}}^{\text{exp}}$ values of Amylopectin(220) and NAF(56) in Figure 1D.

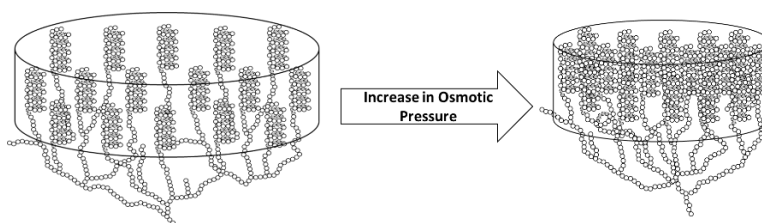


Figure 3. Illustration of a response of an array of (most likely) disordered helices probed by PEF as osmotic pressure is increased by the addition of unlabeled NAF(56).

CONCLUSIONS

The compressibility of amylopectin and three NAFs was studied by monitoring the I_E/I_M ratio and N_{blob} value as a function of NAF concentration. An increase in the NAF concentration above C^* built up the osmotic pressure applied to amylopectin and the NAFs, which resulted in the shrinkage of the PyLPs, as probed by an increase in the I_E/I_M ratio and N_{blob} . All the particles compressed at 11 wt% of NAF(56) regardless of the size of particles. At the same d_{h-h} , a particle with a larger size had a larger N_{blob} as it had more helices, that could generate more inter-helical interactions. The number of helices inside a PyLP involved in PEF was predicted to be within a few hundreds of helices for Amylopectin(220) and NAF(56) while our results suggested that PEF in NAF(16) and NAF(8) involved only 9 and 4 helices, respectively

REFERENCES

- ¹ French, D. Fine Structure of Starch and its Relationship to the Organization of Starch Granule. *J. Jpn. Soc. Starch Sci.* **1972**, *19*, 8-25.
- ² Imberty, A.; Tran, V.; Perez, S. Recent Advances in Knowledge of Starch Structure, *Starch/Stärke* **1991**, *43*, 375-384.
- ³ Li, L.; Kim, D.; Zhai, X.; Duhamel, J. A Pyrene Excimer Fluorescence (PEF) Study of the Interior of Amylopectin in Dilute Solution. *Macromolecules* **2020**, *53*, 6850-6860.
- ⁴ Yamashita, Y.; Hirai, N. J. Single Crystals of Amylose V Complexes. II. Crystals with 71 Helical Configuration. *Polym. Sci. Part A2* **1966**, *4*, 161-171.

Joanne Fernandez
Chemistry
Waterloo

Grafting of Starch using Cerium-Persulfate Initiation System

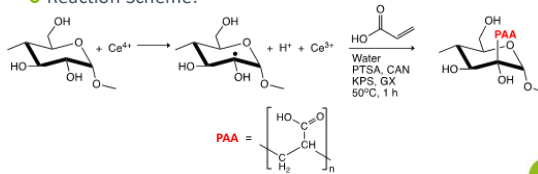
Grafting of Starch Using a Cerium-Persulfate Initiation System

Joanne Fernandez, Mario Gauthier
IPR Symposium 2021
May 5, 2021

EXPERIMENTAL PROCEDURES

- Synthesis of modified starch with cerium-persulfate initiation system
 - Grafting from technique
 - Speculative redox reaction with hydroxyl-containing polymers
 - Theoretically, homopolymerization is significantly reduced
 - Found that the addition of certain aldehydes (i.e. glyoxal and butyraldehyde) dramatically increased the grafting efficiency

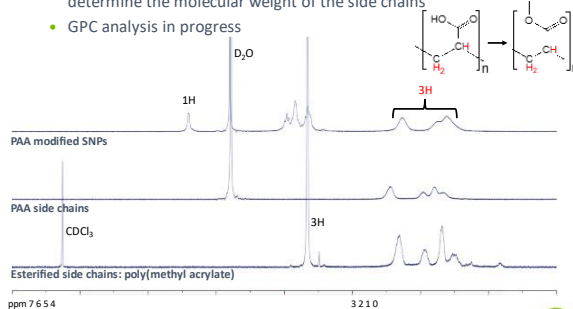
○ Reaction Scheme:



PTSA: *p*-Toluenesulfonic acid; CAN: Ceric ammonium nitrate; KPS: Potassium persulfate; GX: Glyoxal

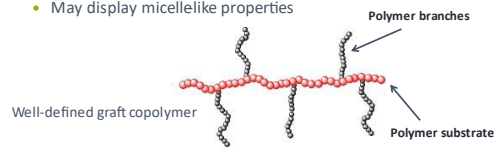
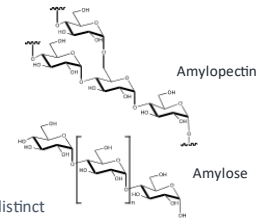
RESULTS

- Characterization of poly(acrylic acid) side chains
 - Successful degraded and esterified PAA modified starch to determine the molecular weight of the side chains
 - GPC analysis in progress



BACKGROUND

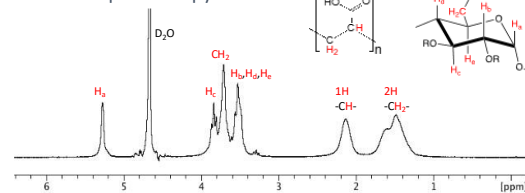
- Starch
 - Biocompatible, renewable and biodegradable
 - Composed of two main polymers: amylopectin and amylose
 - Various modification techniques
- Graft Copolymers
 - Can display characteristics of two distinct polymer phases
 - May display micellelike properties



A Rudin *The Elements of Polymer Science and Engineering* 2ed., Academic Press: Oxford, 1998.

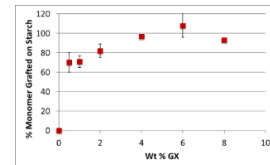
RESULTS

○ ¹H NMR Spectroscopy



○ Addition of Glyoxal

- % Monomer grafted on starch increases with the amount of glyoxal added



FUTURE WORK

- Investigate the grafting mechanism leading to increased efficiency in the presence of specific aldehydes
- Characterize the modified starch by additional techniques (dynamic light scattering, gel permeation chromatography, transmission electron microscopy)

Thank you!

Natun Dasgupta
Chemistry
Waterloo

Synthesis of Thermoresponsive Chitosan Films
grafted with Poly(di(ethylene glycol)methyl
ether methacrylate)

Synthesis of Thermoresponsive Chitosan Films Grafted with Poly(di(ethylene glycol) Methyl Ether Methacrylate)

May 5th 2021

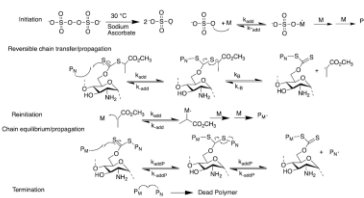
Presented by Natun Dasgupta

Supervisor: Prof. Mario Gauthier



Synthesis of Thermoresponsive Chitosan

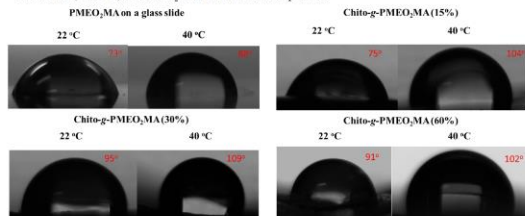
- To make thermoresponsive chitosan films, poly(di(ethylene glycol) methyl ether methacrylate) (PMEO₂MA) (LCST ~ 26 °C) can be grafted onto chitosan
- Reversible Addition Fragmentation Chain Transfer (RAFT) grafting was used to couple PMEO₂MA to the surface of chitosan films
- Cells could be grown on the thermoresponsive films at 37 °C, and then extracted by lowering the temperature below the LCST



PAGE 3

Contact Angle Measurements

- The surface of the modified chitosan samples was found to be more hydrophobic at temperatures above the LCST (~ 26 °C) of PMEO₂MA than at room temperature



PAGE 5

Conclusions

- PMEO₂MA was successfully grafted to deacetylated chitosan by RAFT at different compositions
- FTIR confirmed the presence of PMEO₂MA on the surface of chitosan
- The modified chitosan surfaces were thermoresponsive, as demonstrated through contact angle measurements

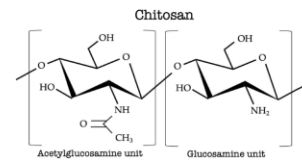
Future Work

- Cleave PMEO₂MA from the surface of chitosan and determine their chain length
- Conduct cell studies to grow cells on the surfaces at 37 °C, and then detach them by lowering the temperature below the LCST

PAGE 7

Introduction

- Chitosan is a linear polysaccharide made up of randomly distributed
 - β-(1→4)-linked D-glucosamine (deacetylated) units
 - β-(1→4)-linked N-acetyl-D-glucosamine (acetylated) units
- Chitosan is the second most abundant biopolymer, found mostly in the shells of crustaceans
- Currently used as an antibacterial agent and for drug delivery applications

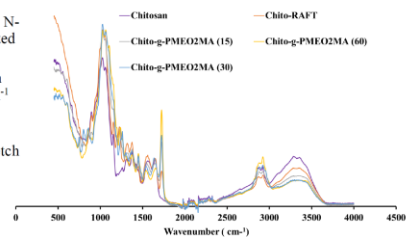


Juanito-Ocampo B, Valencia-Salazar S, Pinzón-Díaz CE, Herrera-Torres E, Aguilar-Pérez CF, Acuña J, Ku-Vera JC. The role of chitosan as a possible agent for enteric membrane navigation in remission. *Animals*. 2019; 9(11):942.

PAGE 2

IR Characterization

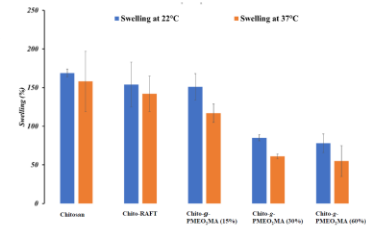
- Spectra normalized using the N-H bending peak of deacetylated chitosan at 1670 cm⁻¹
- The modified chitosan has an ester C=O stretch at 1730 cm⁻¹ in Chito-RAFT and Chito-g-PMEO₂MA
- The intensity of the C=O stretch increases as the amount of monomer used for grafting is increased



PAGE 4

Swelling Tests

- The modified and unmodified chitosan samples were soaked in water for 2 h at 22 and 37 °C
- The swelling capacity of the chitosan films decreases with the amount of PMEO₂MA grafted on its surface
- Since PMEO₂MA is hydrophobic above its LCST, swelling in modified chitosan samples decreases as the temperature rises



PAGE 6

Azin Adibi
Chemical Engineering
Waterloo

Engineered Polysaccharide α -1,3 glucan as
Reinforcement Fillers of Rubber
Nanocomposite Thin Films for Dipped Goods
Application

Engineered polysaccharide as reinforcement fillers of natural rubber nanocomposite

Presented by: Azin Adibi

Supervisors: Dr. Mekonnen and Dr. Simon



PAGE 1

Introduction

❖ Why engineered polysaccharide (commercially known as Nuvole™)?

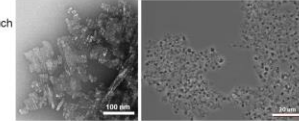
1. High modulus
2. High degree of crystallinity
3. High thermal stability
4. Excellent water dispersibility; opportunity for good interaction with rubber latex and other water based polymer systems

❖ Project objectives

- Improving the performance of latex based products such as gloves
- Providing sustainability options such as bio-content and/or biodegradability to address concerns on uncontrolled littering



Image of MCG



SEM image of MCG

Optical micrograph image of MCG

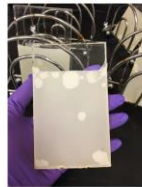


PAGE 2

Introduction

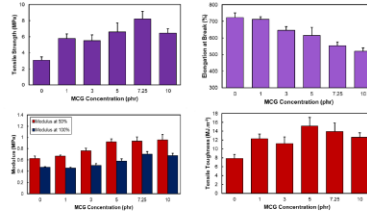
❖ Film preparation:

- Dipping method were employed for the film preparation.
- The formulation contained curing agent, activating agent, MCG and Natural rubber.
- Latex formulations with constant viscosity were prepared.
- Flat glass formers were used to prepare dipped films.
- The glasses were first dipped in a coagulant formulation, dried and then dipped into the rubber formulation followed by curing the samples for 2 hours



PAGE 3

Tensile test



- Incorporation of the MCG enhanced the tensile strength as well as modulus.

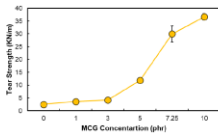
- As expected, elongation at break reduced with the addition of MCG.

- Generally the toughness of the films, increased with the addition of the MCG.



PAGE 4

Tear strength

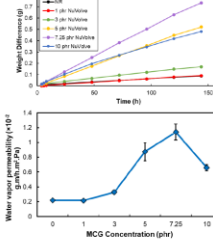


- Noticeable improvement in tear strength can be observed which can be due to good dispersion of MCG.
- These results can be promising tear properties for prolonging the practical life of gloves.



PAGE 5

Water vapor permeability



- Water vapor permeability (WVP) test conducted under constant relevant humidity environment as humidity has a positive correlation with water vapor permeability.

$$WVTR = \frac{G}{t \cdot A}$$

$$WVP = \frac{(WVTR) \times l}{\Delta p}$$

- The WVP increased with increasing concentration of the MCG.



PAGE 6




Thank you!
Any questions/comments?

PAGE 7


Mingrui Liang
Chemical Engineering
Waterloo

Tribological Studies of Cellulose Nanocrystal
Polyurethane Composite




Tribological studies of cellulose nanocrystal/polyurethane composite

Presenter: Mingrui Liang
Supervisor: Professor Boxin Zhao



Objective

- + To improve the tribological properties of waterborne polyurethane based coating, CNC/PU composites are fabricated by mixing CNC and PU with different ratios.
- + Tribological behaviors of CNC/PU composites will be investigated

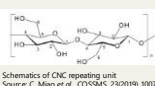


Photographic image of WPU/PMAN&D optical grating.

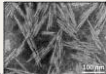
Background- two key components of this work

cellulose nanocrystal (CNC)

- + Most abundant renewable polymer resource
- + Typically, 6-10 nm in width and 100-200 nm in length
- + Highly polar, negatively-charged, hydrophilic nanoparticles



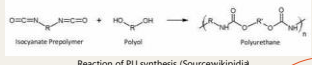
Schematics of CNC repeating unit
Source: C. Miao et al., COSSMS, 23(2019), 10076



TEM image of sulfonated CNC
Source: H. Ogunlu et al., COCS, 28, 46-56(20)

waterborne PU



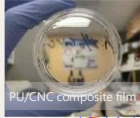
- + Superior mechanical properties with low volatile organic compound
- + High transparency, wear resistance, re-varnishing resistance



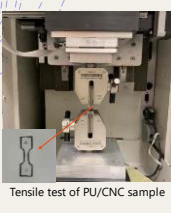
Reaction of PU synthesis (Source: wikipedia)

Fabrication of CNC/PU composite

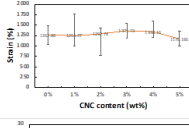
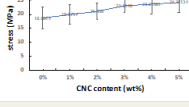
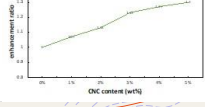
- + The powder CNC was dispersed in the DI water till no aggregation left with concentration of 10 mg/ml
- + The CNC dispersion was mixed with PU, sonication was employed to ensure the mixture uniform
- + The mixture was casted and evaporated in petri dish naturally

Current results

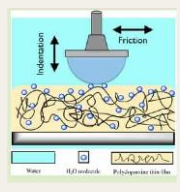


Tensile test of PU/CNC sample

CNC content (wt%)	Strain (%)	Stress (MPa)	Enhance ratio
0	1262.86	18.6644	1.00
1	1254.47	19.9757	1.07
2	1292.78	21.0380	1.13
3	1371.73	23.1046	1.23
4	1338.16	23.61581	1.26
5	1170.19	24.12124	1.31

Future work on tribological test



Scheme of indentation and friction test
(Source: W. Zhang et al., Biomacromolecules, 14, 394-405, 2013)

- Microindentation test are employed to investigate the adhesion contact
- Contact angle test will be carried out to analyze the film hydration
- Friction test of the PU/ CNC coating on different substrates both in air and water condition

Hunter Little
Chemistry
Waterloo

Probing the Internal Dynamics of Polymers in Polar Solvents

Probing the Internal Dynamics of Polymers in Solution from Pyrene Excimer Formation Experiments

Hunter Little and Jean Duhamel*

Institute for Polymer Research, Waterloo Institute for Nanotechnology, Department of Chemistry, University of Waterloo, ON, N2L 3G1, Canada

INTRODUCTION

The characterization of the flexibility of a macromolecule is most important to understand the underlying physical phenomena controlling the deformation of plastics¹ or the folding of proteins.² Too flexible, and a polypeptide loses its ability to adopt a stable structure; too rigid, and the polymer yields a brittle plastic, that cannot be deformed. For this reason, characterizing the flexibility of polymers is relevant to numerous fields of research.

One parameter often used to characterize the flexibility of a polymer is the glass transition temperature (T_g). T_g is defined as the temperature at which enough thermal energy has been absorbed by the polymer to allow interconversion between the *trans* and *gauche* conformations in the polymer backbone.^{1,3} Since rotation about backbone bonds is permitted above T_g , a more flexible and rubbery material is obtained for a polymer above T_g , while below T_g , the backbone is locked in place and the polymer is incapable of undergoing deformation.^{1,3,4} At first glance, these observations would make T_g a reasonable parameter to gauge the flexibility of a polymer. However, closer inspection reveals some glaring inconsistencies. Foremost is that T_g depends solely on the free volume generated by the polymer in the bulk. Consequently, the long side-chains of a polymer will generate substantial free volume, thus lowering T_g , even as they hinder backbone flexibility.⁴ Rogers and Mandelkern illustrated this effect by measuring the T_g of several poly(*n*-alkyl methacrylate)s (PAMAs).⁴ Increasing the side chain length of the PAMAs decreased both the mobility of the polymethacrylate backbone and T_g .⁴ The decrease in T_g was attributed to the generation of more free volume with increasing side chain length.^{Error! Bookmark not defined.} This, in addition to other shortcomings, means that a new parameter is needed to better describe the internal dynamics of a polymer.

While numerous techniques can measure the rotation diffusion coefficient of a macromolecule to probe its internal dynamics, fluorescence dynamic quenching is one of a very few techniques that can measure the translational diffusion coefficient of a polymer chain.⁵ Fluorescence quenching can occur with a polymer labeled with dyes and quenchers only if the quenchers can encounter the dye while it is excited and this encounter is controlled by the flexibility of the polymer backbone.⁵ By using the fluorophore pyrene, which can self-quench through the formation of an excited-state dimer, or excimer, the synthetic challenge of labeling the polymer with a dye and quencher is significantly reduced since it only involves the labeling with a single dye.⁶ Global analysis of the time-resolved fluorescence decays of the pyrene monomer and excimer using the fluorescence blob model (FBM) yields the parameters $\langle N_{\text{blob}} \rangle$ and $\langle k_{\text{blob}} \times N_{\text{blob}} \rangle$, which represent the number of structural units encompassed inside the volume probed by an excited pyrene and a measure of polymer chain dynamics, respectively.⁷ Global analysis of the fluorescence decays with the model-free analysis (MFA) yields $\langle k_{\text{MF}} \rangle^{\text{blob}}$,^{8,9} a parameter analogous to $\langle k_{\text{blob}} \times N_{\text{blob}} \rangle$. These parameters can be used to quantify the backbone flexibility of a polymer.

The relationship that exists between the product $\langle k_{\text{blob}} \times N_{\text{blob}} \rangle$ and the internal dynamics of a polymer is illustrated in Figure 1, where the product $\langle k_{\text{blob}} \times N_{\text{blob}} \rangle$ was plotted as a function of the molar mass of a structural unit (MW_{RU}) for a series of poly(alkyl methacrylate)s (PAMAs). PAMAs with a longer alkyl side chain and a larger MW_{RU} have a stiffer main chain and a smaller $\langle k_{\text{blob}} \times N_{\text{blob}} \rangle$ value. In turn, the trend shown in Figure 1 can be used as a benchmark against which the internal dynamics of other polymers can be compared.¹⁰⁻¹²

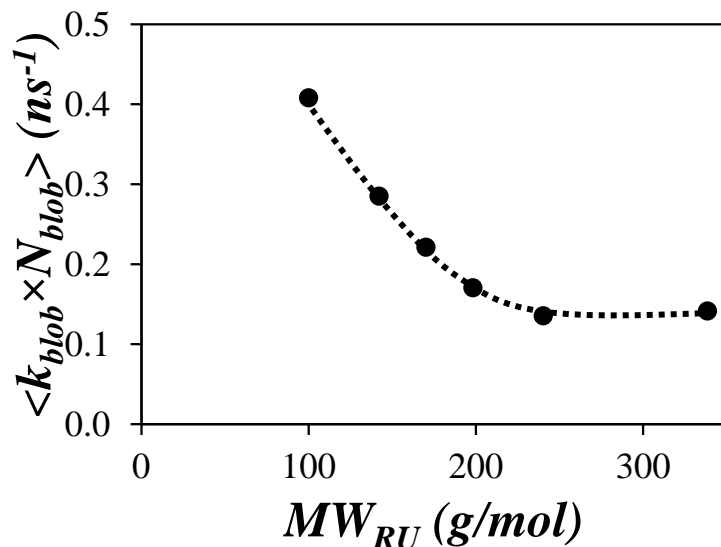


Figure 1. Plot of $\langle k_{\text{blob}} \times N_{\text{blob}} \rangle$ as a function of the molar mass of a structural unit (MW_{RU}) for poly(n -alkyl methacrylate)s in THF with alkyl side chains with 1 to 18 carbon atoms.

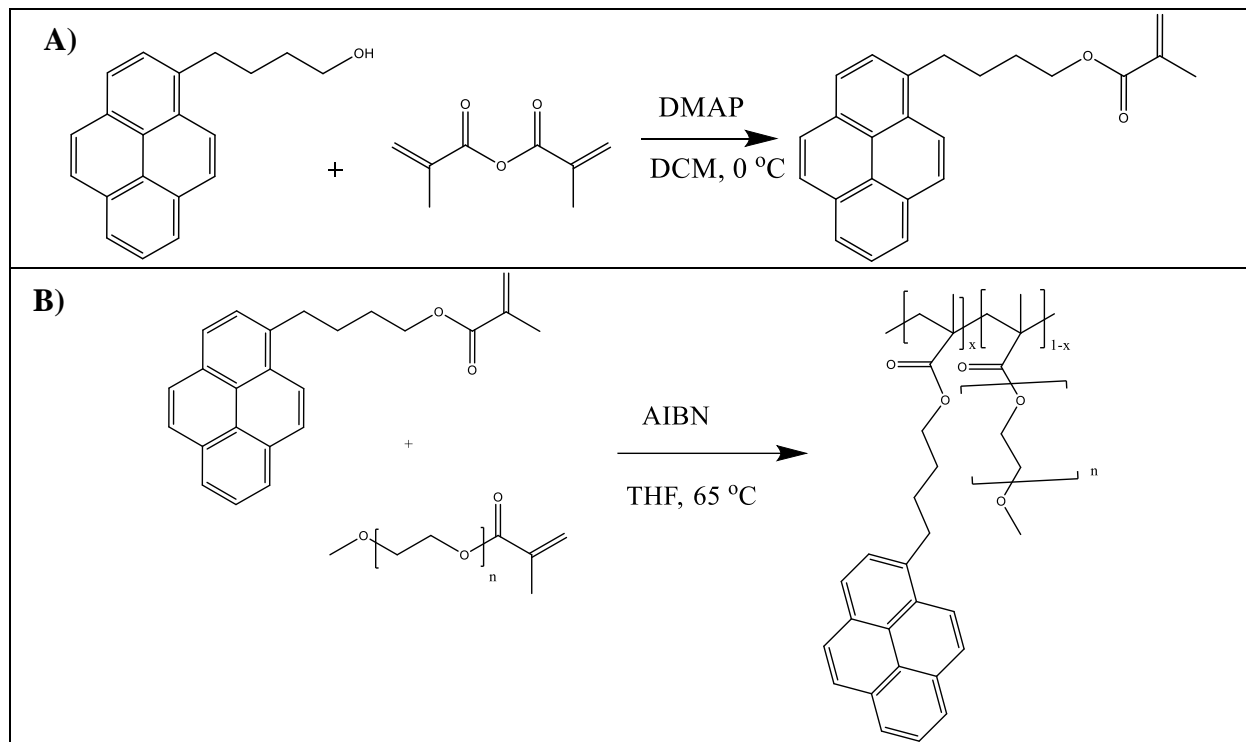
For a same MW_{RU} , a polymer with a value of $\langle N_{\text{blob}} \rangle$, $\langle k_{\text{blob}} \times N_{\text{blob}} \rangle$, or $\langle k_{\text{MF}} \rangle^{\text{blob}}$ greater than that of the PAMA benchmark, such as poly(dimethylsiloxane),¹² is more flexible than a polymer such as poly(isobutylene-*alt*-maleic anhydride)¹¹ with a value of $\langle N_{\text{blob}} \rangle$, $\langle k_{\text{blob}} \times N_{\text{blob}} \rangle$, or $\langle k_{\text{MF}} \rangle^{\text{blob}}$ below that of the PAMA benchmark. While this benchmark is most useful to assess the flexibility of other polymers with respect to PAMAs, it can only be used for polymers that are soluble in THF as the alkyl side chains limit the PAMAs solubility in more polar solvents such as dimethylformamide (DMF), dimethyl sulfoxide (DMSO), acetonitrile (ACN), and water. Unfortunately, these polar solvents are the only ones capable of dissolving numerous biological macromolecules like polypeptides, polysaccharides, and DNA, which prevents the use of Figure 1 to characterize their internal dynamics.

The goal of this project is to prepare a benchmark similar to that shown in Figure 1 for polymers dissolved in more polar solvents by preparing polymethacrylates with an oligo(ethylene glycol) methyl ether sidechain, that would be soluble in more polar solvents. The polymers would be labeled with pyrene and their fluorescence decays analyzed according to both the FBM and MFA to retrieve the parameters $\langle N_{\text{blob}} \rangle$, $\langle k_{\text{blob}} \times N_{\text{blob}} \rangle$, and $\langle k_{\text{MF}} \rangle^{\text{blob}}$.

EXPERIMENTAL

A series of pyrene-labeled poly(oligo(ethylene glycol) methyl ether methacrylate)s (Py-PEG_nMAs) were prepared, where the number n representing the number of ethylene glycol units

in the side chain equaled 1, 3, 9, and 19. 1-Pyrenebutyl methacrylate was prepared according to Scheme 1A and then copolymerized with different oligo(ethylene glycol) methyl ether methacrylates, according to Scheme 1B. The Py-PEG₁₉MA samples were prepared by graduate student Janine Thoma. The pyrene-labeled poly(methyl methacrylate) samples prepared by Shiva Farhangi¹⁰ were also used to characterize the dynamics of polymers having a low MW_{RU} in the more polar solvents.



Scheme 1. Preparation of (A) 1-pyrenebutyl methacrylate and (B) polymerization of 1-pyrenebutyl methacrylate and oligo(ethylene glycol) methyl ether methacrylate to yield Py-PEG_nMAs

The polymers were characterized by gel permeation chromatography (GPC) to determine their number and weight average molecular weights, and polydispersity.

Before fluorescence experiments were conducted, a sample of the polymer was dissolved in the chosen solvent to an absorbance of 0.1 OD at 344 nm to ensure that the pyrene concentration in the solution equaled 2.5×10^{-6} M. The solutions were degassed by bubbling a gentle stream of nitrogen gas through the solutions for 30 min for THF and ACN or 45 min for DMSO and DMF. Degassing was not done for the polymer solutions in water.

RESULTS AND DISCUSSION

The fluorescence decays of the monomer and excimer were analyzed according to both the FBM and MFA to yield the parameters $\langle N_{\text{blob}} \rangle$, $\langle k_{\text{blob}} \times N_{\text{blob}} \rangle$, and $\langle k_{\text{MF}} \rangle^{\text{blob}}$. The parameters retrieved in THF with the Py-PEG_nMA samples agreed with those previously found for a series of Py-PAMAs.¹⁰ Furthermore, the more polar side-chains of the PEG_nMAs enabled their dissolution in polar solvents, which allowed the creation of a benchmark, similar to that shown in Figure 1, for

the internal dynamics of polymers in DMF, DMSO, ACN, and water, as shown in Figure 2 for the parameter $\langle k_{\text{blob}} \times N_{\text{blob}} \rangle$.

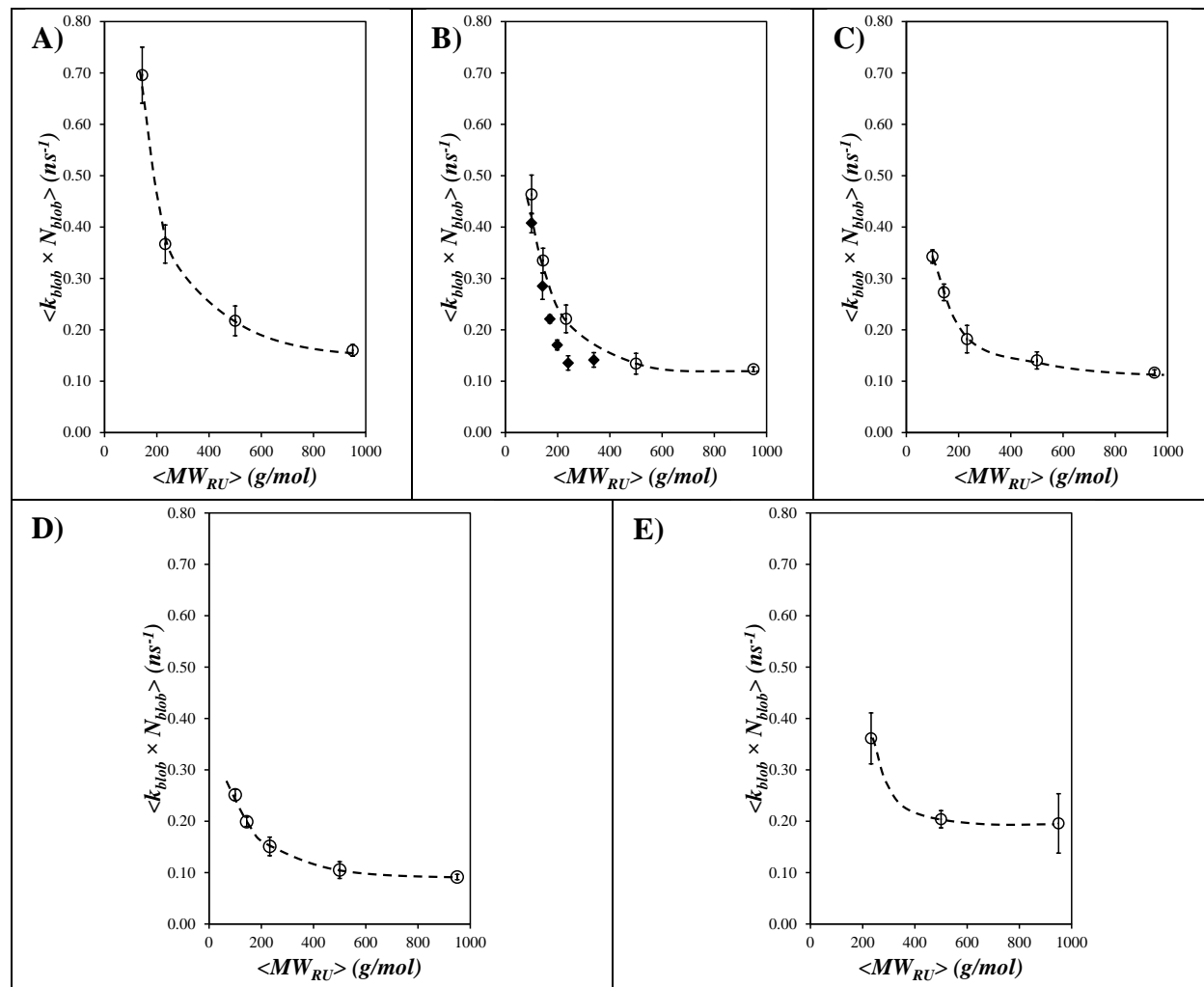


Figure 2. Plots of $\langle k_{\text{blob}} \times N_{\text{blob}} \rangle$ as a function of MW_{RU} for the (◆) Py-PAMAs and (○) PyPEG_nMAs in (A) ACN, (B) THF, (C) DMF, (D) DMSO, and (E) water.

The trends shown in Figure 2 indicate that $\langle k_{\text{blob}} \times N_{\text{blob}} \rangle$ decreases with increasing solvent viscosity with DMSO, the most viscous solvent, having the smallest $\langle k_{\text{blob}} \times N_{\text{blob}} \rangle$ values while ACN with the lowest viscosity yielded the highest $\langle k_{\text{blob}} \times N_{\text{blob}} \rangle$ values. A similar trend was seen for $\langle k_{\text{MF}} \rangle^{\text{blob}}$. As $\langle k_{\text{blob}} \rangle$ remained constant within experimental error at $10 \pm 2 \mu\text{s}^{-1}$ in all solvents but water, the differences in the $\langle k_{\text{blob}} \times N_{\text{blob}} \rangle$ -vs- MW_{RU} trends were due to larger $\langle N_{\text{blob}} \rangle$ values, indicating that the less viscous solvents allowed the pyrenyl labels to probe a larger blob volume.¹³ The main exception seems to be water. With a viscosity of 0.89 mPa•s, the effect of water on $\langle k_{\text{blob}} \times N_{\text{blob}} \rangle$ was expected to fall between that of DMF (0.794 mPa•s) and DMSO (1.99 mPa•s). However, inspection of Figure 2E and D revealed that the $\langle k_{\text{blob}} \times N_{\text{blob}} \rangle$ values in water are much closer to those in ACN. This is due to the twice larger $\langle k_{\text{blob}} \rangle^{\text{water}} = 18 \pm 2 \mu\text{s}^{-1}$, which when multiplied by $\langle N_{\text{blob}} \rangle$, increases the value of $\langle k_{\text{blob}} \times N_{\text{blob}} \rangle$. This effect is most likely related to the insolubility of pyrene in water, which results in the pyrenyls probing a much smaller volume,

namely the volume close to the polymethacrylate main chain, where they experience an environment that is similar to ethylene glycol. This smaller volume allows the pyrenyl labels to form excimer on a faster time scale as reflected by the twice larger $\langle k_{\text{blob}} \rangle$ value.

Evident in Figure 2 is the improvement in solubility of the Py-PEG_nMA in polar solvents enabled by the oligo(ethylene glycol) side chains. Py-PEG_nMA with EG_n side chains shorter than 3 ethylene glycol units did not benefit from this effect and were insoluble in water, while the poly(methyl methacrylate) polymers were insoluble in both water and ACN. Two more Py-PEG_nMA series will be prepared using side chains consisting of 4 and 5 ethylene glycol units to consolidate the trends shown in Figure 2.

The trends obtained in Figure 2 for the Py-PEG_nMA in DMF and DMSO could be used to compare the internal dynamics of other polymers. To this end, the $\langle k_{\text{blob}} \times N_{\text{blob}} \rangle$ values obtained for a series of copolypeptides prepared with different amino acids¹⁴ were compared to those of Py-PEG_nMA in DMF and DMSO. To account for the different number of atoms introduced into the backbone by the different structural units, the $\langle k_{\text{blob}} \times N_{\text{blob}} \rangle$ value was multiplied by the number of backbone atoms (N_{bb}) in Figure 3, where N_{bb} equaled 2 and 3 for the PEG_nMA and polypeptide samples, respectively.

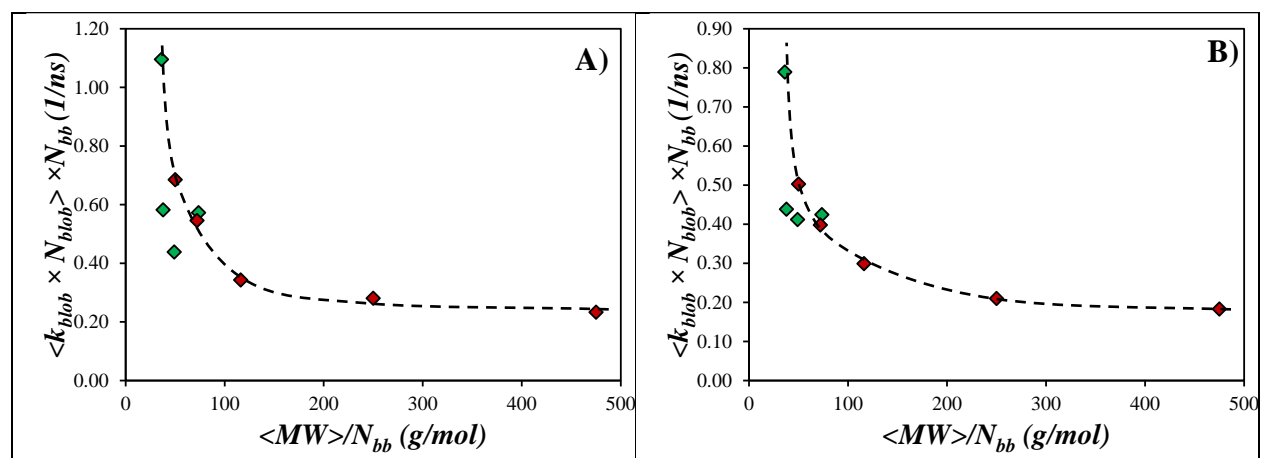


Figure 3. Plots of $\langle k_{\text{blob}} \times N_{\text{blob}} \rangle$ as a function of MW_{RU} for (◆) polypeptides and for (◆) PyPEG_nMA in (A) DMF and (B) DMSO.

As illustrated in Figure 3, the internal dynamics of the polypeptides were fairly similar to those of the PyPEG_nMA. The observation that the internal dynamics of polypeptides were significantly different from those expected for polymers in solution suggested that the ability of polypeptides to fold into complex 3D structures is not due to an abnormality in their internal dynamics.

CONCLUSIONS

A series Py-PEG_nMA samples was synthesized and their internal dynamics were characterized by determining the product $\langle k_{\text{blob}} \times N_{\text{blob}} \rangle$ in five different solvents. Plotting $\langle k_{\text{blob}} \times N_{\text{blob}} \rangle$ as a function of MW_{RU} in each solvent yielded trends that can be used to assess the internal dynamics of any other polymer in these solvents. A first application of this work was to investigate whether the internal dynamics of polypeptides, which control protein folding, is different from that of synthetic polymers.

REFERENCES

1. Rudin, A. *The Elements of Polymer Science & Engineering*; Elsevier Science & Technology Books, 1998, pp 394-403
2. Huber, R. Flexibility and Rigidity, Requirements for the Function of Proteins and Protein Pigment Complexes. *Biochem. Soc. Trans.* **1987**, *15*, 1009–1020.
3. Fox, T. G.; Flory, P. J. Second-Order Transition Temperatures and Related Properties of Polystyrene. I. Influence of Molecular Weight. *J. Appl. Phys.* **1950**, *21*, 581–591.
4. Rogers, S. S.; Mandelkern, L. Glass Formation in Polymers. I. The Glass Transitions of the Poly-(n-Alkyl Methacrylates). *J. Phys. Chem.* **1957**, *61*, 985–990.
5. Duhamel, J. New Insights in the Study of Pyrene Excimer Fluorescence to Characterize Macromolecules and Their Supramolecular Assemblies in Solution. *Langmuir* **2012**, *28*, 6527–6538.
6. Duhamel, J. Global Analysis of Fluorescence Decays to Probe the Internal Dynamics of Fluorescently Labeled Macromolecules. *Langmuir* **2014**, *30*, 2307–2324.
7. Mathew, A. K.; Siu, H.; Duhamel, J. A Blob Model To Study Chain Folding by Fluorescence. *Macromolecules* **1999**, *32*, 7100–7108.
8. Yip, J.; Duhamel, J.; Bahun, G. J.; Adronov, A. A Study of the Dynamics of the Branch Ends of a Series of Pyrene-Labeled Dendrimers Based on Pyrene Excimer Formation. *J. Phys. Chem. B* **2010**, *114*, 10254–10265.
9. Siu, H.; Duhamel, J. Comparison of the Association Level of a Pyrene-Labeled Associative Polymer Obtained from an Analysis Based on Two Different Models. *J. Phys. Chem. B* **2005**, *109*, 1770–1780. Farhangi, S.; Weiss, H.; Duhamel, J. Effect of Side-Chain Length on the Polymer Chain Dynamics of Poly(Alkyl Methacrylate)s in Solution. *Macromolecules* **2013**, *46*, 9738–9747.
10. Farhangi, S.; Weiss, H.; Duhamel, J. Effect of Side-Chain Length on the Polymer Chain Dynamics of Poly(Alkyl Methacrylate)s in Solution. *Macromolecules* **2013**, *46*, 9738–9747.
11. Thoma, J. L.; Duhamel, J.; Li, M. J.; Bertocchi, M. J.; Weiss, R. G. Long-Range, Polymer Chain Dynamics of a “Stiff” Polymer. Fluorescence from Poly(Isobutylene-Alt-Maleic Anhydride) with N-(1-Pyrenylmethyl)Succinimide Groups. *Macromolecules* **2017**, *50*, 3396–3403.
12. Thoma, J.; Duhamel, J.; Bertocchi, M.; Weiss, R. Long Range Polymer Chain Dynamics of Highly Flexible Polysiloxane in Solution Probed by Pyrene Excimer Fluorescence. *Polymers*. **2018**, *10*, 345.
13. Yip, J.; Duhamel, J.; Qiu, X. P.; Winnik, F. M. Long-Range Polymer Chain Dynamics of Pyrene-Labeled Poly(N -Isopropylacrylamide)s Studied by Fluorescence. *Macromolecules* **2011**, *44*, 5363–5372.
14. Casier, R.; Duhamel, J. The Effect of Amino Acid Size on the Internal Dynamics and Conformational Freedom of Polypeptides. *Macromolecules* **2020**, *53*, 9811–9822.

Remi Casier
Chemistry
Waterloo

Predicting the Folding Time of Proteins Based
on Pyrene Excimer Formation Measurements
on Polypeptides

Predicting the Folding Time of Proteins Based on Pyrene Excimer Formation Measurements on Polypeptides

Remi Casier and Jean Duhamel

INTRODUCTION

Proteins are biological macromolecules composed of linear polypeptide chains. Often, a specific three-dimensional arrangement of the constituting polypeptides is required for the protein to have a biological function. Despite the seemingly infinite conformational space available to an unfolded polypeptide, that should theoretically lead to infinitely long folding times, in practice proteins are capable of folding on the order of milliseconds to seconds. One solution to this paradox, also referred to as Levinthal's paradox,¹ can be found through the concept of folding domains. A folding domain is defined as a group of amino acids (*aa*'s) contained within a subvolume of a protein, which cooperatively interact as the protein folds. The ability of folding to take place simultaneously in each folding domain, often described as *foldons*,² significantly reduces the conformational space available to a folding polypeptide and therefore can circumvent the folding-time paradox.

Although the existence of *foldons* has been demonstrated through hydrogen-exchange experiments,² there remain many unanswered questions about these domains such as a rationale for their existence and for their fairly narrow size distribution centered around ~25 *aa*'s. Answering these questions for a protein in an unfolded state is a tricky problem, that requires the establishment of a theoretical framework to enable a mathematical description of polypeptide chain dynamics in solution. Therefore, it was the goal of this research to study the effects that each *aa* had on the solution conformation of polypeptides, and to use this information to develop a *blob*-based approach, where a *blob* would be the mathematical equivalent to an experimental *foldon*, to calculate the folding time of proteins to gain a better understanding of the fundamental principles governing the folding process.

EXPERIMENTAL

A series of random copolypeptides were synthesised via ring-opening copolymerization of the *N*-carboxyanhydrides (NCAs) of *D,L*-glutamic acid (Glu) and one of glycine (Gly), *D,L*-alanine (Ala), or ϵ -carboxybenzyl-*D,L*-lysine (Lys(Z)) yielding PGlyGlu, PAlaGlu, and PLys(Z)Glu, respectively.^{3,4} The chemical structures of the polypeptides are given in Figure 1. Since it is the goal of this research to quantify the domain size of polypeptides in their unfolded state, the polypeptides were synthesized using racemic mixtures of *D,L-aa*'s to suppress the formation of ordered structures. The polypeptides were labeled with the dye pyrene and their internal dynamics were gauged based on their ability to form an excimer upon the encounter of an excited and ground-state pyrene. The fluorescence decays of the pyrene-labeled polypeptides were analyzed using the Fluorescence *Blob* Model (FBM). The FBM divides a macromolecule into a series of subvolumes of equal size, referred to as *blobs*. Utilizing this *blob*-based tool, the FBM can provide information on the local chain conformation through the parameter N_{blob} , which is the number of structural units capable of locally interacting with one another in a *blob*. Consequently, application of the FBM to unstructured polypeptides yields information on the number of *aa*'s capable of cooperatively interacting together. This makes the *blobs* generated by the FBM analysis analogous to protein *foldons*,⁵ and therefore allows the FBM to provide insight into the nature of protein folding.

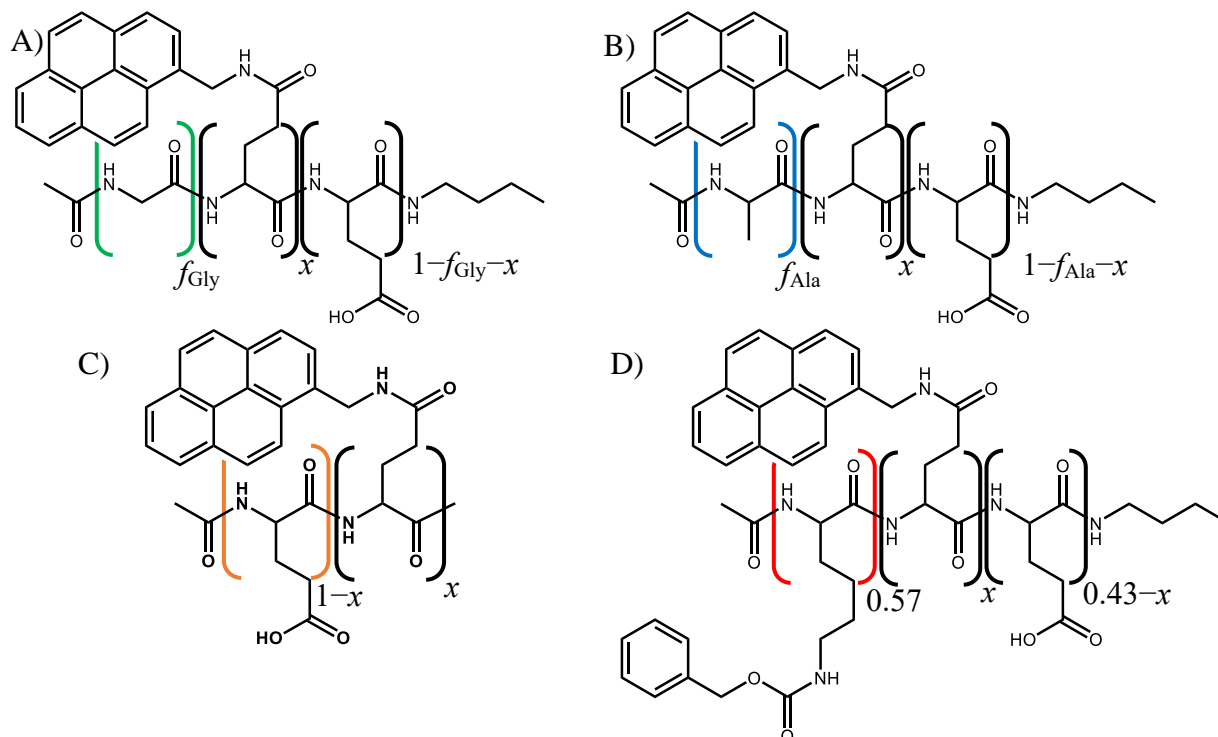


Figure 1. Chemical structures of A) Py-PGlyGlu, B) Py-PAlaGlu, C) Py-PGlu, and D) Py-PLys(Z)Glu. All stereocenters are racemic.

RESULTS AND DISCUSSION

Amino Acid Side Chain Size: A series of copolymers (Fig. 1) were prepared containing Glu and one of Gly, Ala, or Lys(Z). In this manner the effect, that each *aa* had on a polypeptide's conformation could be studied in a systematic manner. To quantify the difference between the *aa*'s, each *aa* was defined in terms of its side chain size (SCS). SCS was defined as the number of non-hydrogen atoms contained in an *aa*'s side chain and provides a simple means to quantify the side chain bulkiness. To ensure that the only difference between the copolymers was the SCS of the copolymerized *aa*, the copolymers were chosen such that a Glu content of ~ 45 mol% was kept similar between the samples. For each copolymer, N_{blob} was found to be independent of the pyrene content, indicating that pyrene

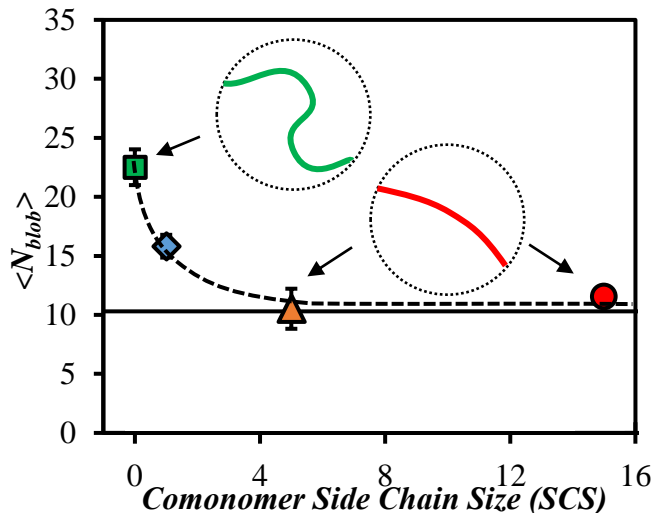


Figure 2. Plot of N_{blob} as a function of the SCS of the comonomer for (■, SCS = 0) Py-PGlyGlu, (◆, 1) Py-PAlaGlu, (▲, 5) Py-PGlu, and (●, 15) Py-Lys(Z)Glu in DMSO. The dashed line was added to guide the eye. The solid line indicates the $N_{\text{blob}}^{\text{theo}}$ value of 10 (± 1) for an extended polypeptide in a coiled conformation. A schematic representation of the local backbone conformation within a *blob* is provided as an inset.

was not altering the polypeptides behavior. The N_{blob} values for each polypeptide were then averaged across the pyrene contents and plotted as a function of SCS in Figure 2.

Figure 2 shows that N_{blob} quickly decreased with increasing SCS, reaching a plateau for SCS above 4 atoms. This indicated that the increase in SCS rapidly increased the sterics between the side chains, which led to a straightening of the backbone on the few nm length-scale of a *blob*.³ The plateau $N_{\text{blob}} = 11 (\pm 1)$ value obtained for PGlu and PLys(Z)Glu indicated that the side chains of Glu and Lys(Z) were sufficiently bulky to fully elongate the polypeptide backbone, and therefore any polypeptides containing *aa*'s with SCS's of 5 or more are all expected to have the same *blob* size of ~ 11 *aa*'s. This conclusion was supported by molecular mechanics optimization which found a theoretical $N_{\text{blob}}^{\text{theo}}$ value equal to 10 (± 1) for a polypeptide in an extended conformation,^{4,5} matching the experimentally determined N_{blob} value. Interestingly, Figure 2 suggests that there is only a significant change in N_{blob} when either Ala or Gly are incorporated, and given that they are the two smallest *aa*'s, this suggests that the presence of these two *aa*'s are most important for defining *foldon* sizes.

Amino Acid Incorporation: Although Figure 2 demonstrates that the incorporation of small *aa*'s increases the number of *aa*'s capable of diffusively encountering one another, the increase was only observed when the small *aa*'s constituted a rather significant portion of the polypeptides sequence (~ 55 mol%). Since proteins often contain significantly lower fractions of these *aa*'s, two series of copolypeptides were prepared to investigate how the *blob* size responded to the level of incorporation of Ala and Gly. Plots of N_{blob} for PAlaGlu and PGlyGlu as a function of comonomer incorporation are given in Figures 4A and B, respectively. It was expected that the incorporation of Ala or Gly would result in a continuous increase in N_{blob} . Instead, both figures indicated that the conformation of the polypeptides were essentially independent of the *aa* content and that only a low level of incorporation (>24 mol% Ala and >15 mol% Gly) was required to enhance the polypeptides conformational freedom and therefore domain size. The fact that N_{blob} was independent of the *aa* content and that the increase in N_{blob} persisted at low levels of incorporation suggests that the local conformation of polypeptides may simply be dictated by the presence of a select few *aa*'s such as Ala and Gly.

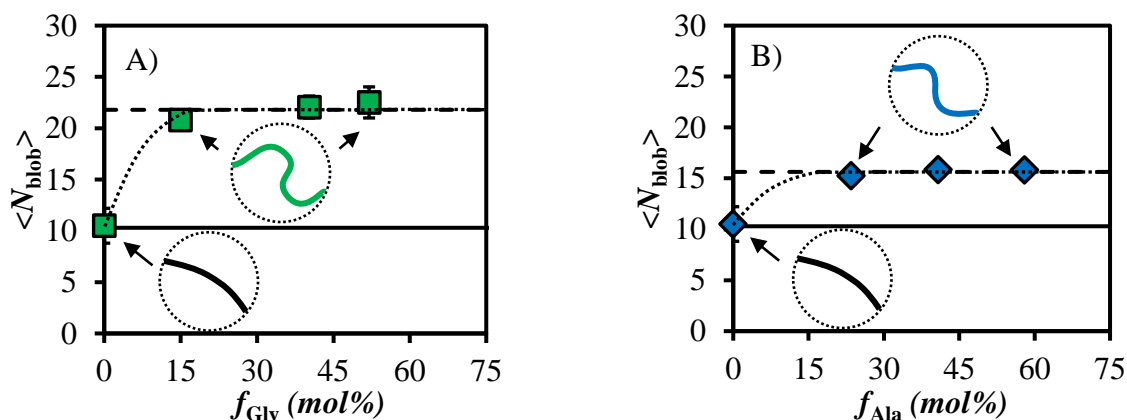


Figure 3. Plots of N_{blob} as a function of comonomer composition for A) Py-PGlyGlu and B) Py-PAlaGlu. The solid lines indicate the theoretical $N_{\text{blob}}^{\text{theo}}$ value of 10 (± 1) for a rigid and extended polypeptide. The dashed lines equal the N_{blob} plateau values of A) 22 (± 1) and B) 16 (± 1). The dotted lines were added to guide the eye. A schematic representation of the local backbone conformation within a *blob* is provided as an inset.

Protein Folding Domain Size: Since protein *foldons* and polypeptide *blobs* are analogous to one another, it is logical that the *foldon* size would respond to *aa* composition in the same manner as *blobs*. On average, proteins contain 7.8 and 7.3 mol% of Ala and Gly, respectively.⁶ Therefore, it is statistically expected that any given domain of ~ 25 *aa*'s within a protein will contain several Ala and/or Gly's. Knowing that the inclusion of Ala and Gly results in a relatively large domain size of 16 – 23 *aa*'s (Figure 2) and that these domain sizes persist, even at low levels of incorporation (Figures 3A and B), it is expected that a folding domain in a protein would be constituted of $\sim 19 = (16+23)/2$ *aa*'s, which would have a $>95\%$ probability of containing at least one Gly or one Ala.

Calculating Protein Folding Times: For a protein to fold, the unfolded polypeptide chain must undergo a conformational search, and therefore the time it takes to fold is equivalent to the time it would take the chain to probe its available conformational space. Taking advantage of the fact that folding occurs in domains and using *blobs* to represent these domains, the number of conformations available to an unfolded protein can be divided into two simple steps. The first step would determine the number of conformations (Ω_B) available to the *aa*'s within a *blob*. Since the *blobs* must also rearrange among themselves

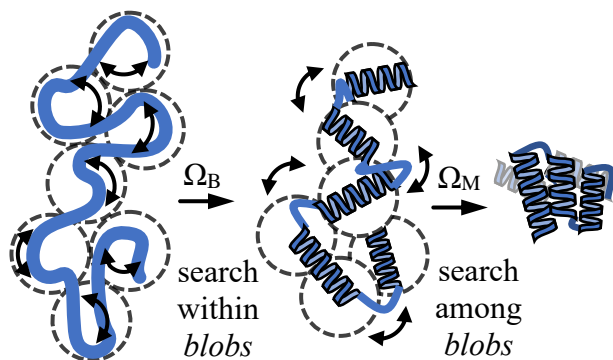


Figure 4. Schematic representation of a conformational search of a folding protein compartmentalized into domains or *blobs*.

before the native conformation can be found, the second step would determine the number of conformations (Ω_M) available among the *blobs*. A depiction of this folding process is given in Figure 4. If the *blob* size and number of *blobs* is known, Ω_B and Ω_M can be readily calculated using Equation 1. Equation 1 is a result of renormalization group theory and provides the number of unique conformations among n units in a chain.⁴ In Equation 1, the value of n equals the *blob* size or the number of *blobs* when calculating Ω_B or Ω_M , respectively.

$$\Omega(n) = 1.17 \cdot (n-1)^{\frac{1}{6}} \cdot 3.19^{n-2} \quad (1)$$

Based on Figure 4, the total number of searchable conformations is given by $\Omega_B \times \Omega_M$. Multiplying this value by the timescale of local polypeptide molecular motions (~ 1 ps)⁷ yields the total conformational search time (*tcst*), which is simply equal to the time it would take the protein to fold assuming folding followed a random conformational search. Based on this method, only two factors are needed to calculate *tcst*: the *blob* size and the number of *blobs* contained within a protein. As discussed above, a protein *blob* contains ~ 19 *aa*'s and since the *blob* size is expected to be more-or-less constant, the number of *blobs* contained within a protein is simply equal to its chain length (*DP*) divided by the *blob* size of 19. Following this simple logic, the *tcst* of 144 proteins was calculated using Equation 2. These *tcst*'s were then compared to the experimentally measured folding times in Figure 5.

$$tcst = \Omega_M \times \Omega_B \times 1ps \quad (2)$$

The $tcst$ of the 144 proteins matched rather well with their experimentally observed folding times, resulting in a correlation coefficient of 0.75, placing this method among some of the best experimentally-based correlation trends reported in the literature. Moreover, this *blob*-based method can be readily applied to any protein regardless of its size, structural class, or folding kinetics, which are often limitations of other methods in the literature. Furthermore, this is the first procedure based on experimentally-obtained results which generates a direct 1-to-1 correspondence between the calculated and experimentally determined folding times of proteins. The fact that this simple method is capable of directly predicting folding times based solely on local chain conformation suggests that protein folding may simply be a consequence of polypeptide chain dynamics despite the seemingly vast complexity of proteins.

CONCLUSIONS

Taking advantage of the FBM's ability to compartmentalize polypeptides into subvolumes, the size of polypeptide folding domains was investigated as a function of their *aa* sequence. Due to the inherent rigidity of polypeptides, most *aa*'s are expected to generate domain sizes of ~ 11 *aa*'s. However, the presence of small *aa*'s such as Ala or Gly were found to significantly increase the polypeptides flexibility, therefore increasing the number of *aa*'s contained within a domain. Surprisingly, the increased size did not depend on the amount of Ala or Gly incorporated in the polypeptide, even at levels as low as 15 mol%. These results indicated that the mere presence of Ala and Gly in a proteins sequence is sufficient to increase the proteins domain size to ~ 19 *aa*'s. Based on these results, a *blob*-based method was developed to calculate the $tcst$ of proteins. The *blob*-based approach generated a correlation coefficient of 0.75 between the calculated and experimentally observed folding times for 144 proteins. The ability of this method to directly predict protein folding times demonstrates that both the existence of folding domains and the ability of proteins to rapidly fold are merely consequences of polymer chain dynamics.

REFERENCE

- ¹ Levinthal, C. *Spectroscopy in Biological Systems. Proceedings University of Illinois Bulletin* **1969**, University of Illinois Press, Urbana, IL, pp 22 – 24.
- ² Englander, S. W.; Mayne, L. *Proc. Natl. Acad. Sci. U. S. A.* **2014**, *111*, 15873 – 15880.
- ³ Casier, R. and Duhamel, J. *Macromolecules* **2020**, *53*, 9811 – 9822.
- ⁴ Casier, R. and Duhamel, J. *Macromolecules* **2020**, *53*, 9823 – 9853.
- ⁵ Casier, R. and Duhamel, J. *Macromolecules* **2018**, *51*, 3450 – 3457.
- ⁶ Brooks, D. J.; Fresco, J. R.; Lesk, A. M.; Singh, M. *Mol. Biol. Evol.* **2002**, *19*, 1645 – 1655.
- ⁷ Plotkin, S. S.; Onuchic, J. N. *Q. Rev. Biophys.* **2002**, *35*, 111 – 167.

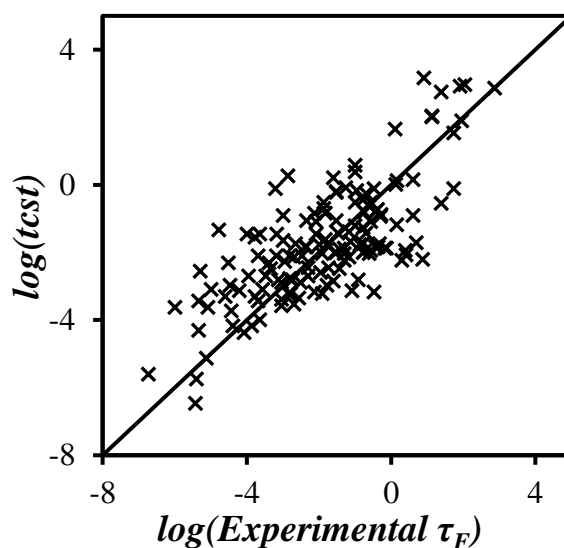


Figure 5. Log-log plot of the total conformational search time ($tcst$) of a protein folding via a *blob*-based model as a function of experimentally determined protein folding times. Folding times are given in seconds. The solid line represents the line of equality. Correlation coefficient $r = 0.75$.

Rebecca Lo
Chemistry
Waterloo

Synthesis of Macrocycles via Migration Insertion Polymerization

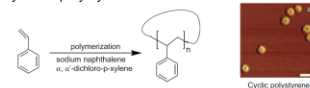
Synthesis of Macrocycles via Migration Insertion Polymerization

Rebecca Lo
Supervisor: Professor Xiaosong Wang
May 5th, 2021

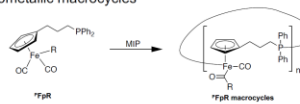


Synthesis of Macrocycles

- Organic macrocycles – polystyrene



- Organometallic macrocycles

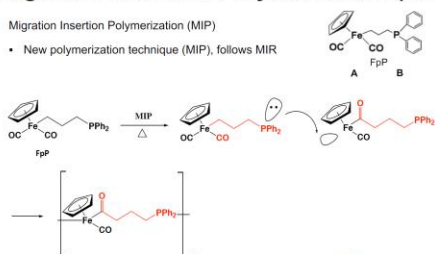


J. Am. Chem. Soc. 2008, 130, 14634-14639

Migration Insertion Polymerization (MIP)

Migration Insertion Polymerization (MIP)

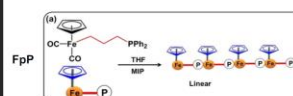
- New polymerization technique (MIP), follows MIR



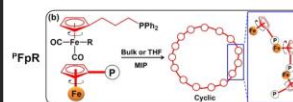
J. Am. Chem. Soc. 2013, 135, 3399-3402



MIP by different monomers



- Linear polymer, P(FpP), formed through MIP

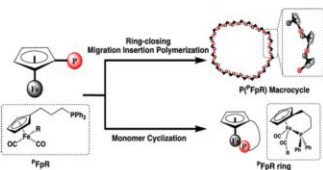


- Cp-Fe coordination bond with low rotational barrier
- Presence of Cp-Fe in the backbone render the chain rotatable

Chem. Eur. J. 2018, 24, 15380 - 15386



Competition during cyclization

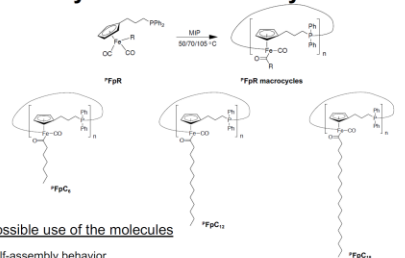


- Ring-closing MIP is favored at high concentration condition
=> >70 wt % in THF at 60 °C
- Monomer cyclization is favored at low concentration condition
=> 1 wt % in THF at 60 °C

Organometallics 2020, 39, 2991-2997



Synthesized macrocycles



Possible use of the molecules

- Self-assembly behavior
- Small rings and macrocycles



Helen Dawit
Chemical Engineering
Ryerson

Modeling Average Molecular Weight Properties
of PBMA via ARGET/AGET ATRP

BY: HELEN DAWIT, MASc
CANDIDATE
SUPERVISOR: DR. RAMDHANE
DHIB

MODELING AVERAGE MOLECULAR WEIGHT PROPERTIES OF PBMA VIA ARGET ATRP

ACTIVATORS REGENERATED BY ELECTRON TRANSFER (ARGET) ATOM TRANSFER RADICAL POLYMERIZATION (ATRP)

- CRP technique that results in lower PDI and narrow molecular weight distribution compared to FRP
- Reversible reaction between active radicals and dormant species
- ARGET uses less Catalyst due to reducing agent- more environmentally friendly

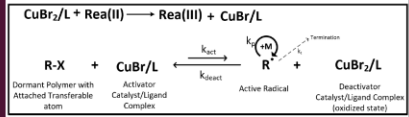


Figure 1: ARGET Reducing Reaction and ATRP Reversible Reaction

CONTINUOUS STIRRED TANK REACTOR DESIGN

- Objective: Model the Average Molecular Properties (average molecular weight and PDI) of PBMA in a CSTR

Table 1: Experimental Reagents

Reactants	Chemical Components	
	Name	Symbol
Monomer	n-butyl methacrylate	M
Initiator	Ethyl-2-bromoisobutyrate	I
Catalyst	Copper (II) bromide	CuBr ₂
Ligand	Tris(2-pyridyl)methylamine	L
Reducing Agent	Tin(II) 2-ethylhexanoate	R ²⁺
Alkyl Halide	Bromine	X
Solvent	Anisole	S/A

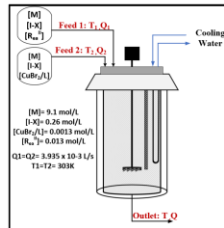


Figure 2: Continuous Stirred Tank Reactor

MODELING TECHNIQUE AND SOLVING METHOD

- Method of Moments
- System of 21 ODE's
 - > 10 from the molar balances
 - > 2 from the energy balances
 - > 9 from the moment balances
- Solved via MATLAB ODE built-in function 'ode15s'

Molar Balance

Example for Reducing Agent:

$$\frac{d[R_2^{2+}]}{dt} = -k_{\text{act}}[R_2^{2+}][CuBr_2/L] + \frac{[R_2^{2+}]_i V_i}{V} - \frac{[R_2^{2+}]_o V_o}{V}$$

Energy Balance

$$\frac{dT}{dt} = \frac{T_1 Q_1}{V} + \frac{T_2 Q_2}{V} - \frac{U A (T - T_c)}{V \rho C_p} + \frac{(-\Delta H_{\text{rxn}} R_p)}{\rho C_p}$$

Moments

$$\lambda_i = \sum_{j=1}^i i^j [R_j]$$

$$e_i = \sum_{j=1}^i j^i [X - R_j]$$

$$\mu_i = \sum_{j=1}^i j^i [P_j] \quad i = 0, 1, 2$$

Average Molecular Properties

$$\bar{M}_n = \frac{(\lambda_1 + \mu_1 + e_1)}{(\lambda_0 + \mu_0 + e_0)} M_{w, \text{monomer}}$$

$$\bar{M}_w = \frac{(\lambda_2 + \mu_2 + e_2)}{(\lambda_1 + \mu_1 + e_1)} M_{w, \text{monomer}}$$

$$PDI = \frac{\bar{M}_w}{\bar{M}_n}$$

CSTR RESULTS

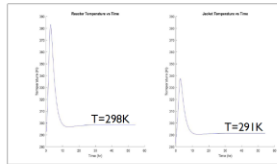


Figure 3: Reactor and Jacket Temperature

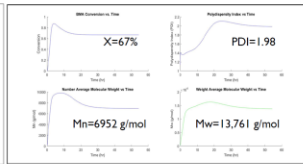


Figure 4: Conversion and Average Molecular Properties

FUTURE WORK

- Limitation: low conversion attained due to low temperature
- Solution: designing a controller to keep reactor temperature at a higher constant value
- No paper published on implementing control systems for ARGET ATRP
- Creating a model for ARGET ATRP in Emulsion (environmentally and economically advantageous compared to solution)

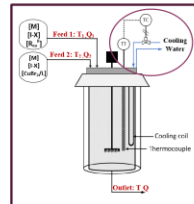


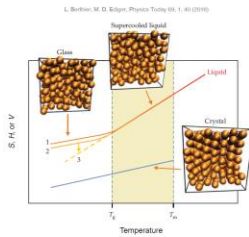
Figure 5: CSTR with Temperature Control

Thank you for watching!

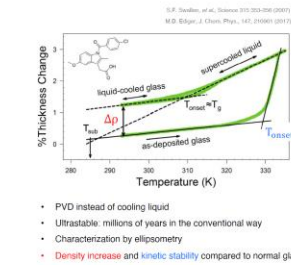
Junjie Yin
Physics and Astronomy
Waterloo

Stable Polystyrene Glasses through PVD and UV radiation

Glass and stable glass



Stable polystyrene glasses through PVD and UV radiation – Junjie Yin, Adam Raegen, James Forrest



- PVD instead of cooling liquid
- Ultrastable: millions of years in the conventional way
- Characterization by ellipsometry
- Density increase and kinetic stability compared to normal glass

PAGE 1

Stable polymeric glasses

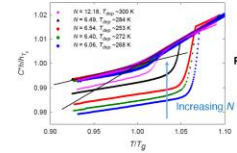
- Difficulties:
- Low vapor pressures
 - Sensitive to thermal degradation

- Possibilities:
- Start with small N
 - Successful distillation of PS (N of 3–13), PEO (N of 7–13) and PMMA ($N = 7$)

- Atactic PS:
- No crystal ground state
 - Surface dynamics well studied



A. Raegen, J. Yin, Q. Zhou, & J. A. Forrest (2020). *Nature Materials*, 19(10), 1110–1113.



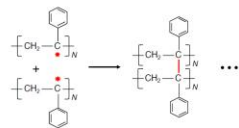
Practical limit: $N \sim 12$

Stable polymer glass:
kinetic stability, low T_g , and increased density

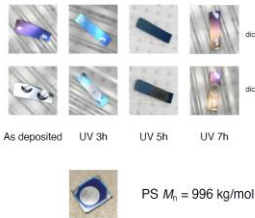
Stable polystyrene glasses through PVD and UV radiation – Junjie Yin, Adam Raegen, James Forrest

PAGE 2

UV crosslinking makes network glasses



UV radiation at 254 nm on PS:
Crosslinking (inert atmosphere) by dehydrogenation

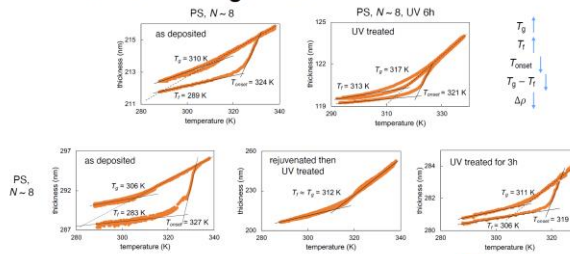


PS $M_n = 996$ kg/mol

Stable polystyrene glasses through PVD and UV radiation – Junjie Yin, Adam Raegen, James Forrest

PAGE 3

Crosslinked stable glasses



Stable polystyrene glasses through PVD and UV radiation – Junjie Yin, Adam Raegen, James Forrest

PAGE 4

Conclusions

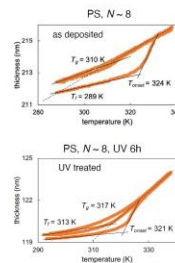
- PVD: PS stable glasses with N of 5–12
- PVD + UV: PS network stable glasses with $N \rightarrow \infty$
- UV radiation reduces kinetic stability

Future work

- Systematic study: UV time, starting N , substrate temperature, deposition rate
- Minimize loss of stability due to UV radiation

Stable polystyrene glasses through PVD and UV radiation – Junjie Yin, Adam Raegen, James Forrest

PAGE 5



Sanjay Patel
Chemistry
Waterloo

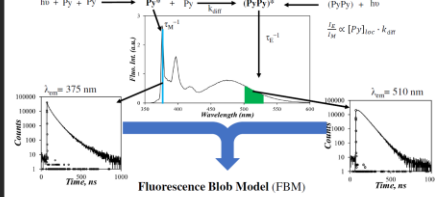
Probing Conformation of Structured
Macromolecules in Solution by Pyrene Excimer
Fluorescence

Probing the Conformation of Structured Macromolecules in Solution by Pyrene Excimer Fluorescence

By: Sanjay Patel
Supervisor: Jean Duhamel

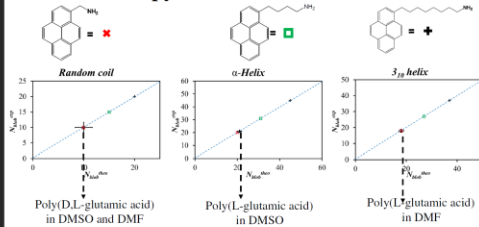


Pyrene Excimer Fluorescence



→ Able to distinguish between dynamics and $[Py]_{loc}$

Comparison of N_{blob} for different structures and pyrene derivatives

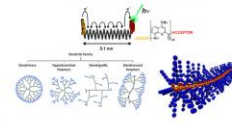


Macromolecules

- Biological macromolecules:**
- Polysaccharide → Ex. Starch, Glycogen
 - Nucleic acids → Ex. DNA, RNA
 - Proteins



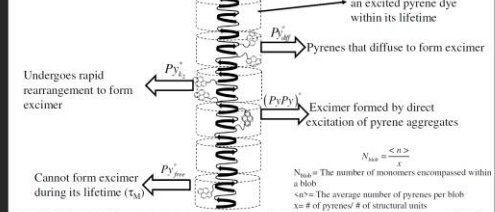
Synthetic macromolecules:



Methods to Probe Macromolecules

- X-ray Crystallography
- Circular Dichroism
- Light Scattering
- Scanning electron microscopy

Fluorescence Blob Model (FBM)



Duhamel, J. Global analysis of fluorescence decays to probe the internal dynamics of fluorescently labeled macromolecules. *Langmuir* 2013, 30, 2307-2324.

Acknowledgements

- Supervisor: Prof. Jean Duhamel
- The Duhamel and Gauthier Groups



Franklin Frasca
Chemistry
Waterloo

Gel Permeation Chromatography Analysis to Predict the Composition of PIBSI Dispersants

GPC Analysis to Predict the Composition of PIBSI Dispersants

Franklin Frasca and Jean Duhamel

INTRODUCTION

Engine oils work by forming a thin layer upon compression, which decreases wear by reducing metal-on-metal contacts.¹⁻³ Additives are introduced in engine oils for a variety of economical and environmental reasons such as fuel efficiency and mitigation of exhaust pollution, respectively. While the mixture of additives can vary between different lubricating oils depending on the application, the additive of interest in this work is dispersants.

Dispersants are polymeric additives designed to suspend insoluble matter in the oil and prevent their aggregation into particulates that would become large enough to precipitate. Dispersion is often achieved with block copolymers containing both polar and apolar segments. The polar segments associate to the surface of the particulates, while the larger apolar segments prevent further particulate aggregation through steric stabilization.^{3,4}

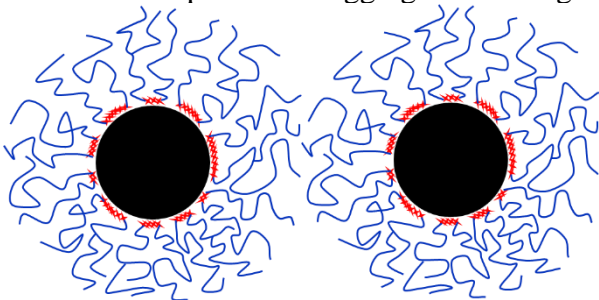
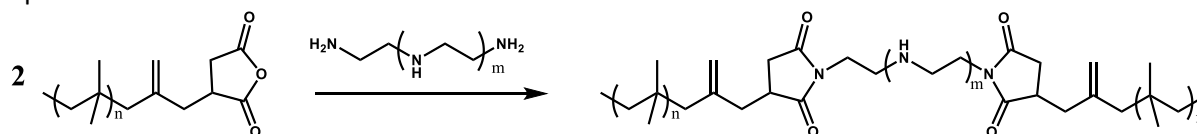


Figure 1. Steric stabilization of dispersed particles.

The dispersants most commonly used today are constituted of polyisobutylene (PIB) apolar segments and polyamines as the polar core. Two polyisobutylenes terminated with succinic anhydride groups (PIBSAs) can be linked via reaction of a polyamine with two terminal succinic anhydrides (SAs) according to Scheme 1 to form *bis*-polyisobutylene succinimides (*b*-PIBSIs).^{2,3}



Scheme 1. General scheme for the synthesis of *b*-PIBSI dispersants.

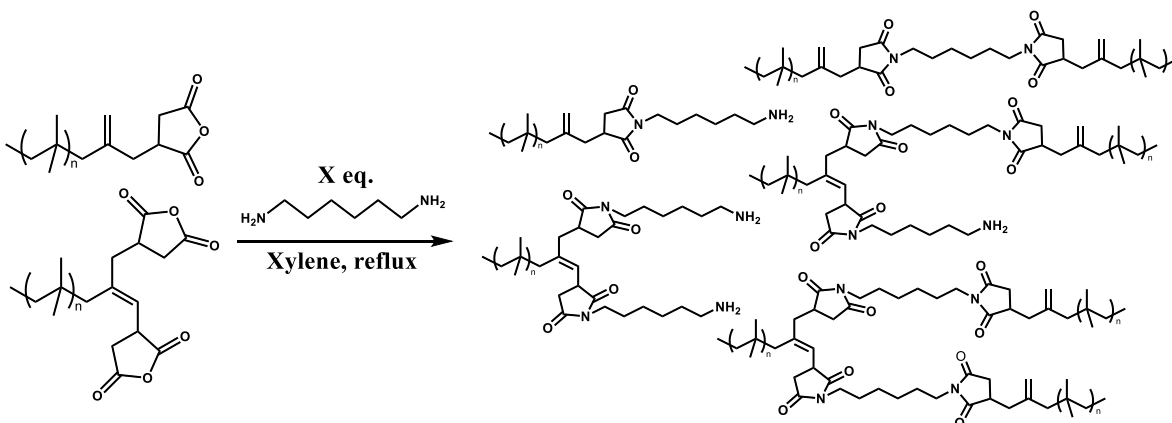
Unfortunately, the ideal *b*-PIBSI product depicted in Scheme 1 is often contaminated by the presence of PIBSI-trimers (*tri*-PIBSIs) or other higher-order PIBSIs, which are generated by doubly-maleated PIBSAs (PIBSA₂) during the imide coupling reaction. The PIBSA₂ species is an impurity found in any PIBSA sample, which is the result of PIB chains having been maleated twice. Since the architecture of PIBSI dispersants is directly correlated to the performance of the oil they are dissolved in, the characterization and prediction of their architecture has been the object of sustained research. In this context, the succinic anhydride content of PIBSA samples, which can be calculated by FTIR analysis,⁵ and the molar fraction (f_{doubly}) of PIBSA₂ in a PIBSA sample, which can be determined by fluorescence,⁶ are important parameters to help predict the chemical composition of a reaction mixture resulting from the coupling of a PIBSA sample and a polyamine.

However, the characterization of PIBSI products suffers from a variety of complications when attempting to use conventional methods such as ¹H NMR and FTIR spectroscopy. The signals of the amine hydrogens and succinimide carbonyls of PIBSI dispersants in, respectively, the ¹H NMR and FTIR spectra have shown substantial distortions due to hydrogen bonding between the two groups.⁷ The lack of monodisperse low molecular weight PIB standards and the low dn/dc values for PIB in tetrahydrofuran (THF) complicate the quantitative GPC analysis using a conventional calibration curve. These issues present difficult experimental challenges to overcome in the analysis of PIBSI products.

While PIBSI products can be difficult to characterize, it might be possible to circumvent this problem by simulating the expected PIBSI products based on the f_{doubly} value determined from fluorescence experiments. In turn, the molecular weight distribution (MWD) of the expected PIBSI products could be used to predict the overall MWD of a PIBSI sample determined by GPC analysis. Based on these considerations, a series of coupling reactions between PIBSA and hexamethylene diamine (HMDA) were conducted with varying amine-to-succinic anhydride ratios ($N_{\text{Am}}/N_{\text{SA}}$) to produce a series of PIB(HM)SI samples, whose MWD was characterized by GPC analysis of the DRI traces. Different reaction simulation programs were then applied to predict the MWD of the different PIBSI products generated by the coupling reactions conducted with different $N_{\text{Am}}/N_{\text{SA}}$ molar ratios. The simulated MWDs of the predicted PIBSI products were then transformed into a theoretical DRI trace which was then compared to the experimental DRI trace obtained for the PIBSI products. The best agreement between the simulated and experimental DRI traces was obtained by assuming that steric hindrance prevented the formation of high-order PIBSI products when they were prepared from HMDA. By enabling the quantitative prediction of the nature of the PIBSI products obtained from the reaction between a PIBSA sample and HMDA, this study opened the path for using a combination of GPC, fluorescence, and FTIR analysis to predict the composition of product mixtures resulting from the reaction of PIBSA with more complex polyamines.

EXPERIMENTAL

Two simulation programs were written to take into account the molar fraction (f_{doubly}) of PIBSA chains, that were doubly maleated (PIBSA₂). The programs randomly selected one succinic anhydride (SA) and one amine in the reaction mixture to couple them and form a PIBSI product. When all amines or SA had run out, the program *reaction3* stopped and summarized the number of unreacted PIBSA and mono-, bis-, tri- ... PIBSI products left in the reaction mixture. A similar simulation program, *reaction4*, was implemented with the assumption that steric hindrance prevented the formation of higher-order PIBSI products. Using the molecular weight distribution (MWD) of the PIBSA sample determined from GPC analysis the MWD of the *b*-PIBSI and higher-order PIBSI products could be estimated.



Scheme 2. Synthesis of PIBSI-HMDA.

To validate the composition of reaction products obtained from the simulated coupling reactions of PIBSA and HMDA, experimental data were generated by coupling a PIBSA sample of known f_{doubly} with HMDA for amine-to-SA ratios ($N_{\text{Am}}/N_{\text{SA}}$) varying between 0.25 and 2.00 to create mixtures of reactants and products having different compositions according to Scheme 2.

The MWDs of the PIB(HM)SI samples were then determined through GPC analysis with a differential refractometer, generating a DRI trace for each PIB(HM)SI sample. The DRI traces were baseline corrected and could be fitted with a sum of Gaussians as a function of either elution volume (V_{el}) or degree of polymerization (X_n) using the programs *xgauss* where x equals *mono*-, *bi*-, *tri*-, *tetra*-, *penta*-, or *hexa*- to fit the DRI traces with a sum of 1 – 6 Gaussians according to

Equation 1, respectively. This sum-of-Gaussians analysis yielded the scaling factor A and the parameters a_i , μ_i , and σ_i , which represent the normalized pre-Gaussian factor, the average, and the standard deviation of the i^{th} Gaussian used to fit the GPC traces.

$$DRI(x) = A \times \sum_{i=1}^n a_i \frac{1}{\sigma_i \sqrt{2\pi}} \exp\left(-\frac{(x-\mu_i)^2}{2\sigma_i^2}\right) \quad (1)$$

The *xgauss*SNP program series (where $x = \text{mono}$, bi , and tri) was used to fit the DRI traces with Equation 2, which divided the GPC traces into two sums of Gaussians, where one of the sums of Gaussians was fixed in the analysis. The parameters a_i , μ_i , and σ_i determined from the *xgauss* analysis of the DRI trace of a PIBSA sample, shown below in Figure 2, were fixed in the analysis conducted with Equation 2. This procedure enabled isolation of the contribution (A in Equation 2) of the PIBSA-like molecules in the DRI traces from that of the higher order products (B in Equation 2).

$$DRI(x) = A \times \sum_{i=1}^n a_i \frac{1}{\sigma_i \sqrt{2\pi}} \exp\left(-\frac{(x-\mu_i)^2}{2\sigma_i^2}\right) + B \times \sum_{j=1}^m a_j \frac{1}{\sigma_j \sqrt{2\pi}} \exp\left(-\frac{(x-\mu_j)^2}{2\sigma_j^2}\right) \quad (2)$$

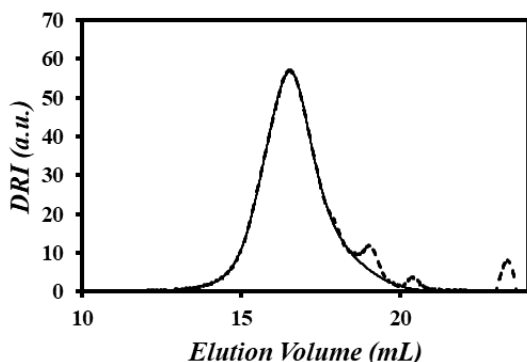


Figure 2. Plot of the (---) DRI trace and (—) gaussian fit of a dehydrated PIBSA-2 sample as a function of elution volume. The contribution of the solvent peaks at 19, 20, and 24 mL were eliminated from the calculation.

RESULTS AND DISCUSSION

The sum of Gaussians used to represent the PIBSA trace in Figure 2 was first fixed in the analysis with the *monogauss*SNP, *bigauss*SNP, and *trigauss*SNP programs used to simulate the DRI traces of the PIB(HM)SI(X) samples where X represents the N_{Am}/N_{SA} ratio used for the reactions. These programs used a sum of one, two, and three additional Gaussians, respectively, on top of the sum of four Gaussians used to represent the PIBSA contribution to the DRI traces. An example of the traces obtained by fitting the PIB(HM)SI(1.0) DRI trace with *trigauss*SNP is shown in Figure 3A, along with the overlaid fits for samples having N_{Am}/N_{SA} ratios of 0.25 – 1.0 and 1.0 – 2.0 in Figure 3B and C, respectively. In these analyses, PIBSA and *m*-PIBSI are assumed to have a same MWD and both molecules are referred to as PIBSA-like molecules (PLMs).

The overlaid Gaussian fits of the PIB(HM)SI samples showed that the MWD remained relatively constant for N_{Am}/N_{SA} ratios greater than 1. The similar DRI traces shown in Figure 3C, resulting from the fits for samples with N_{Am}/N_{SA} ratios above 1, indicated that the coupling reaction would not necessarily favor the formation of *m*-PIBSI over that of *b*-PIBSI or higher-ordered PIBSIs at higher N_{Am}/N_{SA} ratios. Each of the non-PLM traces obtained through the fits showed near-identical MWDs inferring the same PIBSI products were being produced independent of the N_{Am}/N_{SA} ratio used. This led us to infer that the non-PLM traces represented a *b*-PIBSI product which may be too sterically hindered at its core to produce trimers or higher-order PIBSIs. A linear regression was used to fit each experimental DRI trace with a sum of two traces representative of the PLMs and non-PLMs, using the traces of PIBSA and *b*-PIBSI, respectively. These fits yielded

the weight fractions of the PLMs and non-PLMs, that were in good agreement with those obtained through the Gaussian fits.

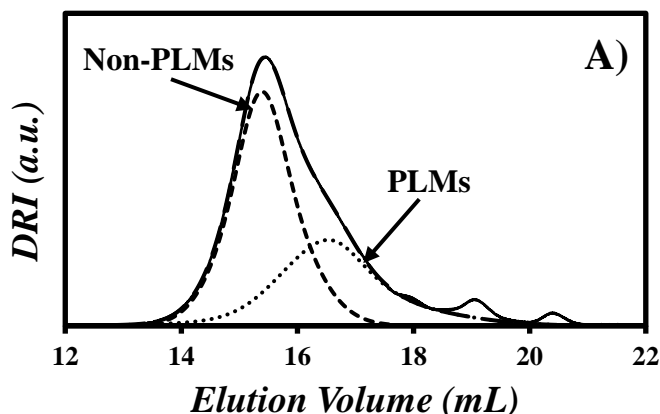
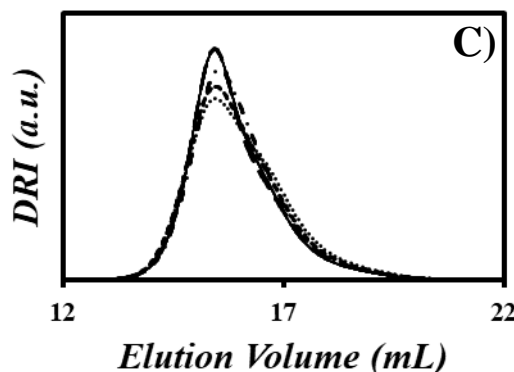
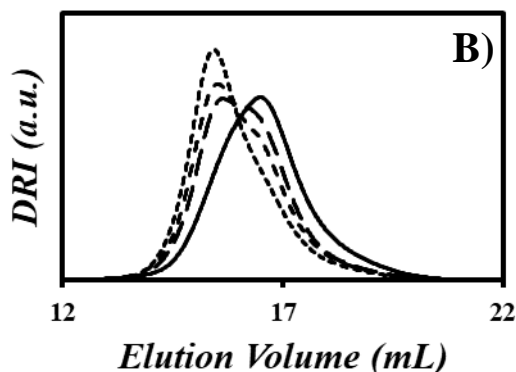


Figure 3. A) An example of the quality of the (- - -) fit with a sum of Gaussians of (———) the DRI trace of PIB(HM)SI(1.0), (······) the contribution from PIBSA-like molecules, and (- - - -) the contribution from non-PIBSA like molecules. Fits with sums of Gaussians for the PIB(HM)SI(X) samples with N_{Am}/N_{SA} ratios of B) (———) 0.25, (- - - -) 0.5, (- - - -) 0.75, and (······) 1.0, and C) (———) 1.0, (- · - ·) 1.25, (- - - -) 1.5, (- - - -) 1.75, and (······) 2.0, normalized to a sum of 1.



The PIBSA coupling results from both simulation programs were then used in conjunction with the experimental DRI traces of the PLM and non-PLM to simulate the DRI traces expected from the PIBSA coupling reaction either when assuming no limitations in higher-order PIBSI formation through PIBSA₂ with *reaction3*, or assuming that higher-order PIBSIs than *b*-PIBSI were not formed possibly due to steric hindrance with *reaction4*. These simulated DRI traces used the contributions of the different species expected in the reaction mixture listed in Table 1.

Table 1. PIBSI products simulated by the reaction3 and reaction4 programs.

N_{Am}/N_{SA} ratio	reaction3					reaction4		
	PIBSA	<i>m</i> -PIBSI	<i>b</i> -PIBSI	<i>tri</i> -PIBSI	<i>tet</i> -PIBSI	PIBSA	<i>m</i> -PIBSI	<i>b</i> -PIBSI
0.25	739	0	123	5	0	742	0	129
0.50	481	0	240	13	0	492	0	254
0.75	234	0	337	28	2	254	0	373
1.00	0	1	410	49	8	34	0	483
1.25	0	128	380	32	4	0	130	435
1.50	0	231	339	29	1	0	234	383
1.75	0	290	313	28	0	0	294	353
2.00	0	345	295	19	2	0	350	325

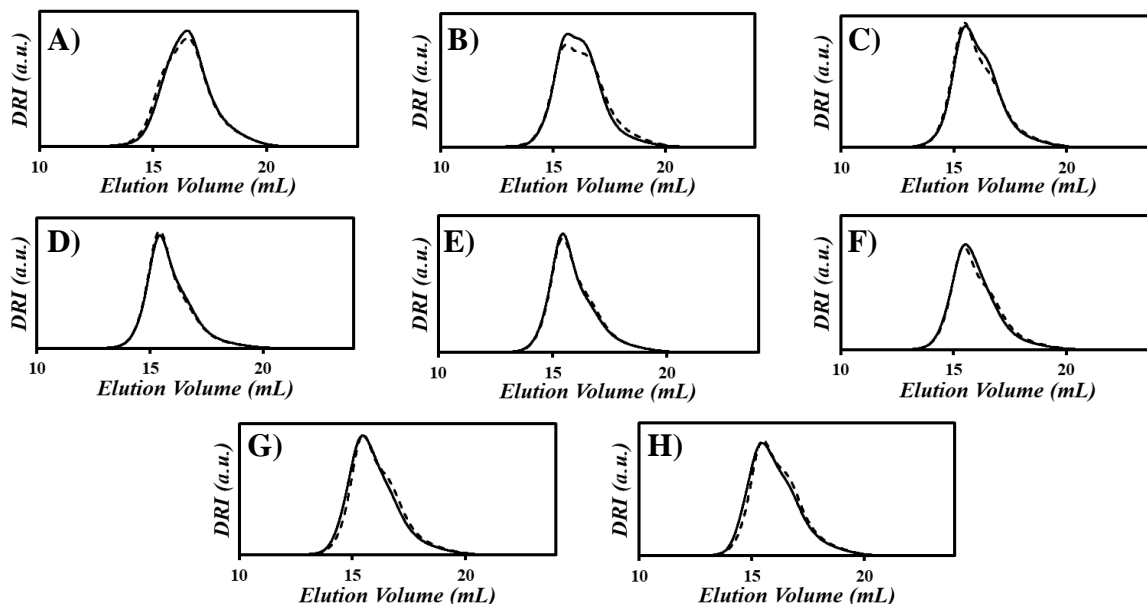


Figure 3.1. Comparison of (—) the simulated DRI traces obtained from the molar fractions obtained with *reaction4*, and the DRI traces of PIBSA and *b*-PIBSI and (- - -) the experimental DRI traces fitted with the *xgaussSNP* programs of the PIBSA-2-H(X) products. The N_{Am}/N_{SA} ratios equal A) 0.25, B) 0.5, C) 0.75, D) 1.0, E) 1.25, F) 1.5, G) 1.75, and H) 2.0.

Comparison of the experimental and simulated DRI traces for the PIB(HM)SI products obtained with the *reaction4* program provided an excellent measure of the expected MWD of the products of a PIBSA-HMDA coupling reaction while taking into account f_{doubly} and N_{Am}/N_{SA} of the PIBSA sample.

CONCLUSIONS

A series of simulation programs were developed to fit the DRI traces obtained from GPC analysis of the PIB(HM)SI samples with a sum of Gaussians. By fixing the MWD of the PLMs, the MWDs of the non-PLMs were obtained for each PIB(HM)SI sample and found to remain relatively constant, leading to the conclusion that the production of *b*-PIBSI proceeded without the formation of higher-order oligomers formed through PIBSA₂. Two programs were written to simulate the coupling reaction between PIBSA with HMDA and predict the molar ratios of different PIBSA and PIB(HM)SI products. The program which prevented oligomerization of PIBSA into trimers or higher-order PIBSAs, *reaction4*, was found to give excellent agreement with the experimental DRI traces when using the non-PLM trace to represent *b*-PIBSI, further suggesting that only *b*-PIBSI rather than higher-order PIBSA was produced in these PIBSA-HMDA coupling reactions.

REFERENCES

1. Pawlak, Z. *Elsevier*: Warsaw, Poland, 2003; Vol. 45.
2. Rizvi, S. Q. A.; edited by Rudnick, L. R. *CRC Press*, Boca Raton: Florida, **2017**, pp 45-65.
3. Seddon, E. J.; Friend, C. L.; Roski, J. P. In *Chemistry and Technology of Lubricants*. Eds. Mortier, R. M.; Malcolm, F. F.; Orszulik, S. T. *Springer: Netherlands*, **2010**, pp 213-236.
4. Rizvi, S. Q. A.; edited by Shah, R. J. *ASTM International*, West Conshohocken: PA, **2003**, pp 199-248.
5. Walch, E.; Gaymans, R. J. *Polymer* **1994**, *35*, 1774-1778.
6. Mathew, A. K.; Duhamel, J. *Macromolecules* **2001**, *34*, 1454-1469.
7. Pirouz, S.; Wang, Y.; Chong, M.; Duhamel, J. *J. Phys. Chem. B* **2014**, *118*, 3899-3911.

Janine Toma
Chemistry
Waterloo

Using Pyrene Excimer Formation to Predict the
Flexibility of Polymeric Bottle Brushes in
Solution

Using Pyrene Excimer Formation to Predict the Flexibility of Polymeric Bottle Brushes in Solution

Janine Lydia Thoma and Jean Duhamel*

Institute for Polymer Research, Waterloo Institute for Nanotechnology, Department of Chemistry, University of Waterloo, ON N2L 3G1, Canada

INTRODUCTION

Polymeric bottle brushes (PBBs) are a class of highly branched and grafted polymers, which offer structural variability and functionality. The variety in main chain and side chain chemical composition presents PBBs with an assortment of unique applications. One of the important properties of PBBs being affected by a change in side chain size, grafting density, and chemical composition is the main chain stiffness. The stiffness of a polymer can be characterized by its Kuhn length (l_K) or persistence length, l_p ($l_K=2l_p$). In turn, l_p is related to the orientation of the tangent along the contour of the main polymer chain, which is expected to persist locally in one direction over a shorter distance for a flexible polymer than for a stiffer polymer, as depicted in Figure 1.

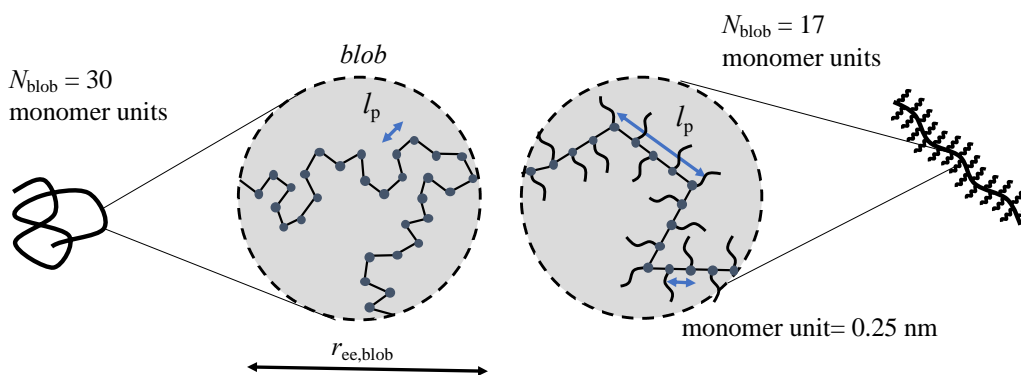







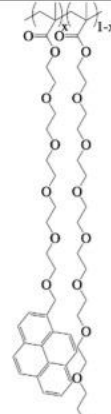

Figure 1. Random coil (left) and extended (right) polymer conformations in solution.

Covalently labeling a series of poly(oligo(ethylene glycol) methyl ether methacrylate)s with 1-pyrenemethoxy penta(ethylene glycol) enabled the study of the effect of side chain length, taken as the number (N_s) of atoms constituting the side chain backbone, on l_p by applying the fluorescence blob model (FBM). The FBM was used in conjunction with the Kratky-Porod worm-like chain (KPWLC) model to implement for the first time a *blob*-based approach to determine l_p .

RESULTS AND DISCUSSION

The chemical structure of the pyrene labeled poly(oligo(ethylene glycol) methyl ether methacrylate)s (PyEG₅-PEG_nMA with $n = 0, 3, 4, 5, 7, 9,$ and 19) used in this study along with the number of atoms in their side chain, $N_s (= 3n + 3)$ are shown in Table 1. The polymers were synthesized using a grafting through technique and conventional radical polymerization.

Table 1. Chemical structure and N_s of the PyEG₅-PEG_{*n*}MA PBBs used in this study.

Sample	PyEG ₅ -PEG ₀ MA	PyEG ₅ -PEG ₃ MA	PyEG ₅ -PEG ₄ MA	PyEG ₅ -PEG ₅ MA	PyEG ₅ -PEG ₇ MA	PyEG ₅ -PEG ₉ MA	PyEG ₅ -PEG ₁₉ MA
Structure							
N_s	3	12	15	18	24	30	60

The time resolved fluorescence decays of dilute solutions of the PyEG₅-PEG_{*n*}MA samples were acquired in aerated DMSO and then analyzed using the FBM. The FBM separates the polymer backbone into even sized sub-volumes or *blobs*. The FBM can then determine the number of structural units encompassed within a *blob*, N_{blob} , where N_{blob} is expected to be larger or smaller for a more flexible or a locally stiffer polymer, respectively (see Figure 1). This was indeed the case, as shown in Figure 2, where the average N_{blob} value, $\langle N_{blob} \rangle$, obtained for all PyEG₅-PEG_{*n*}MA samples of a same *n* value, was compared for each of the PyEG₅-PEG_{*n*}MA polymers. Poly(methyl methacrylate) (PyEG₅-PEG₀MA) is known to adopt a random coil conformation in solution and it yielded the largest $\langle N_{blob} \rangle$ value. For larger *n* values, $\langle N_{blob} \rangle$ decreased with increasing N_s before reaching a plateau for the largest side chain constituted of 60 atoms (PyEG₅-PEG₁₉MA). The FBM was then combined with the Kratky-Porod worm-like chain (KPWLC) model to extract the persistence length, l_p , of the PyEG₅-PEG_{*n*}MA polymers. Kratky and Porod derived Equation 1 using the end-to-end distance of a polymer coil, $\langle r_{ee} \rangle_{KP}$, and the contour length of the polymer, L . L was set equal to $N \times l$ where N and l are the number of bonds in the backbone and the length of a C-C bond (0.125 nm), respectively.

$$\langle r_{EE}^2 \rangle_{KP} = 2l_p L - 2l_p^2 \left[1 - \exp(-L/l_p) \right] \quad (1)$$

Using a *blob*-based approach to determine the l_p of the PyEG₅-PEG_{*n*}MA polymers first required the determination of the end-to-end distance of a *blob*, $\langle r_{ee} \rangle_{blob}$. $\langle r_{ee} \rangle_{blob}$ was calculated by determining $\langle N_{blob} \rangle$ for an infinitely long side chain, $N_{blob}(\infty)$. This represented the point when the polymer has reached a locally extended conformation ($\langle r_{ee} \rangle_{blob} = N_{blob}(\infty) \times 2l$). Since the same pyrene derivative was used for all PyEG₅-PEG_{*n*}MA samples, the volume probed by an excited pyrene label was the same, and consequently $\langle r_{ee} \rangle_{blob}$ took a same value, for each PyEG₅-PEG_{*n*}MA polymer.

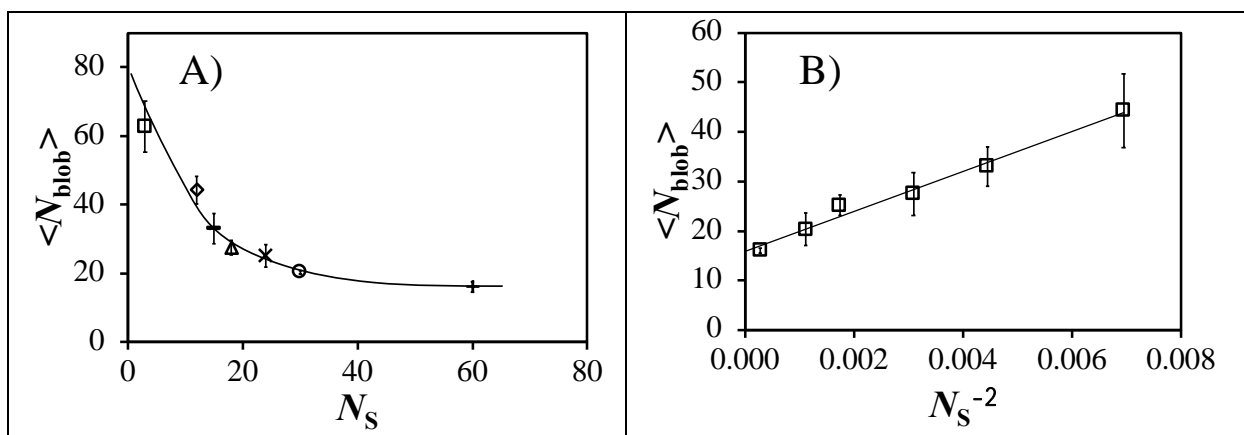


Figure 2. Plot of A) $\langle N_{\text{blob}} \rangle$ versus N_S for (□) PyEG₅-PEG₀MA, (◇) PyEG₅-PEG₃MA, (○) PyEG₅-PEG₄MA, (△) PyEG₅-PEG₅MA, (×) PyEG₅-PEG₇MA, (◊) PyEG₅-PEG₉MA, and (◐) PyEG₅-PEG₁₉MA and B) $\langle N_{\text{blob}} \rangle$ versus N_S^{-2} for PyEG₅-PEG_nMA.

$\langle N_{\text{blob}} \rangle$ for an infinite N_S value, $N_{\text{blob}}(\infty)$, was extracted from Figure 2B, where $\langle N_{\text{blob}} \rangle$ was plotted as a function of N_S^{-2} . Extrapolating the straight line in Figure 2B to the y-intercept yielded an $N_{\text{blob}}(\infty)$ value of 15.9 ± 0.9 . Assigning 0.125 nm as the length of a C–C bond in the all-trans conformation, $\langle r_{\text{ee}} \rangle_{\text{blob}}$ was then calculated and found to equal $(15.9 \times 0.25 \text{ nm})^2 = 15.8 \text{ nm}^2$. Once the size of the blob was determined, l_p could be calculated for each PyEG₅-PEG_nMA polymer by setting the contour length of the chain in Equation 1 to that of a *blob* (L_{blob}) such that L_{blob} equaled $N_{\text{blob}} \times l$. As often done in the literature, the effect of N_S on l_p could be discussed in terms of a main chain stiffness parameter, λ^{-1} , which was introduced by Nakamura.¹ λ^{-1} is equivalent to the Kuhn length which is twice the l_p .

$$\lambda^{-1} = \lambda_0^{-1} + \lambda_b^{-1} \quad (2)$$

In Equation 2, λ_0^{-1} and λ_b^{-1} represent the intrinsic stiffness of the backbone devoid of side chains and the excess free energy against bending generated by collisions between the dense side chains. Plotting l_p against N_S in Figure 3A showed that l_p increased with increasing N_S with the y-intercept corresponding to λ_0^{-1} .

In the literature, λ_b^{-1} is found to scale as N_S^2 for flexible side chains.^{1–4} The trend in Figure 3A could be linearized in Figure 3B by plotting l_p against N_S^2 . To validate the l_p results obtained by pyrene excimer fluorescence (PEF) through a *blob*-based approach, intrinsic viscosity, $[\eta]$, conformation plots were constructed using gel permeation chromatography (GPC). The GPC system was run with a DMSO mobile phase and was equipped with a viscometer detector as well as a multi-angle light scattering detector (MALLS). The l_p was extracted from the $[\eta]$ conformation plots using the Bohdanecky linearization⁵ before being plot along the results obtained by PEF in Figure 3. The l_p values retrieved from PEF or GPC analysis were found to agree with each other, thus validating the PEF results.

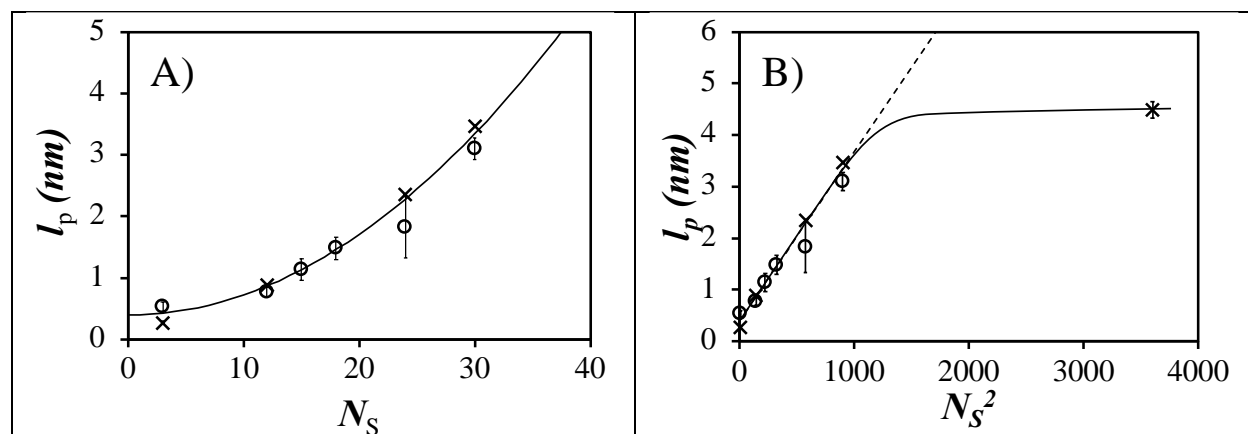


Figure 3. Plot of A) l_p versus N_s for the PyEG₅-PEG_nMA samples and B) l_p versus N_s^2 where l_p was determined by (●) fluorescence and (×) GPC.

l_p for PyEG₅-PEG₁₉MA could not be determined using the FBM since it was approaching the locally extended conformation, where l_p was reaching an infinitely long length on the length scale probed by an excited pyrene. However, GPC analysis could extract l_p and it was found to deviate from the linear relationship observed for l_p -vs- N_s^2 in Figure 3B, as would be expected for a flexible side chain. This result was attributed to a saturation effect also seen by Rathgeber.⁶ Once the side chains are long enough to fully occupy the local volume around the main chain, any extra increase in side chain length would cause l_p to scale differently than expected for a flexible side chain.

CONCLUSIONS

In conclusion, the flexibility of seven PyEG₅-PEG_nMA samples with $n = 0, 3, 4, 5, 7, 9,$ and 19 was studied in dimethyl sulfoxide (DMSO). The fluorescence blob model (FBM) along with the Krakty-Porod worm-like chain (KPWLC) model were combined to determine the persistence length, l_p , of the PyEG₅-PEG_nMA samples by PEF. l_p was found to increase with increasing side chain length, N_s . Good agreement was obtained between the l_p values determined by PEF and GPC with the exception of PyEG₅-PEG₁₉MA, whose side chain contained 60 atoms. The different behavior observed for PyEG₅-PEG₁₉MA is believed to arise from the saturation of the local volume surrounding the polymer backbone. Further research is being conducted to investigate the effect of solvent quality on l_p .

REFERENCES

1. Nakamura, Y.; Norisuye, T. Backbone Stiffness of Comb-Branched Polymers. *Polym. J.* **2001**, *33*, 874-878.
2. Fredrickson, G. H. Surfactant-Induced Lyotropic Behavior of Flexible Polymer Solutions. *Macromolecules* **1993**, *26*, 2825-2831
3. Subbotin, A.; Saariaho, M.; Ikkala, O.; Brinke, G. Elasticity of Comb Copolymer Cylindrical Brushes. *Macromolecules* **2000**, *33*, 3447-3452.
4. Chatterjee, D.; Vilgis, T. A. Scaling Laws of Bottle-Brush Polymers in Dilute Solutions. *Macromol. Theory Simul.* **2016**, *25*, 518-523.
5. Bohdanecky, M. New Method for Estimating the Parameters of the Wormlike Chain Model from the Intrinsic Viscosity of Stiff-Chain Polymers. *Macromolecules* **1983**, *16*, 1483-1492.
6. Rathgeber, S.; Pakula, T.; Wilk, A.; Matyjaszewski, K.; Lee, H-L.; Beers, K. Bottle-Brush Macromolecules in Solution: Comparison between Results Obtained from Scattering Experiments and Computer Simulations. *Polymer* **2006**, *47*, 7318-7327.